

**3D GEOMETRY AND VELOCITY STRUCTURE OF THE TACOMA
BASIN, WESTERN WASHINGTON**

By

BRETT JOSEPH HIETT, B.S.

THESIS

Presented to the Faculty of the Graduate School of

The University of Texas at El Paso

In Partial Fulfillment

of the Requirements

for the Degree of

MASTER OF SCIENCE

Department of Geological Sciences

UNIVERSITY OF TEXAS AT EL PASO

December, 2000

3D GEOMETRY AND VELOCITY STRUCTURE OF THE TACOMA

BASIN, WESTERN WASHINGTON

BRETT JOSEPH HIETT

Department of Geological Sciences

APPROVED:

Dr. Kate C. Miller, Chair

Dr. G. Randy Keller

Dr. Alan Dean

Associate Vice President for
Graduate Studies

Acknowledgements

I would like to thank those who helped me along the way. I want to thank Dr. Kate C. Miller for acquiring the SHIPS data for me and being the main reason why I got through this project. Thanks to Dr. G. Randy for help in processing the gravity points taken in September of 1999. I would like to thank Tom Brocher from the USGS for handing this data over to me for analysis. Thanks to Tom Pratt from the USGS for getting the seismic reflection profiles that aided in the interpretation. Thanks to Tom Parsons from the USGS and John Hole at Virginia Tech University for help in troubleshooting the Hole Code. A very special thanks goes out to Catherine Snelson for all her help from the beginning to the very end. Thanks are due to Carlos Montana and Raed Aldouri for their enormous help with the computer facility and the long distance correspondence. I would like to thank Dr. Steve Harder for his help in processing the GPS data. Thanks go out to Dr. Chris Andronicos for his ideas in the interpretation. Thanks to Marcos Alvarez and Bruce Beaudoin at PASSCAL for their help in processing/writing data to tape to be brought back to UTEP. I would like to thank Oscar, Tefera, Fiona, Terry, for the tidbits of information that I gleaned from them during this whole process. Finally I would like to thank my wife, Karen, for her undying support and help. I couldn't have done it without her.

This thesis was submitted to committee on October 6th, 2000.

Abstract

Within the highly populated Puget Lowland of western Washington, local faulting and the subduction of the Juan de Fuca plate pose a seismic threat that is compounded by the potential for amplification of ground shaking within basins that underlie the region. Studies of other basins on the west coast of the United States (e.g., in San Francisco and Los Angeles) show that they have the propensity to amplify seismic energy up to 15 times. Although the Pacific Northwest has been relatively aseismic compared to other subduction zones, studies have found that this region has M7.0+ earthquake potential on more than one seismogenic structure. The objective of the Seismic Hazards Investigation in Puget Sound (SHIPS) in March 1998 was to produce a 3-D velocity and structural model of the Puget Lowland to help identify and resolve structures not previously studied. Over 300 data acquisition systems were deployed in the Puget Lowland and recorded airgun shots every 16 seconds for an 18-day period. This study presents the results of tomographic inversion of SHIPS data in and around the Tacoma basin. Inversion of over 140,000 arrivals from 61 recorders produces a velocity model that shows that the Tacoma basin is made up of 3 subbasins that trend northwest-southeast. Assuming velocities of 5.5 km/s as a proxy for the top of the Crescent Formation, depths of the subbasins vary from 4.5 to 6 km. Previous studies had estimated the depth of the Tacoma basin to be 3 to 4.5 km depth. The Tacoma basin may have formed as the result

of relief created by thrusting up the Seattle uplift. The subbasins may have originated as pull-apart basins in an Eocene from north-south strike-slip regime.

Table of Contents

Acknowledgements.....	iii
Abstract.....	iv
Table of Contents.....	vi
List of Figures	vii
Introduction	1
Geologic Background.....	5
Previous Geophysical Studies	15
Site Response.....	22
Seismic Data Acquisition and Analysis	27
Seismic Data.....	29
Tomography.....	36
Resolution.....	53
Tomography Results.....	66
Wide-Angle Reflection Methodology.....	78
Discussion	90
Conclusion	105
References	106
Appendix: Gravity.....	114
Curriculum Vitae	115

List of Figures

Figure 1: Regional tectonic map showing study area.....	2
Figure 2: Basemap showing SHIPS experiment shots and receivers	4
Figure 3: Geologic map of western Washington	6
Figure 4: Stratigraphy of the Seattle basin based on borehole information.....	14
Figure 5: Map view of seismicity in the Puget Lowland.....	16
Figure 6: 3 cross sections of seismicity in Puget Lowland	17
Figure 7: Theoretical and empirical site response curves	23
Figure 8: Seismic gather from station C3008.....	30
Figure 9: Seismic gather from station C3011	31
Figure 10: Seismic gather from station C3014.....	32
Figure 11: Seismic gather from station D4010.....	34
Figure 12: Seismic gather from station D4011	35
Figure 13: Input velocity model from tomography	39
Figure 14: RMS vs. iteration plot from tomography.....	40
Figure 15: Travel time residuals from stations C3007 to C3011	42
Figure 16: Travel time residuals from stations C3012 to D4010	43
Figure 17: Travel time residuals from stations D4011 to E5002	44
Figure 18: Travel time residuals from stations E5003 to E5007.....	45
Figure 19: Travel time residuals from stations E5008 to G7003	46
Figure 20: Travel time residuals from stations G7004 to G7008.....	47
Figure 21: Travel time residuals from stations G7009 to H8002	48

Figure 22: Travel time residuals from stations H8003 to H8007	49
Figure 23: Travel time residuals from stations H8008 to UW40	50
Figure 24: Travel time residuals from stations UW42 to UW47	51
Figure 25: Travel time residuals from stations UW48 to UW52	52
Figure 26: Travel time residuals from stations UW53 to UW58	53
Figure 27: Checkerboard results with 10x10 km checkers, input and 3 km	56
Figure 28: Checkerboard results with 10x10 km checkers, 5 km and 7 km	57
Figure 29: Checkerboard results with 15x15 km checkers, input and 3 km	58
Figure 30: Checkerboard results with 15x15 km checkers, 5 km and 7 km	59
Figure 31: Checkerboard results with 15x3 km checkers, input, 38 km to 53 km	60
Figure 32: Checkerboard results with 15x3 km checkers, 58 km to 78 km	61
Figure 33: Ray coverage at 3 km depth	63
Figure 34: Ray coverage at 5 km depth	64
Figure 35: Ray coverage at 7 km depth	65
Figure 36: Velocity slices from tomography in map view at 1 km	67
Figure 37: Velocity slices from tomography in map view at 3 km	68
Figure 38: Velocity slices from tomography in map view at 5 km	69
Figure 39: Velocity slices from tomography in map view at 7 km	70
Figure 40: East-west velocity slices from tomography, 33 km to 53 km	73
Figure 41: East-west velocity slices from tomography, 58 km to 78 km	74
Figure 42: North-south velocity slices from tomography, 30 km to 50 km	75

Figure 43: North-south velocity slices from tomography, 55 km to 75 km.....	76
Figure 44: North-south velocity slices from tomography, 80 km to 95 km.....	77
Figure 45: Color map of the depth to the 5.5 km/s velocity contour from the tomography	79
Figure 46: Seismic section from station C3008 reduced at 6 km/s with reflection calculations overlain.....	81
Figure 47: Seismic section from station C3011 reduced at 6 km/s with reflection calculations overlain.....	82
Figure 48: Seismic section from station C3014 reduced at 6 km/s with reflection calculations overlain.....	83
Figure 49: Seismic section from station D4010 reduced at 6 km/s with reflection calculations overlain.....	84
Figure 50: Seismic section from station D4011 reduced at 6 km/s with reflection calculations overlain.....	85
Figure 51: Near offset gather from station C3011 with a deconvolution applied and reflection calculations overlain	86
Figure 52: Near offset gather from station C3014 with a deconvolution applied and reflection calculations overlain	87
Figure 53: Near offset gather from station D4010 with a deconvolution applied and reflection calculations overlain	88
Figure 54: Basemap showing location of reflection profiles	92

Figure 55: Reflection line 1 displayed in time with velocity contours and velocity colormap overlain (reflection from Pratt et al., 1997)	93
Figure 56: Reflection line 2 displayed in time with velocity contours and velocity colormap overlain (reflection from Pratt et al., 1997)	94
Figure 57: Reflection line 3 displayed in time with velocity contours and velocity colormap overlain (reflection from Pratt et al., 1997)	95
Figure 58: Reflection line 1 displayed in depth with velocity contours and velocity colormap overlain.....	96
Figure 59: Reflection line 2 displayed in depth with velocity contours and velocity colormap overlain.....	97
Figure 60: Reflection line 3 displayed in depth with velocity contours and velocity colormap overlain.....	98
Figure 61: Cross section cartoons of structural style in Puget Lowland and Wyoming.....	101
Figure 62: Schematic of basement in Laramide thrusting, Colorado.....	103

Introduction

The highly populated Puget Lowland of western Washington is subject to a variety of seismic hazards including inter-plate earthquakes due to the subduction of the Juan de Fuca plate (Figure 1) and earthquakes that originate within the subducting slab as well as within the crust (Ludwin et al., 1991). Deep, large inter-plate earthquakes beneath Puget Sound and vicinity are the most clearly identified seismic hazard (Ludwin et al., 1991). Evidence for a great earthquake ($M \sim 9.0$) comes from paleoseismic data that suggest a rupture along a 625 km to greater than 900 km length of the coast in 1700 AD (Atwater and Hemphill-Haley, 1997; Nelson et al., 1995). Moreover, crustal faults such as the Seattle fault and the Southern Whidbey Island fault may be the source of M 6-7 earthquakes (Johnson et al., 1999; Pratt et al., 1997; Johnson et al., 1996).

The potential for local amplification of ground motion due to an earthquake is of concern in the Puget Lowland because it is underlain by a number of Tertiary basins including the Chehalis, Tacoma, Seattle, and Everett basins (Figure 2). In recent years, site response studies have produced considerable evidence for amplification in a number of basins and sediment laden areas including the Marina District (Zhang and Papageorgiou, 1996; Boatwright et al., 1991), the Los Angeles basin (Wald and Graves, 1998; Hartzell et al., 1998; Meremonte et al., 1996), the San Fernando Valley basin (Hartzell et al., 1998; Hough and Field, 1996, Meremonte et al., 1996), and the San Diego basin (van de Vrugt et al., 1996). Numerical simulations show that amplification is sensitive

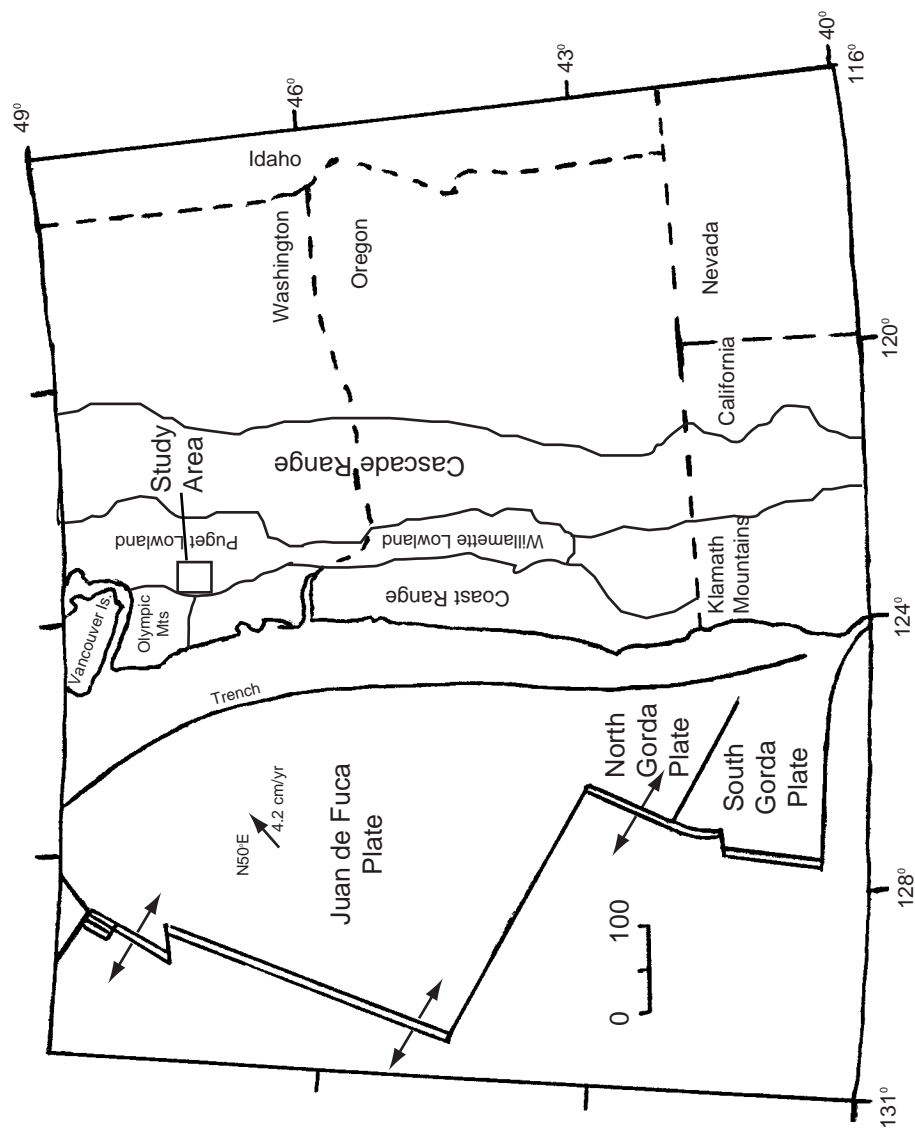


Figure 1: Location map for subduction regime. States and mountains are noted for reference. Direction of Juan de Fuca Plate motion is also noted. After Mooney and Weaver, 1989.

to basin shape and to sediment-basement velocity contrast if the contrast is high (Moczo et al., 1996). In addition, azimuth and distance also play an important role in amplification of seismic energy (e.g., Catchings and Kohler, 1996). A capacity to reliably model these effects will allow for better forecasts of earthquake shaking due to focusing of seismic energy in the Tacoma Basin area.

The purpose of the 1998 Seismic Hazards Investigation in Puget Sound (SHIPS) experiment was to obtain new, three-dimensional structural control on the seismogenic structures and Cenozoic basins in western Washington and southwestern British Columbia (Brocher et al., 1998; Fisher et al., 1999). During the experiment, a ship tracking through Puget Sound, Hood Canal, Lake Washington, the Strait of Juan de Fuca, and the Strait of Georgia fired an airgun array over 33,000 times over an 18 day span (Figure 2). These shots were recorded by 257 RefTEKs, 15 OBSs, and 71 permanent earthquake network stations in and around the Puget Lowland (Fisher et al., 1999).

In this study a subset of the SHIPS refraction data and a tomographic inversion is used to calculate detailed velocity models of the Tacoma basin and surrounding area. These velocity models coupled with existing gravity and seismic reflection data help define a new three-dimensional geophysical model of the Tacoma Basin.

Geologic Background

Since early Cretaceous time, the tectonics of western Washington have been dominated by convergence of the Farallon plate with the North American plate (Atwater, 1970; Armstrong 1978; Duncan, 1982; Wells et al., 1984). Approximately 25 Ma, the Juan de Fuca microplate broke away from the Farallon plate. It continues to subduct beneath the North American plate today (Wells et al., 1984) at a rate of about 4.2 cm/yr at N50°E (Riddihough, 1977,1984) (Figure 1). Underlying the Cascade forearc is an accretionary complex formed during plate convergence consisting of the Eocene basaltic Siletz terrane that is now being underthrust by Cenozoic marine sedimentary rocks (Parsons et al., 1999). Outcrops in the Olympic Mountains shows that this assemblage consists of thrust-imbricated marine turbidites and minor pillow basalts (Tabor and Cady, 1978).

Within the forearc of the Cascadia subduction zone lies the Puget Lowland, which consists of a number of subbasins including the Tacoma basin (Figure 3). The basins straddle an inferred major north-trending crustal boundary between the Eocene Siletz terrane to the west and pre-Tertiary basement rocks of the Cascades to the east, termed the Coast Range Boundary fault (Johnson, 1985). This area has undergone Eocene to recent extensive faulting and deformation (e.g. Johnson, 1985) which can be attributed to the oblique subduction of the Juan de Fuca plate beneath the North American plate. A major portion of the geologic framework is poorly constrained because most pre-

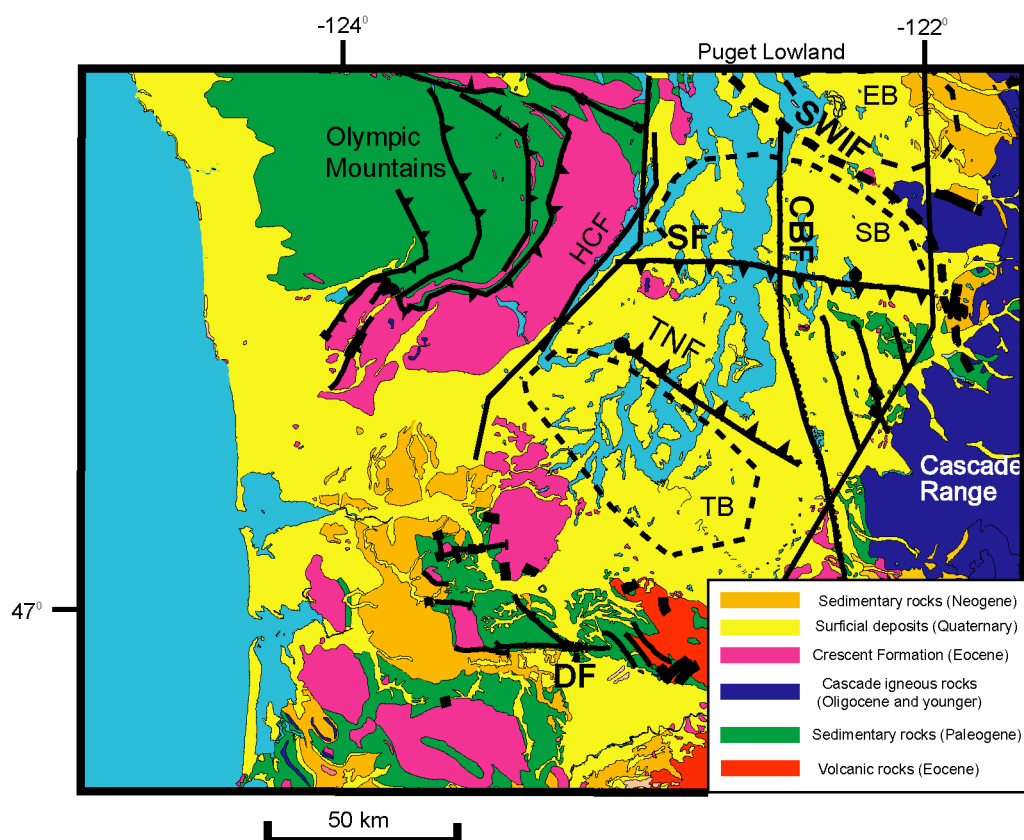


Figure 3: Geologic map of western Washington showing the Olympic Mountains, Cascade Mountains, and the Puget Lowland. Abbreviations for major faults that are shown in thick black lines: SF=Seattle Fault; TNF=Tacoma Narrows Fault; HCF=Hood Canal Fault; SWIF=Southern Whidbey Island Fault; CBF=Coast Range Boundary Fault (also referred to as the Puget Fault); DF=Doty Fault. Basins are indicated by dashed outlines: EB=Everett Basin; SB=Seattle Basin; TB=Tacoma Basin. Geology from Raines and Johnson (1996).

Pleistocene geologic features are obscured by a thick mantle of glacial sediment or vegetation (Johnson, 1996).

Cascade Range Rocks

The Cascade Range is a Tertiary to recent magmatic arc formed as a result of subduction of the Juan de Fuca plate (e.g., Guffanti and Weaver, 1988), which is built on a diverse suite metamorphic, igneous, and sedimentary rocks comprised of many different crustal terranes with exotic origins (e.g. Tabor, 1994). These rocks formed the framework of the Washington continental margin after the accretion of these crustal terranes by the Cretaceous or early Tertiary time (Tabor, 1994). During early to early-middle Eocene time, this province experienced significant strike-slip faulting and transtensional deformation (Johnson, 1985). In this eastern pre-Tertiary basement, Cascade arc volcanism began in the late Eocene to early Oligocene and has continued to the present (Johnson, 1996).

Siletz Terrane and Coast Range Rocks

In Western Washington, the Coast Range rocks are underlain by thick Paleocene to middle Eocene mostly submarine basalts of the Siletz terrane (also referred to hereafter as the Crescent Formation). Two models that may explain the origin of the Coast Range basement are: 1) accretion to the continent of hot spot generated linear seamount chains (Simpson and Cox, 1977; Duncan, 1982) and, 2) eruption during oblique rifting of the continental margin as it overrode an active hotspot (Wells et al., 1984; Babcock, 1992).

Interpretations made by Babcock et al. (1992) are consistent with extrusion in a basin or series of basins formed by this rift.

On the eastern Olympic Peninsula, a 16.2-km section of the Crescent Formation is exposed. The 8.4 km thick lower part of the sequence consists mainly of pillowed submarine to massive basalt flows, whereas the upper 7.8 km is composed of pillowed to massive subaerial flows (Babcock et al., 1992).

Structurally, the Coast Range basement and overlying rocks of southwest Washington and western Oregon have gentle dips and are cut by high-angle faults (e.g. Wells, 1990). Localized block rotations and regional rotation were probably facilitated by the presence of these high-angle faults (Wells and Heller, 1988; Wells, 1990). Conversely, the Crescent Formation in the northern coast Range province apparently did not undergo block rotations but did experienced late Miocene and younger uplift to form an east-plunging anticline that is underlain by an Eocene and younger accretionary complex of the Olympic Mountains (Tabor and Cady, 1978; Brandon and Calderwood, 1990; Brandon and Vance, 1992).

Potential Seismogenic Structures

The ability to define potentially active faults in western Washington is a major step in understanding the seismic hazard of the region. The Coast Range boundary fault was inferred by Johnson (1984) to be a major dextral transcurrent fault that truncated the pre-Tertiary continental framework of western Washington and southern Vancouver Island during the late Cretaceous and early Tertiary.

This fault now marks the boundary between the Coast Range province and the Cascade Range province. The fault trends north and is covered by Puget Lowland sediments (Figure 3). Sedimentary basins that formed marginal to the fault are characterized by rapid facies changes and sediment accumulation rates, abrupt stratigraphic thinning and thickening, irregular basin margins, petrographic mismatches, and other features consistent with origin in a zone of strike-slip faulting. The Coast Range Boundary fault was part of a network of intracontinental late Cretaceous-early Tertiary strike-slip faults in the northern North American Cordillera and likely served as a major avenue of northward translation (Johnson, 1984).

The Southern Whidbey Island fault is a northwest-trending fault comprised of a broad, steep, northeast-dipping zone that includes several splays with inferred strike-slip, reverse, and thrust displacement (Johnson, 1996). This fault also represents the inferred northern boundary between the Cascade Range province to the northeast and the Coast Range province to the southwest (Figure 3). The fault is thought to have originated during the early Eocene as a dextral strike-slip fault along the eastern side of a continental margin rift. Slip began during the late middle Eocene and continues to the present (Johnson, 1996).

The Seattle fault is thought to have originated as a restraining transfer zone with dextral offset on the Coast Range boundary fault (Johnson, 1994) (Figure 3). The main phase of movement on the Seattle fault is thought to be Miocene and younger because Eocene to Oligocene sedimentary rocks do not

thicken towards the fault whereas the Miocene sedimentary rocks do (Johnson, 1994; ten Brink et al, in review). Johnson (1994,1999) suggests that the Seattle fault is a zone that consists of three or more south-dipping reverse faults with slip rates of about 0.6 mm/yr on the main fault, that separates the Seattle basin and the Seattle uplift and 0.7-1.1 mm/yr across the entire zone. An active, north-trending, high-angle, strike-slip fault zone with a displacement of approximately 2.4-km may cut the Seattle fault into two main segments (Johnson et al., 1999). The Seattle fault is estimated to have a total area of about 4420-km² and could generate an M=7.6 to 7.7 earthquake (Pratt et al., 1997). Segmentation of the Seattle fault may reduce the maximum size earthquake by only allowing a portion of the fault to slip.

Pratt et al. (1997) hypothesized that the Puget Lowland lies on a north-directed thrust sheet based on faults and folds in the region. The base of this sheet may lie at 14 to 20 km deep with the Southern Whidbey Island fault zone forming the northern edge of the sheet, the eastern edge of the Olympic Mountains forming the western edge of the sheet, and a series of north to northwest trending faults and folds at the base of the Cascades forming the eastern edge of the thrust sheet. The decollement is interpreted to be at a depth of about 17+/- 3 km, which is consistent with earthquake focal mechanisms, potential field data, and some geomorphic and paleoseismic observations (Pratt et al., 1997).

North of Seattle lies the Kingston arch (Figure 2), which is a west trending antiform interpreted from potential field and seismic reflection data (Gower et al., 1985, Johnson et al., 1994, 1996). Strata are almost flat across its 6.0-km wide top, dip about 24° southward on the south flank, and dip about 30° northward on the north flank (Pratt et al., 1997). The east side of the structure shows a narrower top (3-km) and a wider north flank (6.5 km versus 3.5 km) with the cause of the lateral change being unknown (Pratt et al., 1997). A west-trending Bouguer gravity high is consistent with the arch lifting Crescent formation rocks closer to the surface. The arch has been interpreted to be a ramp anticline caused by a 2 km step up in the decollement or a fault propagation fold above a blind thrust fault that is not imaged on seismic data (Pratt et al., 1997). Pratt et al. (1997) interpret arch formation as occurring after the early Oligocene since Oligocene strata do not onlap onto both flanks of the arch, but rather are folded within the Kingston arch.

The Seattle uplift is a region of uplifted and folded strata between Seattle and Tacoma (Figure 3). The southern edge of the uplift is defined by a 10 km wide zone of strata dipping 15° to 25° to the southwest (Pratt et al., 1997). Three small anticlines 4 to 8 km wide and having up to 1.5 km of structural relief are superimposed on the uplift and trend nearly due west. Igneous rocks were penetrated at a depth of 213 m in a well on the Seattle uplift (Danes et al., 1965).

Pratt et al. (1997) interpreted the Black Hills as a structural uplift above one or more thrust faults (Figure 3). Crescent Formation basaltic rocks and the

slightly younger andesitic volcanic rocks of the upper middle to upper Eocene Northcraft Formation are found in the Black Hills. Northwest trending thrust or reverse faults (Snively et al., 1958) and the east trending Doty fault are two distinct fault trends that occur on the south flanks of these uplifts (Figure 3). These faults dip northward and may merge with the decollement beneath the north side of the Black Hills (Pratt et al., 1997).

Basins

The Seattle basin is located north of the Seattle fault (Figure 3) and south of the Kingston Arch. Eocene to Quaternary strata fill the basin and thin from about 7.5 km at the Seattle fault to about 2 km at the Kingston Arch, 20 km to the north (Johnson et al., 1994; Pratt et al., 1997). The most recent study shows the basin to be 10 km deep and to be partitioned into 3 subbasins (Brocher et al., in press). Basin fill consists of lower to upper Eocene marine strata, upper Eocene to Oligocene Blakeley Formation, Miocene to Pliocene Blakely Harbor Formation, and Quaternary deposits (Johnson et al., 1994) (Figure 4). Johnson et al. (1994) suggests that the basin became a discrete geologic element in the late Eocene as a result of reorganization in regional fault geometry and kinematics. The Coast Range Boundary fault stepped eastward, and the Seattle fault began as a restraining transfer zone. Offset on the Seattle fault forced flexural subsidence in the Seattle basin to the north that continues to the present.

Due to lack of borehole data, little is known about the lithology and age of sediments in the Tacoma basin (Figure 3). Pratt et al. (1997) interpret seismic

reflection and gravity data to show that the basin is 3.5 km thick. Danes et al. (1965) estimated 4 km of sedimentary rocks in the Tacoma basin with a gently north-dipping southern edge.

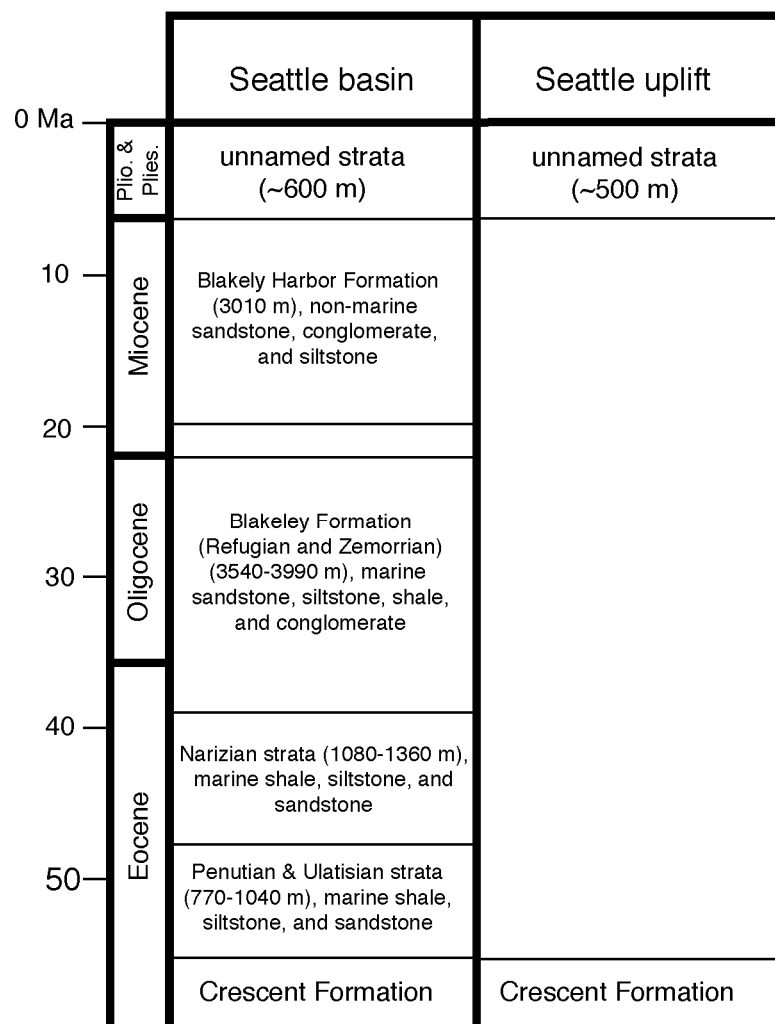


Figure 4: Stratigraphy of the Seattle basin and Seattle uplift with control provided by the Mobil Kingston #1 borehole (Johnson et al., 1994).

Previous Geophysical Studies

The Puget Lowland has been studied rather extensively using geophysical methods. Refraction, reflection, earthquake tomography, and gravity have been important contributors to understanding the geology of this area. Many faults, basins, and uplifts have been well defined while others remain to be looked at in detail. This is due in part to the fact that earthquake tomography results in the Puget Lowland have not imaged shallow structures well.

Seismicity

Studies suggest that the Cascadia subduction zone is capable of producing a great earthquake based on its similarity to other subduction zones (e.g., Clague, 1997; Heaton and Kanamori, 1984) and on the stresses that have been determined in the upper crust near the Cascade Range volcanic arc (Hyndman and Wang, 1995; Weaver and Smith, 1983). Additional evidence for great earthquakes ($M \sim 9.0$) comes from paleoseismic data (Nelson et al., 1995, Atwater and Hemphill-Haley, 1997) and are consistent with recent GPS and strain measurements that also suggest the potential for great earthquakes (Hyndman and Wang, 1995). These earthquakes may occur as frequently as once every 300 years with an average recurrence time of 500 to 600 years (Pratt et al., in press).

Analysis of the distribution of present-day seismicity (Figures 5 and 6) show that deep events occur primarily within the upper part of the subducting oceanic

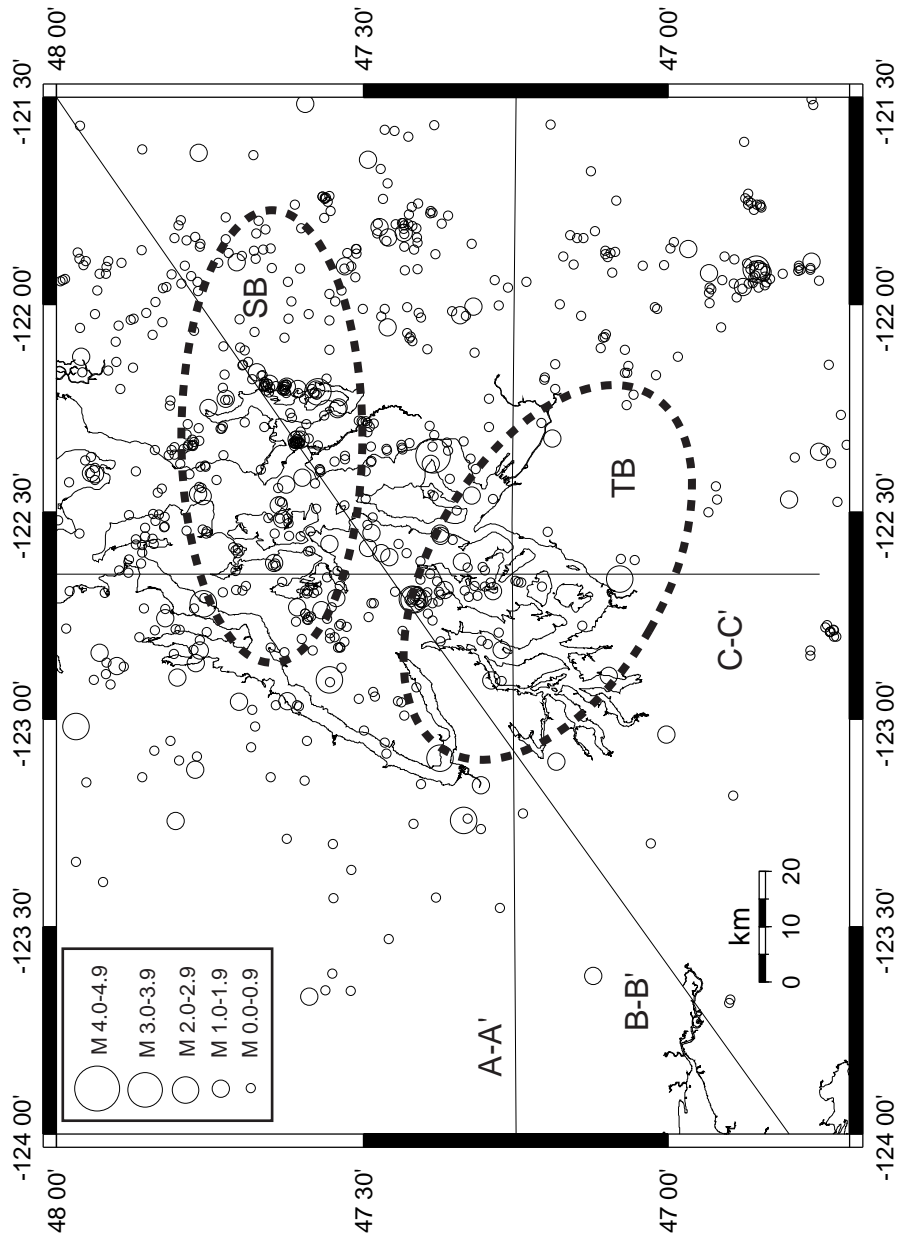


Figure 5: Map of epicenters in the Puget Lowland. Earthquakes occurred from 1969 to 1999 and are good quality locations from the University of Washington database. Cross sections of lines 1, 2, and 3 are shown in Figure 6. Basins are outline with dashed ellipses: TB=Tacoma Basin; SB=Seattle Basin.

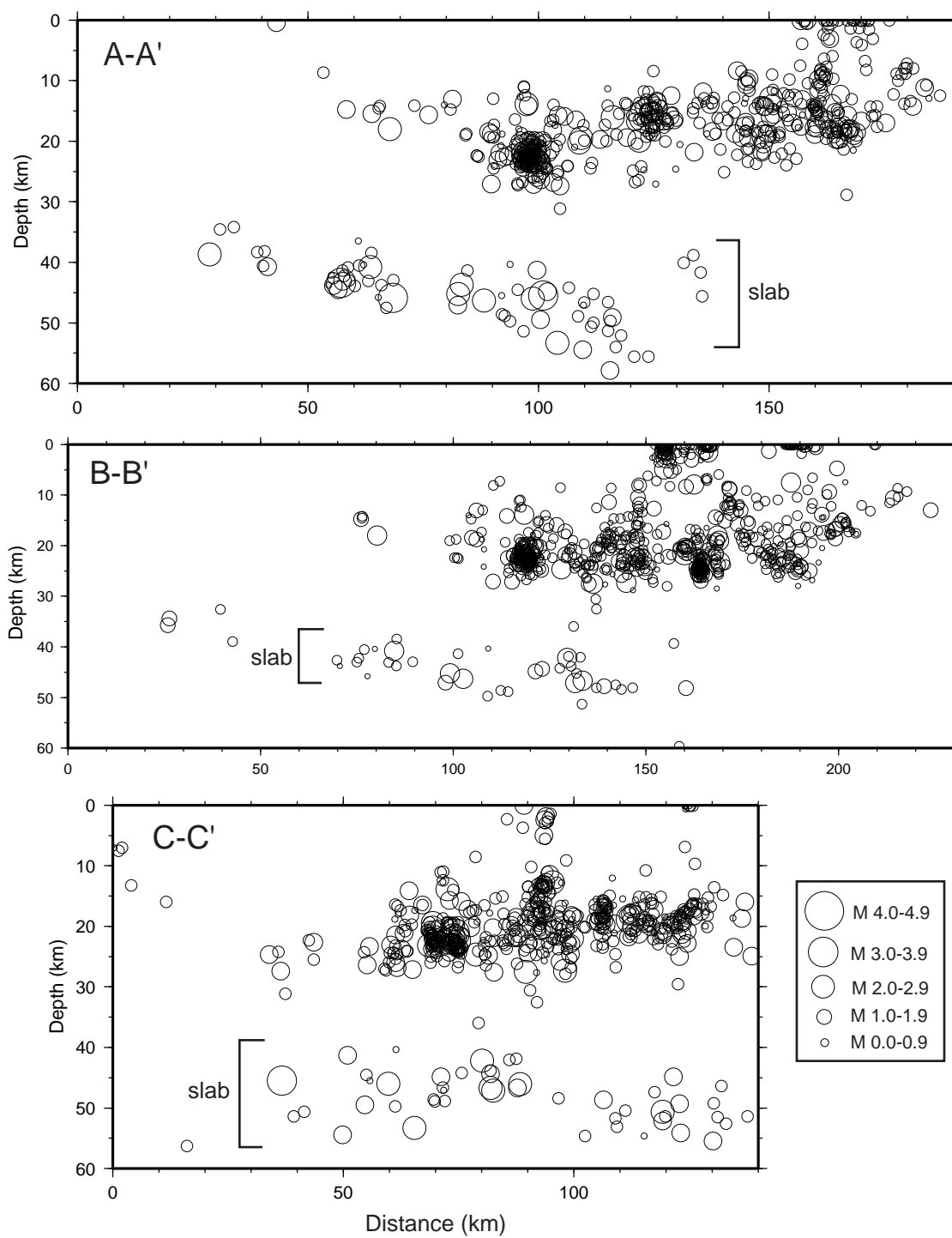


Figure 6: Seismicity cross section along lines A-A', B-B', and C-C' (Figure 5). Earthquakes occurred from 1969 to 1999 and are good quality from the University of Washington database.

lithosphere, within the oceanic mantle, and not at the interface with the North American plate (Taber and Smith, 1985) (Figures 5 and 6). Hypocenters in the subducting Juan de Fuca plate are interpreted as showing that the direction of plate dip changes from northeast beneath the Puget Sound region to east-southeast beneath southwest Washington (Weaver and Baker, 1988, Ludwin et al., 1991). The dip of hypocenter distribution in the subducting slab changes from $\sim 10^\circ$ near the coast to $\sim 20^\circ$ just west of Mount St. Helens (Ludwin et al., 1991). In the Puget Lowland, crustal seismicity is concentrated in the middle to lower crust (Ludwin et al., 1991). This seismicity is diffuse and does not appear to delineate faults.

Juan de Fuca Slab Geometry and Crustal Structure

Active source seismic data also provide constraints on slab geometry. Reflection and refraction data were collected during two different onshore-offshore seismic experiments near Grays Harbor, Washington (Parsons et al., 1998; Taber and Lewis, 1986). Results showed an approximate 9° dip of the subducting oceanic lithosphere, a clear indication of where the slab encounters a ~ 20 km thick block of Siletz terrane and begins to bend, and confirmation of the continuity of the slab (Taber and Lewis, 1986).

Interpretation of refractions and wide-angle reflections from earthquake sources shows that a distinct crustal root lies beneath the Cascades with a depth of 47 km and velocities ranging from ~ 6.0 km/s at 4 km to ~ 6.8 km/s at 20 km

(Schultz and Crosson, 1996). Crustal thickness underneath Puget Sound varies from 30 to 45 km with velocities ranging from 6.0 km/s in the upper 10 km of the crust to ~7.8 km/s at the crust-mantle boundary based on results from active source refraction/reflection (Stanley et al., 1999; Parsons et al., 1999; Miller et al., 1997). A low-velocity (2.5-5.0 km/s) accretionary wedge lies just to the east and underneath the Siletz terrane in the subsurface (Parsons et al., 1999; Symons and Crosson, 1997) and outcrops in the Olympic Mountains (Brandon and Calderwood, 1990). Tomographic inversion of earthquake data suggest that an apparent mantle wedge with velocities of 7.5 to 8.0 km/s lies between the Juan de Fuca subducting plate and the North American crust (Symons and Crosson, 1997).

Crescent Formation and Cascade Range Rocks

The Puget Lowland overlies a major north-trending crustal boundary between the Eocene basement rocks of the Crescent Formation to the west and the pre-Tertiary basement rocks of the Cascade Range to the east. Gravity and magnetic maps show that the Crescent Formation extends from Oregon north up to Vancouver Island, and two-dimensional modeling of these data indicate that these rocks are about 1 km thick at the coast, thickening to as much as 30 km near their postulated Coast Range boundary fault edge (Finn, 1990). Others have studied magnetotelluric (Stanley et al., 1987), seismic refraction and/or wide angle reflection data (Trehu et al., 1994; Schultz and Crosson, 1996), and passive source tomography (Lees and Crosson, 1990) and found that the

Crescent Formation may be thicker than 20 km and as thick as 33 km in some areas.

Pre-Tertiary basement rocks of the Cascades include diverse metamorphic, igneous, and sedimentary rocks that comprise several distinct crustal terranes with exotic origins (Tabor, 1994). Relatively high velocities (6.4-6.8 km/s) were found at midcrustal depth under the Cascades (Schultz and Crosson, 1996). A gravity low over the Cascades suggest low rock densities relative to those in the Coast Range (Finn, 1990). These rocks formed the leading oceanic edge of the North American crust before subduction of the Juan De Fuca plate began (Stanley et al., 1990).

Puget Lowland

A large low velocity anomaly beneath the central Puget Sound coincides with the Seattle basin based on tomographic inversion results (Lees and Crosson, 1990). A recent earthquake tomography study shows velocities at 3.5 to 6.5 km depth to be ~4.5 to 5.0 km/s (Symons and Crosson, 1997). Rock units imaged with seismic reflection data across the Seattle basin can be delineated on the basis of seismic facies characteristics and borehole data (Johnson et al., 1994, 1996; Pratt et al., 1997). In another study, a velocity model calculated at a depth of 2.5 km below sea level shows velocities of ~6.0 km/s in the Tacoma basin area (Parsons et al., 1999).

The Seattle uplift lies in between the Tacoma and Seattle basins (Figure 1). The southern edge of the uplift is defined by strata at an estimated dip of 15°

to 20° assuming a velocity between 3.0 and 4.5 km/s (Pratt et al., 1997). Seismic reflection data (Pratt et al., 1997) show a north dipping Crescent Formation reflector that is the base of the Black Hills uplift. The Crescent Formation appears to be an onlap surface for the younger sedimentary units.

Olympic Mountains have mainly been studied using gravity methods. A large Bouguer gravity low is associated with the Olympic Mountains, which most likely suggest low-density rocks that provide isostatic compensation for the mountains (Finn, 1990; Pratt et al., 1997).

Site Response

Reliable estimates of amplification in regions underlain by a basin or unconsolidated sediments remains a challenge. Only recently have researchers begun to study ground motion amplification of earthquakes due to these basins and unconsolidated sediments. Different factors must be considered when analyzing the site response of an area including lithology, basin shape, and earthquake azimuth. Modeling results include estimates of the magnitude of amplification of seismic energy and coherence of ground motion. As models become more reliable, scientists will be able to estimate ground motion and subsequent damage to structures.

The most common method used in site response analysis is the comparison of spectral amplitudes between a reference site and a basin site. A reference site must be located on competent bedrock in hopes of observing the equivalent of the input waveform at the bedrock-sediment contact (Steidl et al., 1996) (Figure 7). The reference site and basin site responses are transformed to frequency and compared to each other to estimate the amplification at the basin site. Finding a good reference site is often a challenging task, so other methods that are reference site independent have been developed and applied to site response analysis. One of these is a parameterized source and path effect inversion outlined by Boatwright et al., (1991) and Field and Jacob (1995). Another method involves a receiver-function

Empirical and Theoretical Estimates of GVDA Site Response

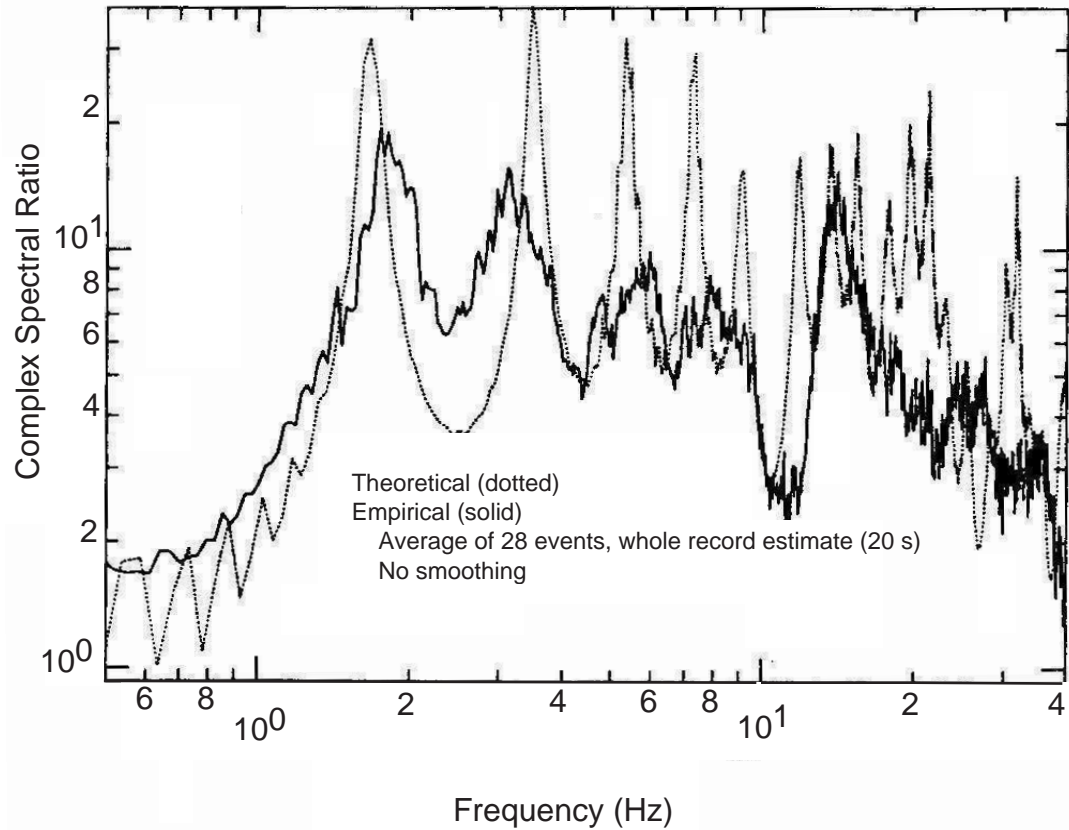


Figure 7: Comparison between the empirical (solid curve) and theoretical (dotted curve) estimates of site response. From Steidl et al., 1996.

type estimate which involves taking horizontal to vertical component ratios of the shear wave spectra (Lermo et al., 1993; Field and Jacob, 1995).

The main objective in site response analysis is to estimate how much a basin amplifies seismic energy. Amplification estimates in many basins on the west coast of the United States show amplification factors of up to 15 times greater than that of the input motion (e.g. Boatwright et al., 1991; Carver and Hartzell, 1996; van de Vrugt et al., 1996). Further investigation shows these amplifications occur at certain frequencies or within certain frequency ranges (e.g. Boatwright et al., 1991; Hartzell et al., 1998). Many areas show the highest amplifications around 1 Hz with decreasing amplification at higher frequencies (e.g. Graves, 1993; Hartzell et al., 1998). Research shows that longer period waves are primarily affected by the geometry and structure of the basin (e.g. Graves, 1993), whereas shorter period waves are affected by smaller localized structures and shallow subsurface variations (e.g. Boatwright et al., 1991; Steidl et al., 1996; Hartzell et al., 1998).

The effects of basin geometry have been shown to have a major effect in simulation studies. Simulations with sample models are done in order to match observed site responses and to estimate what might happen from different sources. One-dimensional models follow the pattern of amplification shown by other studies (e.g. Boatwright et al., 1991), that is, higher amplifications occur at lower frequencies and decrease in amplitude as frequencies increase. However, the 1-D model calculations often severely underestimate amplifications at lower

frequencies and match up better at higher frequencies (Boatwright et al., 1991). Because the simulations lack information on basin geometry they do not account for increased duration of shaking and lateral interferences (Graves, 1993; Zhang and Papageorgiou, 1996). Two-dimensional models compare favorably with observed site response results in terms of amplitude, duration, and frequency content (Zhang and Papageorgiou, 1996). The only drawback to these is in accounting for arrivals from azimuths that are out of a plane. Analysis of site response using 3-D models does a good job of accounting for direction of propagation that affects amplification and duration of shaking (Graves, 1993; Wald and Graves, 1998).

Depth of a basin is critical in amplification simulations. Higher amplifications have been found to coincide with the deepest part of a basin (e.g., Hartzell et al., 1998). Extended periods of shaking and higher amplifications have also been attributed to basin edge induced waves (surface waves) (Carver and Hartzell, 1996; Field, 1996). Moreover, varying azimuth of the incident wave field and location of stations will show different durations and amplitudes (Graves, 1993).

Topography, unconsolidated sediments, and localized structures, such as small anticlines, focus and defocus energy and create additional complications in estimating site response (Hartzell et al., 1998; Hough and Field, 1996; van de Vrugt et al., 1996). In the Los Angeles area, Meremonte et al. (1996) found ground motion variabilities up to a factor of 2 over distances as small as 200 m

for sites on the same mapped soil unit. Critical and postcritical reflections from the Moho and crustal layers caused increased shaking at discrete distances along the San Francisco peninsula during the 1989 Loma Prieta earthquake (Catchings and Kohler, 1996). Sites closer to the epicenter on bay muds experienced much less shaking than sites on hard rock that were farther from the epicenter. This indicates that epicentral distances have an effect on site responses regardless of subsurface geology (Catchings and Kohler, 1996).

Seismic Data Acquisition and Analysis

In March of 1998, deep-crustal wide-angle seismic reflection and refraction data acquisition for SHIPS was completed with the objective of developing a comprehensive 3-D velocity model of the Puget Lowland. Approximately 33,000 shots were fired at 16 second intervals from an airgun array of 6700 in³, that was towed by the R/V Thompson through Puget Sound, Hood Canal, Lake Washington, the Strait of Juan de Fuca, and the Strait of Georgia. A 2.4-km streamer towed by the R/V Thompson, 15 ocean-bottom seismographs, 257 Reftek recorders, and 71 permanent seismic stations recorded data (Fisher et al., 1999) (Figure 2).

The Reftek recorders consisted of five components that included (1) Data Acquisition System (DAS), (2) internal or external hard disk drive, (3) internal oscillator and internal or external GPS clock, (4) 3-component seismometer, and (5) two external 12-V batteries that supplemented a small internal battery (PASSCAL, 1991). These two external batteries were essential for carrying out continuous recording over the 18-day period of the experiment. The Reftek DAS was monitored and programmed using Palm-Top HP terminals or hand held terminals. Seismometer locations were determined from internal GPS receivers and from digital topographic maps, and elevations were also determined from digital topographic maps (Brocher et al., 1998). Latitudes and longitudes for the seismometers have an accuracy of about 50 m while the elevations are accurate

to approximately 10 m (Brocher et al., 1998). Station spacing ranged from 5 to 15 km and shot spacing ranged from 50 to 150 m.

Data were reduced and archived as receiver gathers in SEG-Y format with geometry in the headers. Eleven different trace files were archived for each station corresponding to the 11 different shot lines that were created from the continuous path of the R/V Thompson. Traces are 90 seconds long with a sample rate of 100 Hz. Source-receiver offsets were recorded from as small as 1 km to as large as 370 km while useable data from most seismometers was picked up for source-receiver offsets of at least 40 to 50 km (Brocher et al., in review). Signals in urban or suburban areas were harder to detect due to the noise level, and seismometers deployed in the eastern Cascades were too far from air gun shots to provide interpretable data (Brocher et al., in review).

This study focuses on data from 61 land stations from the array in and around the Tacoma Basin (black box in Figure 2). Of the 11 shot lines defined by the USGS, this study focuses on lines 2, 3, and 9 (Figure 2). Only shots and receivers in the designated model space can be used in the tomography, and these 3 lines are the only of the 11 lines that enter the model space.

Seismic Data

Representative receiver gathers from the experiment (Figures 8-12) were reduced at 6 km/s and had a 2-20-10-30 Butterworth filter applied to them to enhance first arrivals, particularly at far offsets. The filter caused a phase shift of less than 20 ms which was taken into account when picking first arrivals. These gathers show first arrival energy to offsets averaging 50 km and secondary arrivals that contain significant amounts of multiple energy.

Preliminary analysis of the seismic record sections shows the first order variations in velocity and subsurface structure. First arrivals on station C3008 (Figure 8) exhibits some typical velocity variations. Starting at ~20 km offset and moving north, velocities decrease and a 1 s travel time delay occurs for shots in the Seattle basin. Low apparent velocity in the Seattle Basin (~4.5 to 5 km/s) can also be seen on station C3011 beginning around 30 km and moving northward (Figure 9). The shallower, higher velocity (~5 to 5.5 km/s) Seattle uplift is evident on stations C3008 between 2 and 20 km, C3011 between 8 and 30 km, and C3014 between 10 and 40 km (Figure 10). Delays in the first arrivals also occur in the Tacoma basin. The best indication of the Tacoma basin is seen on station C3008 beginning around -15 km and moving south. Stations C3011 and C3014 show evidence of the Tacoma basin in the direct wave arrivals.

Shot line 3, located in the Hood Canal area (Figure 2), also shows pronounced travel time variations due to subsurface structure. Station D4010

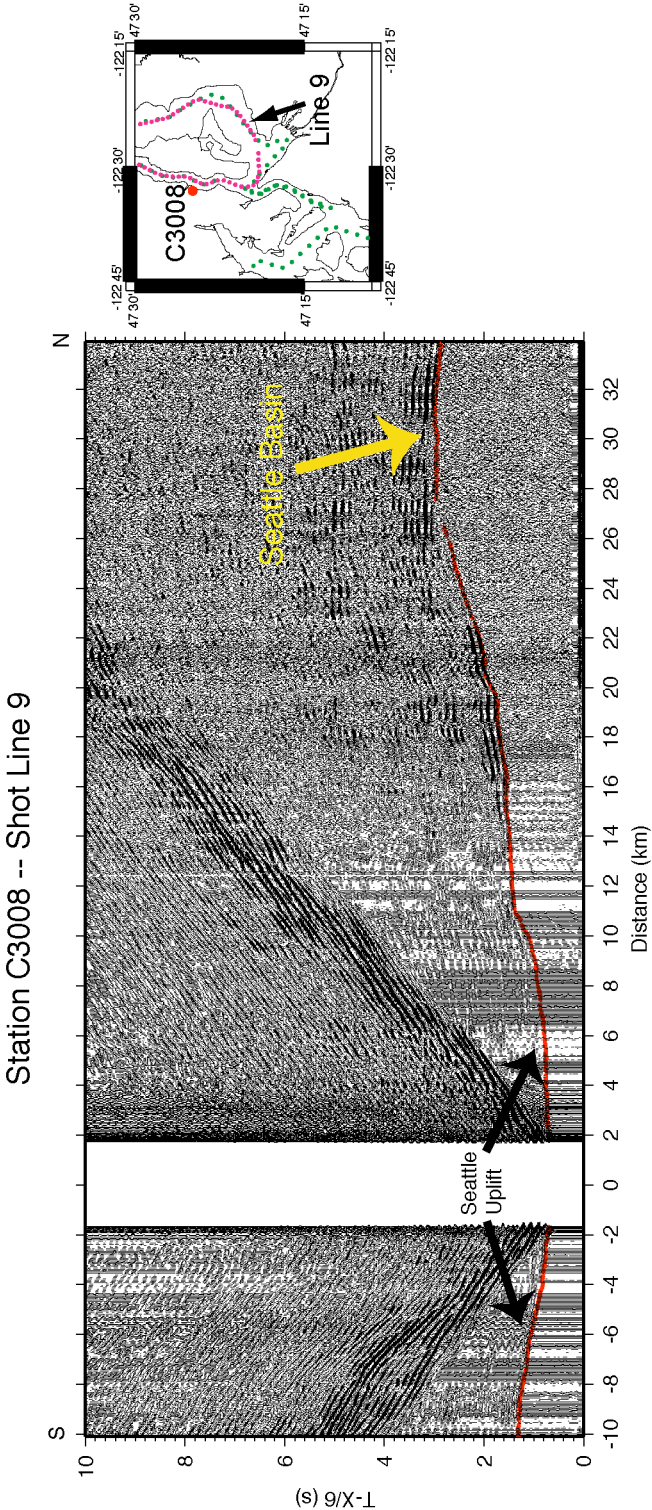


Figure 8: Filtered seismic data from line 9 acquired at station C3008. Travel time is reduced at 6 km/s . A 2-20-10-30 Butterworth filter has been applied to remove noise. The red line shows first arrival picks. Travel time delays due to the Seattle basin and the Seattle uplift are annotated.

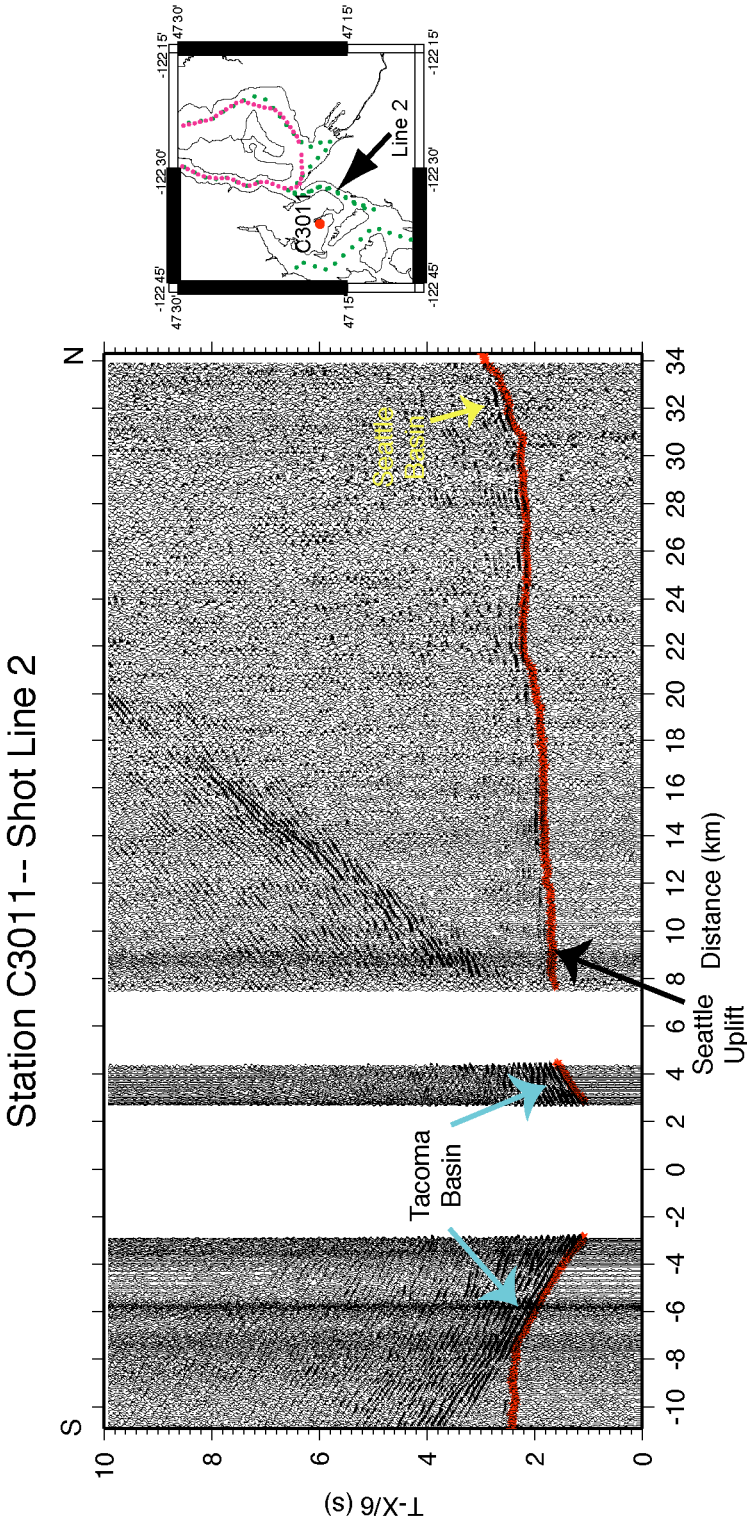


Figure 9: Filtered seismic data from line 2 acquired at station C3011. Travel time is reduced at 6 km/s. A 2-20-10-30 Butterworth filter has been applied to remove noise. The red line shows first arrival picks. Travel time delays due to the Seattle and Tacoma basins, and the Seattle uplift are annotated.

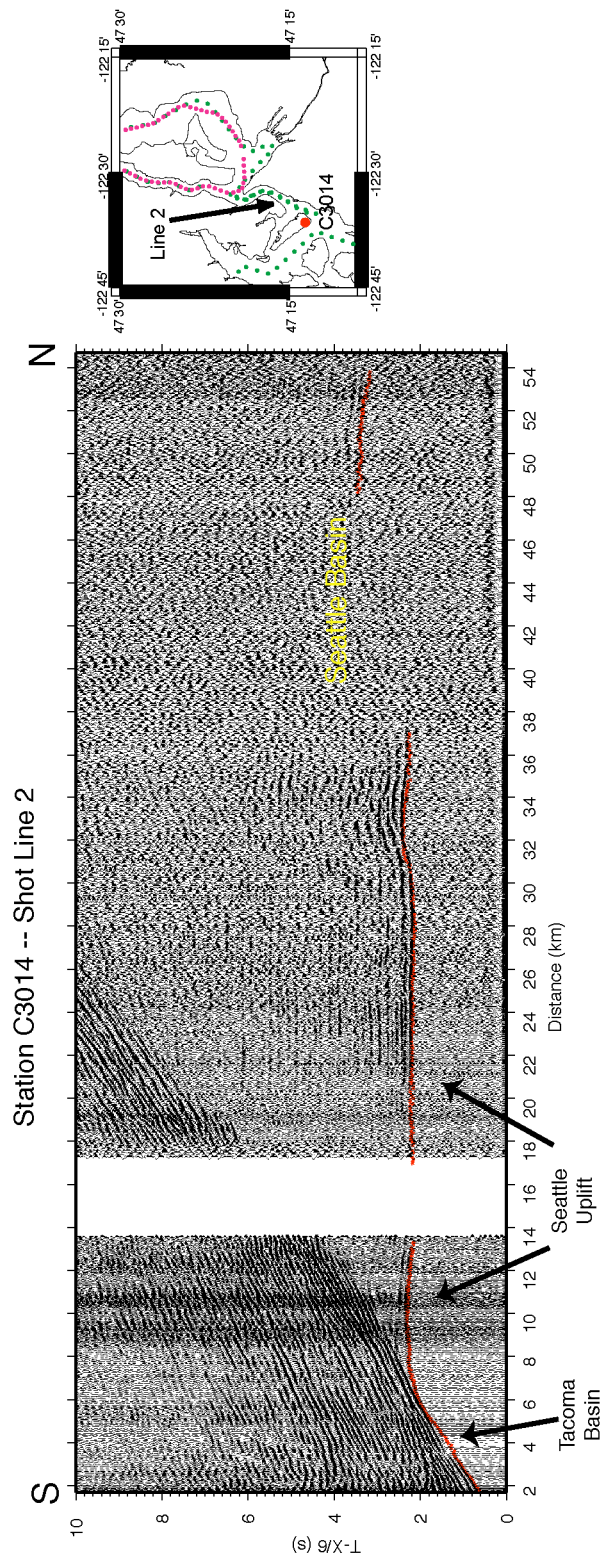


Figure 10: Filtered seismic data from line 2 acquired at station C3014. Travel time is reduced at 6 km/s. A 2-20-10-30 Butterworth filter has been applied to remove noise. the red line shows first arrival picks. Travel time delays due to the Seattle and Tacoma basins and the Seattle uplift are annotated.

shows low velocities (~ 4 to 4.5 km/s) from ~ 20 to 30 km which could represent the western most edge of the Seattle basin (Figure 11). Station D4011 exhibits this apparent velocity beginning around 25 km (Figure 12). First arrivals show basin velocities from ~ 3 to 6 km offset on D4010 and from ~ 3 to 8 km on D4011. Basin velocities (~ 4 to 4.5 km/s) are shown very well on the south side of D4010 while higher velocities (~ 5.0 km/s) are evident on the south side of D4011. These higher velocities do not appear to be fast enough to indicate Crescent Formation, but they may possibly indicate the edge of the basin.

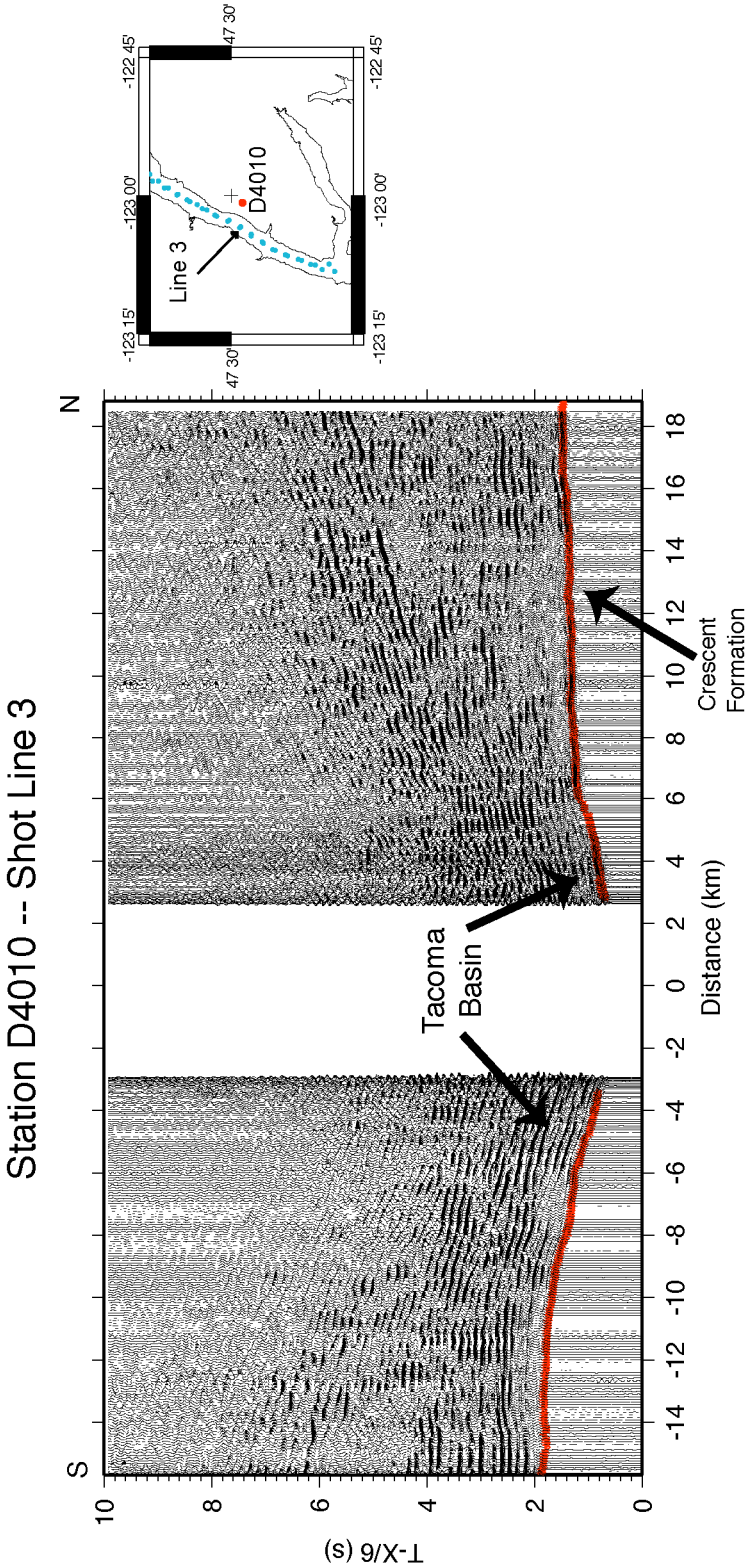


Figure 11: Filtered seismic data from line 3 acquired at station D4010. Travel time is reduced at 6 km/s. A 2-20-10-30 Butterworth filter has been applied to remove noise. the red line shows first arrival picks. Travel time delays due to the Tacoma basin and Crescent Formation arrivals are annotated.

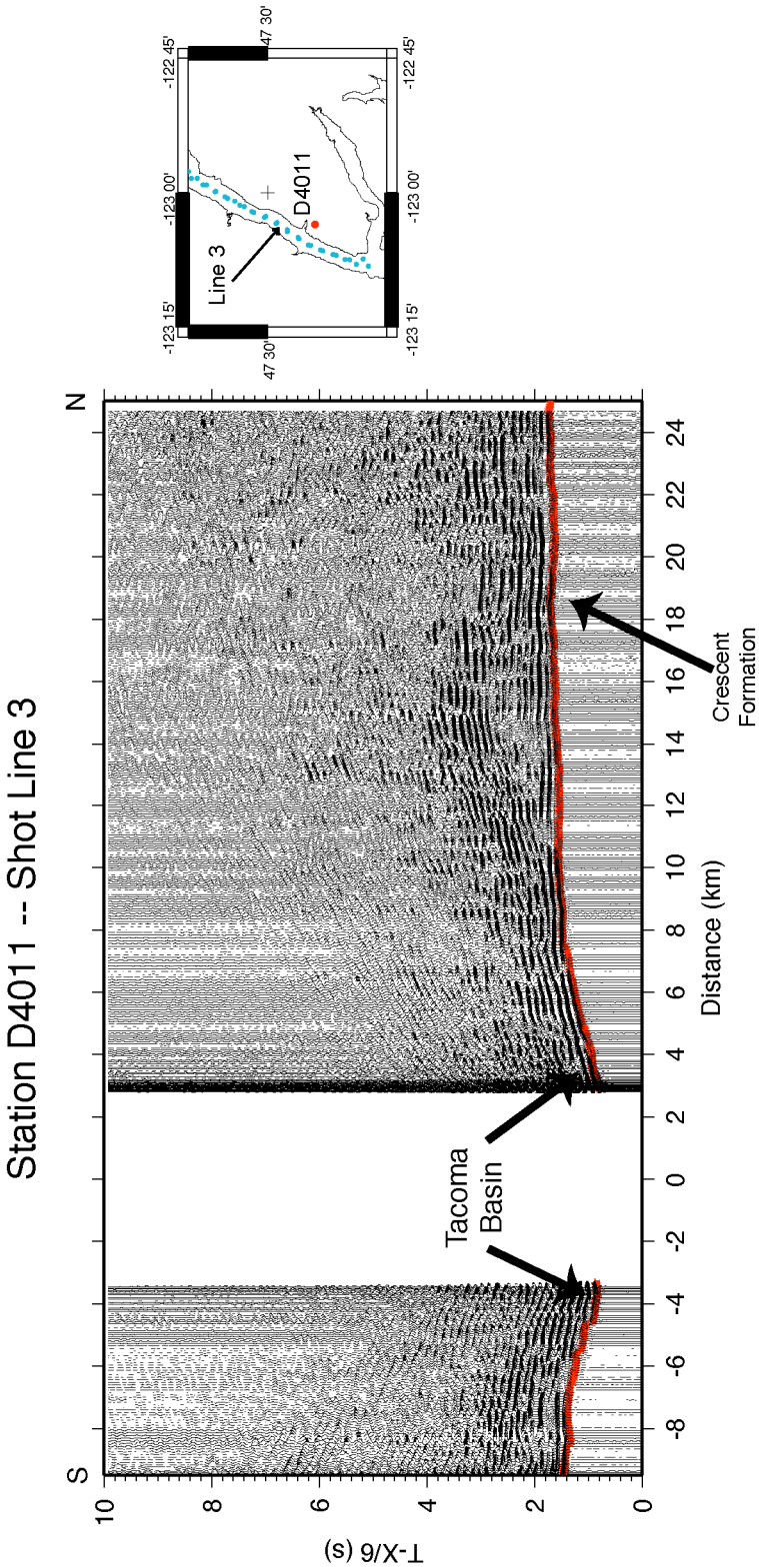


Figure 12: Filtered seismic data from line 3 acquired at station D4011. Travel time is reduced at 6 km/s. A 2-20-10-30 Butterworth filter has been applied to remove noise. the red line shows first arrival picks. Travel time delays due to the Tacoma basin Crescent Formation arrivals are annotated.

Tomography

The large data volume together with the 3-D geometry of the experiment requires a 3-D tomographic approach for deriving a velocity model for the Tacoma basin. We chose to use a nonlinear high resolution 3D travel time tomography that is computationally time efficient and can account for large velocity contrasts (Hole, 1992).

First arrival travel times are computed through a user defined starting velocity model using a finite difference approximation to the eikonal equation (Vidale, 1988; Vidale, 1990). The starting velocity model is a uniformly spaced set of grid points in three dimensions. First arrival travel times are computed to all grid points in the model by a finite difference operator that uses the average slowness across a grid cell. Rays are found by tracing backward from the receivers through the computed travel time field. Thus, the travel time field can be used to trace rays from any number of receivers located anywhere in the model for a single source.

The inversion for velocity relies on linearization of the eikonal equation with a Taylor series expansion that ignores higher order terms. This results in a linear relationship between residual travel times and changes made to a velocity model that must be solved iteratively. The approach is non-linear in that travel times are recalculated through the new model after each inversion. The basic steps in the inversion procedure are (1) an input 1-D velocity model is used to calculate initial ray paths, (2) the inversion minimizes the difference between

observed calculated travel times to produce a slowness perturbation model, (3) the original velocity model is updated with the slowness perturbation model and is smoothed using a 3-D moving average filter, and (4) the new output velocity is input to the next round of travel time calculation, inversion, update, and smoothing. This procedure is stopped when there is no significant reduction in the rms travel time error from one model to the next.

Inversion Parameters

The inversion code requires a choice of a number of parameters including a coordinate system, cell size, starting model, and smoothing parameters. After an examination of a map of shot and receiver locations, a model space with corners -123.5° longitude, 46.875° latitude (origin) and -121.75° longitude, 47.625° latitude (opposite corner) was chosen. Shots and receivers within this area were all transformed to an x-y coordinate system, using a Lambert projection.

Because of the large scale of this experiment and the station separation, a cell size of 1 km^3 was chosen. Cell sizes below 1 km^3 were chosen for the computations initially, but the numerical arrays were too large for the program and computer to handle. A 3-D regridding factor was chosen to reduce computation time during the inversion step. When using all offsets in the model space, a regridding of $2 \times 2 \times 1$ (in km) was chosen.

An initial 1-D velocity model (Figure 13) was chosen based on previous studies (Parsons et al., 1999; Symons and Crosson, 1997; Lees and Crosson, 1990; Pratt et al., 1997). This 1-D velocity model is transformed to 3-D by a simple program so it fits the 3-D Hole code format. The ability of the finite difference algorithm to calculate travel times for all ray paths is extremely input model dependent. For example, faster velocities at shallower depths led to rays that were traced out of the model space.

Three-dimensional smoothness operators were chosen for each run. To begin, an operator was selected to be $1/3$ to $1/2$ the size of the model space in all directions and square in the x-y plane. A beginning smoothness operator of $60 \times 60 \times 10$ was chosen for a model space of $132 \times 85 \times 24$ km. After each run of 15 iterations, the smoothness operators were essentially cut in half in the X-Y plane and reduced by 2 in the Z-plane. The 6th run resulted in a final smoothing factor of $2 \times 2 \times 2$ km. Normally, 15 iterations were performed for each smoothness operator with an rms calculated for each iteration. The rms error was plotted versus iteration number (Figure 14) and the next model is selected based upon where the curve begins to flatten out. For example, in figure 14, the third iteration might be chosen to be used in the next run with the smaller smoothing factor.

Layer stripping was also performed with the data, and pick offsets were reduced to 60, 40, and 20 km. The rms error of these models is smaller than the

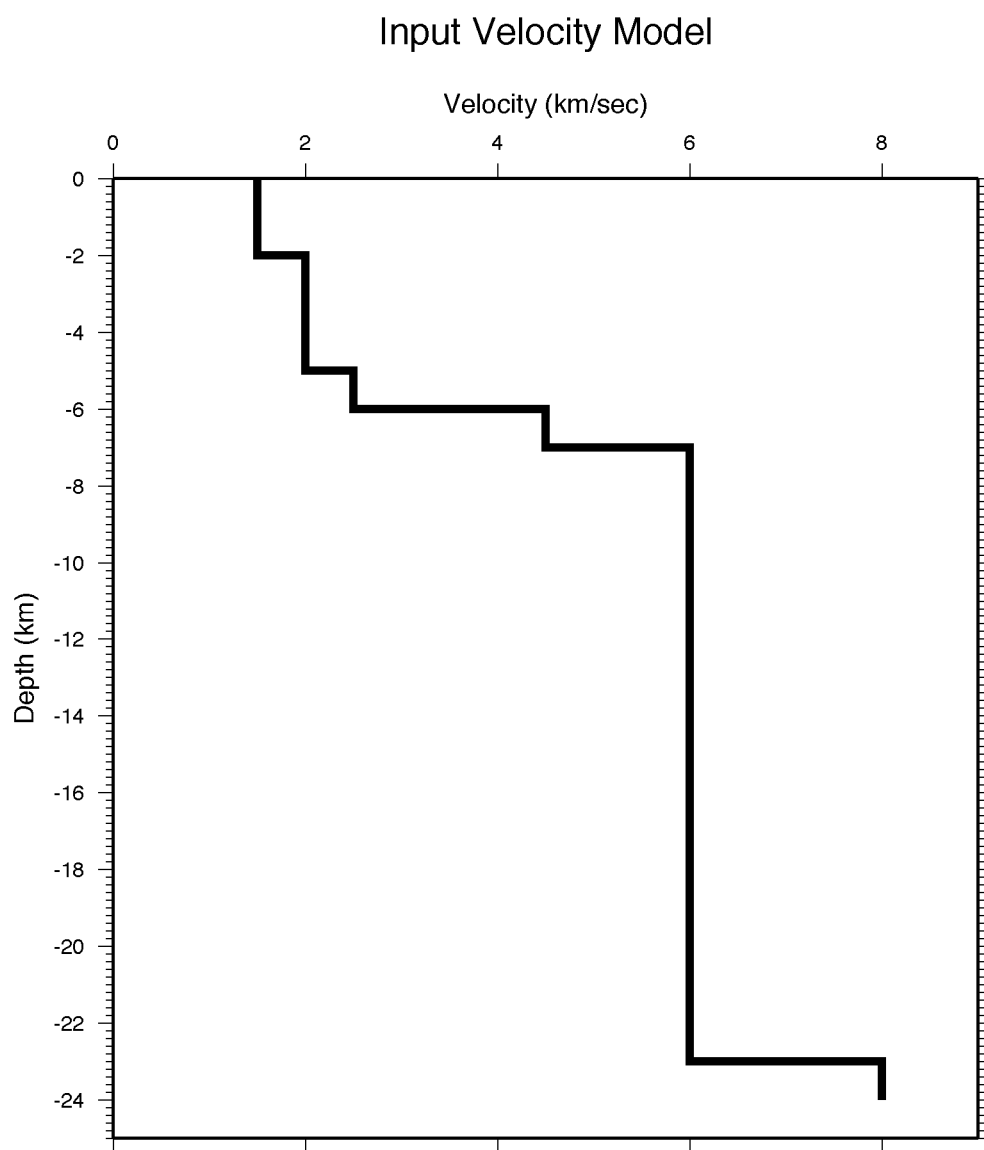


Figure 13: 1-D velocity model used as the starting model for the inversion.

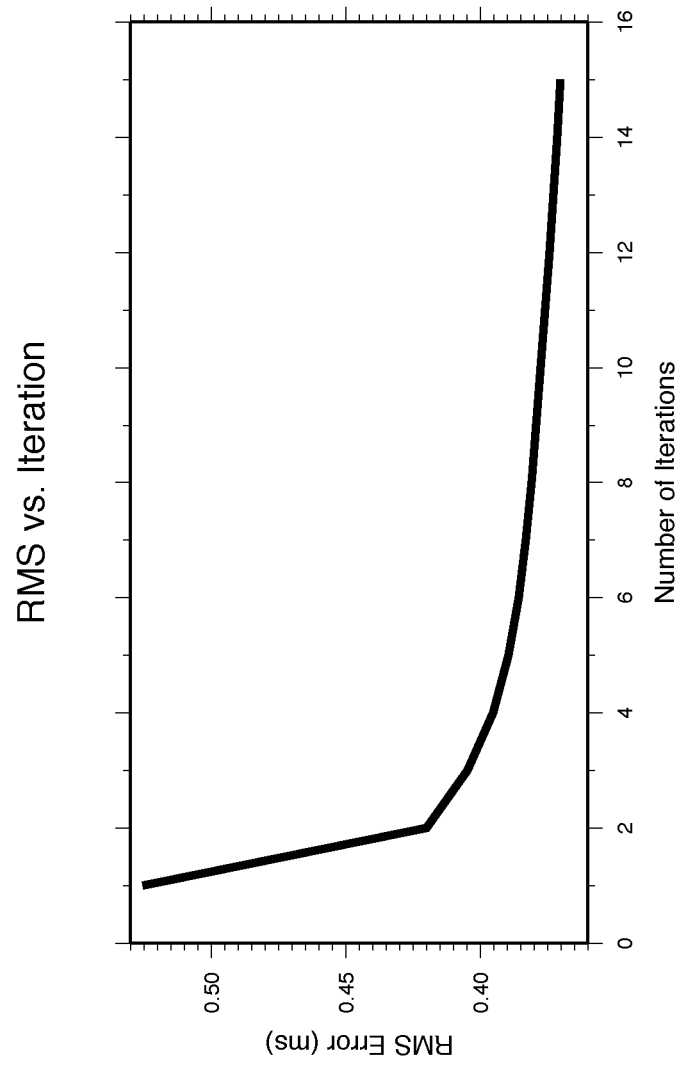


Figure 14: Plot of rms error vs. iteration. The third iteration would be taken for the next run.

rms error of the entire model. By using only those picks at smaller offsets, the error becomes smaller because the ray coverage and calculations are better. The rms errors ranged from 74 ms using 20 km offsets, to 70 ms using 40 km offsets, and to 73 ms using 60 km offsets.

Residuals

Residuals were calculated for each station to help determine where results of the tomography might be less reliable. Figures 15-26 show observed, calculated, and residual travel times. Because of the 1 km cells used in the tomography, the velocity will be affected more by whatever rock is dominant in that cell. This may, in turn, make some cell velocities slower (or faster) depending on the rock composition and create travel times that do not correlate well. If a cell that contains high and low velocity rock is dominated by the slower rock, the overall velocity in the grid will be slower and result in larger travel times. Rays that travel through the part of the grid where the higher velocity rock is located would not be calculated with that velocity, but the slower average velocity. Some stations exhibit this effect (e.g. Figure 15, stations C3008-C3010) at close offsets. Cells at near offsets will be dominated by rock and not the lower velocity water resulting in travel times that arrive earlier.

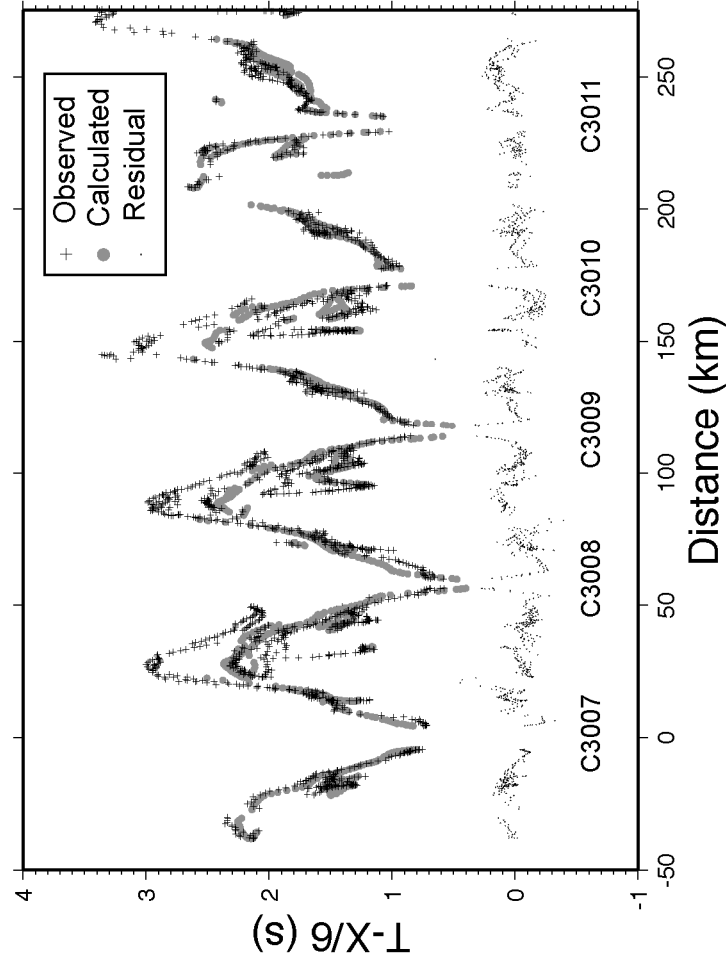


Figure 15: Observed, calculated, and residual travel time plots from stations C3007, C3008, C3009, C3010, and C3011. Offsets of less than 50 km are plotted. Observed picks are denoted as the black plus signs, calculated are the gray circles, and residuals are the black points.

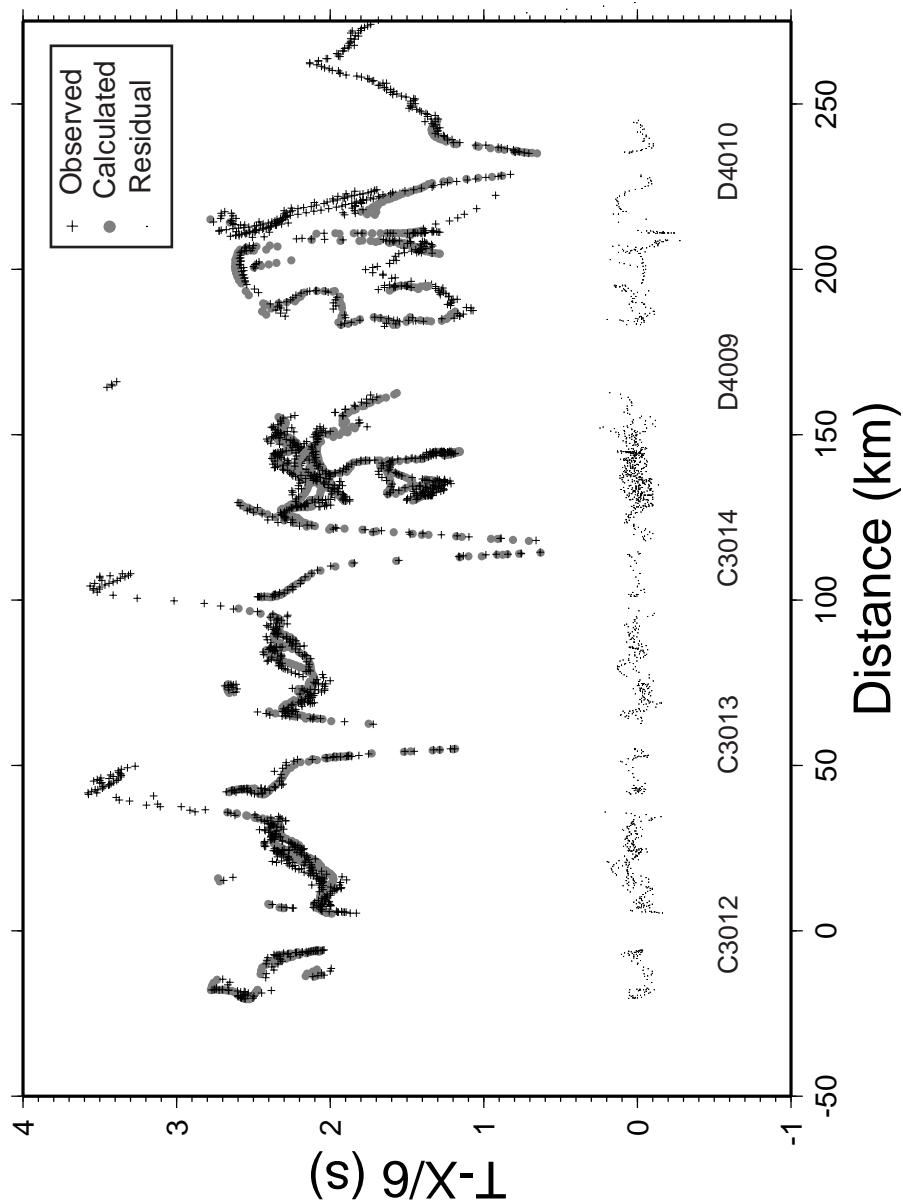


Figure 16: Observed, calculated, and residual travel time plots from stations C3012, C3013, C3014, D4009, and D4010. Offsets of less than 50 km are plotted. Observed picks are denoted as the black plus signs, calculated are the gray circles, and residuals are the black points.

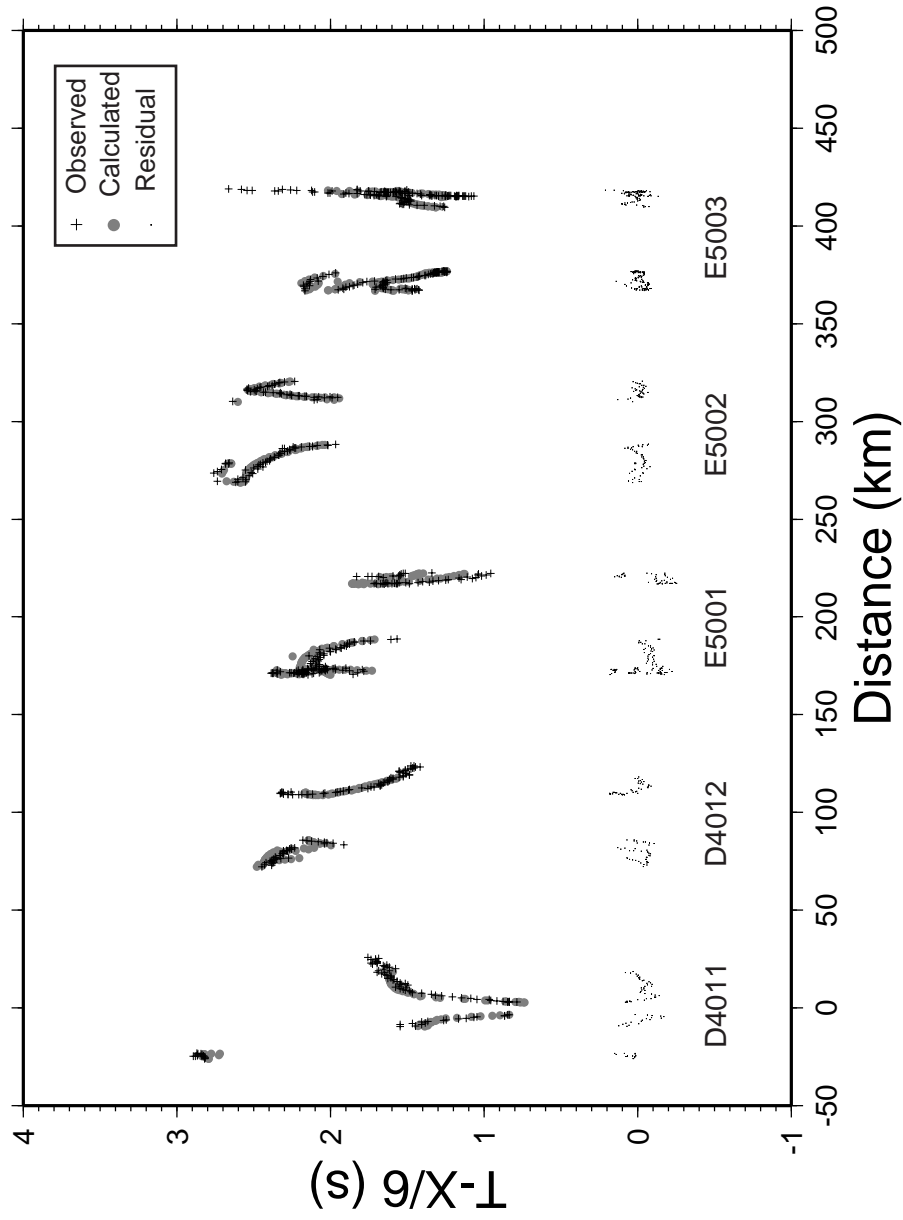


Figure 17: Observed, calculated, and residual travel time plots from stations D4011, D4012, E5001, E5002, and E5003. Offsets of less than 26 km are plotted. Observed picks are denoted as the black plus signs, calculated are the gray circles, and residuals are the black points.

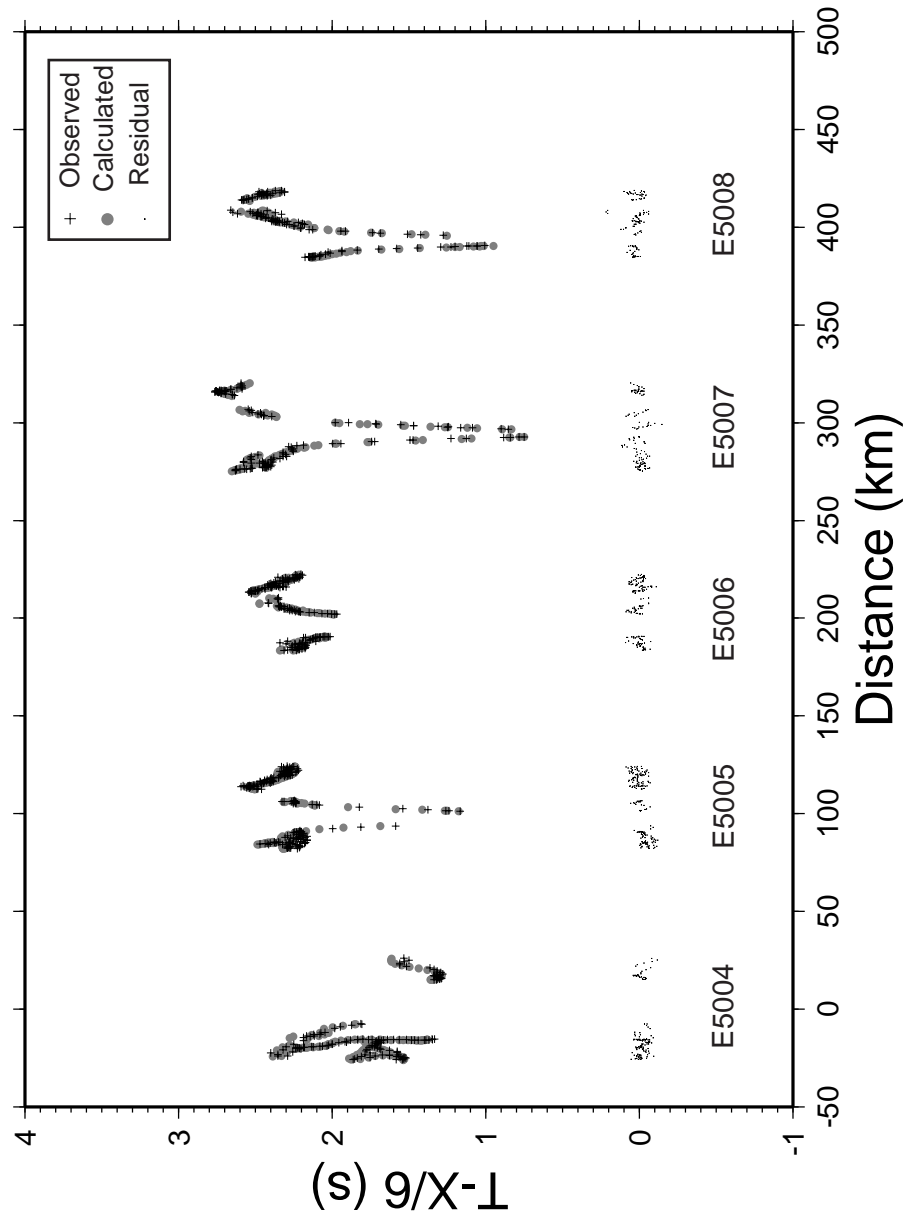


Figure 18: Observed, calculated, and residual travel time plots from stations E5004, E5005, E5006, E5007, and E5008. Offsets of less than 26 km are plotted. Observed picks are denoted as the black plus signs, calculated are the gray circles, and residuals are the black points.

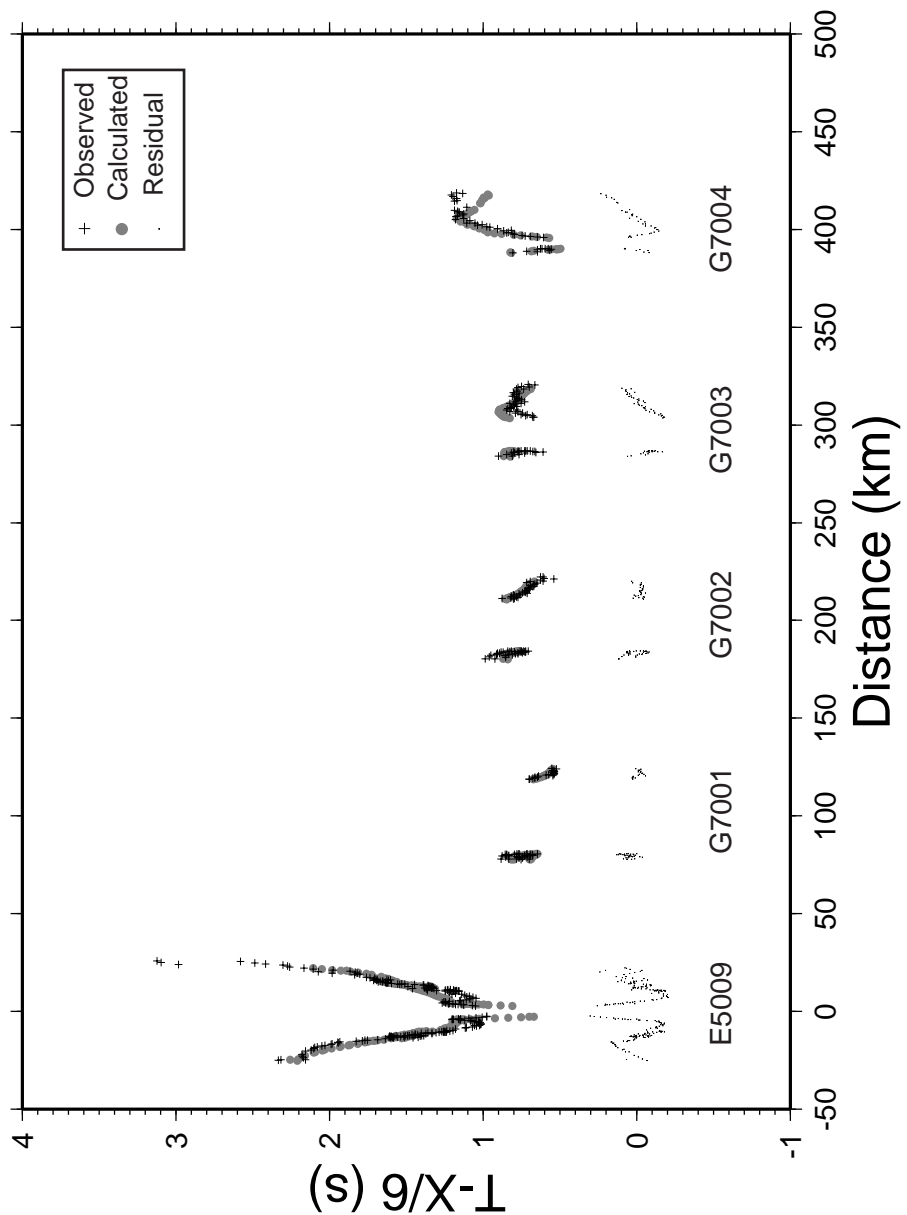


Figure 19: Observed, calculated, and residual travel time plots from stations E5009, G7001, G7002, G7003, and G7004. Offsets of less than 26 km are plotted. Observed picks are denoted as the black plus signs, calculated are the gray circles, and residuals are the black points.

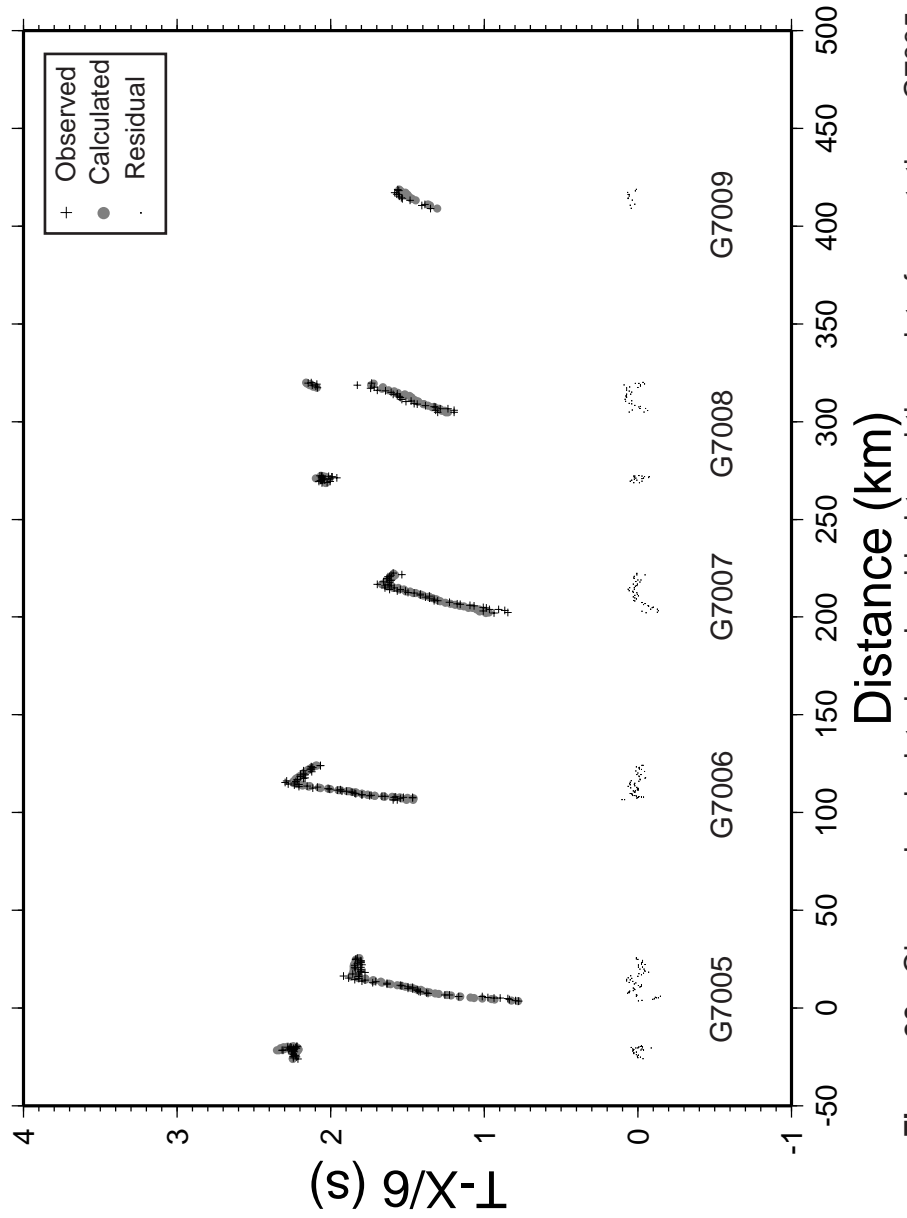


Figure 20: Observed, calculated, and residual travel time plots from stations G7005, G7006, G7007, G7008, and G7009. Offsets of less than 26 km are plotted. Observed picks are denoted as the black plus signs, calculated are the gray circles, and residuals are the black points.

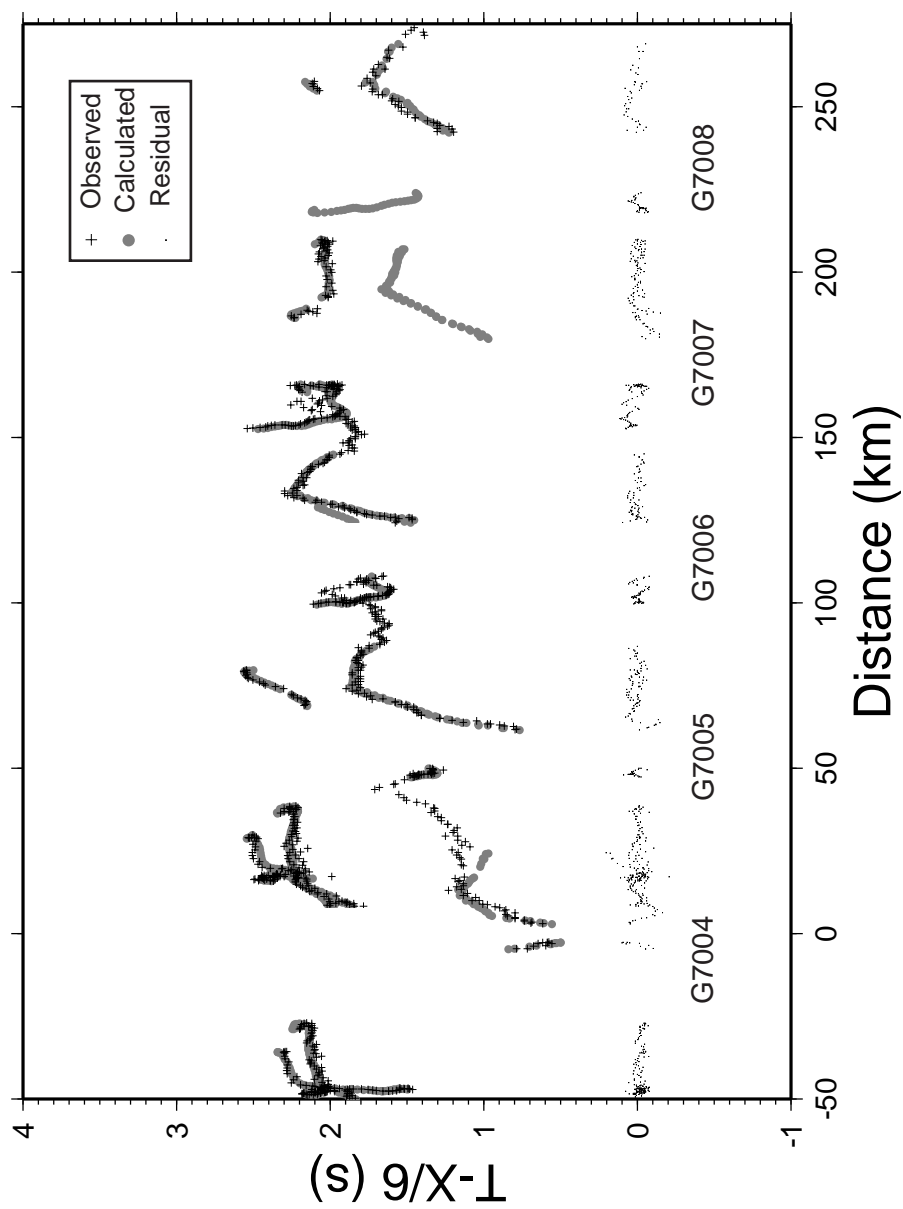


Figure 20: Observed, calculated, and residual travel time plots from stations G7004, G7005, G7006, G7007, and G7008. Offsets of less than 50 km are plotted. Observed picks are denoted as the black plus signs, calculated are the gray circles, and residuals are the black points.

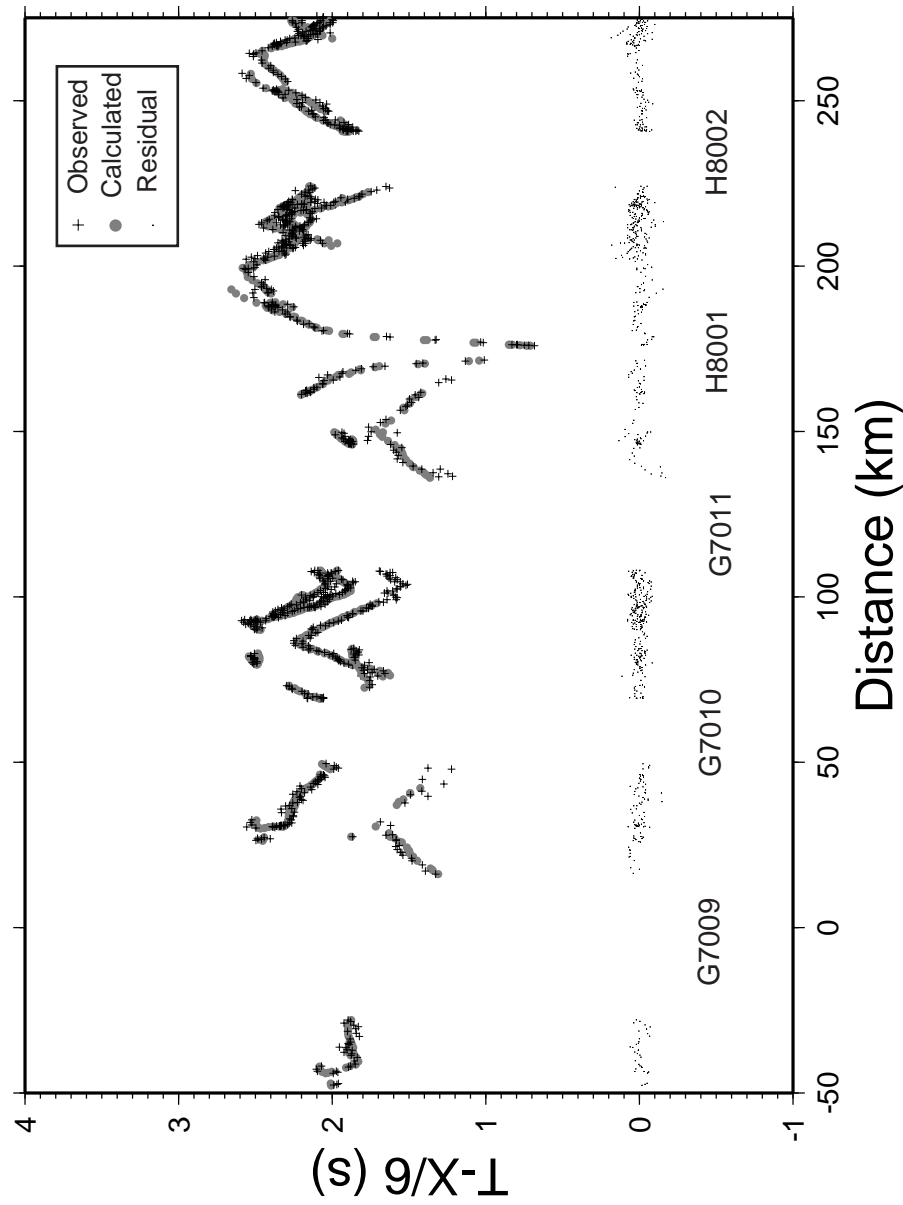


Figure 21: Observed, calculated, and residual travel time plots from stations G7009, G7010, G7011, H8001, and H8002. Offsets of less than 50 km are plotted. Observed picks are denoted as the black plus signs, calculated are the gray circles, and residuals are the black points.

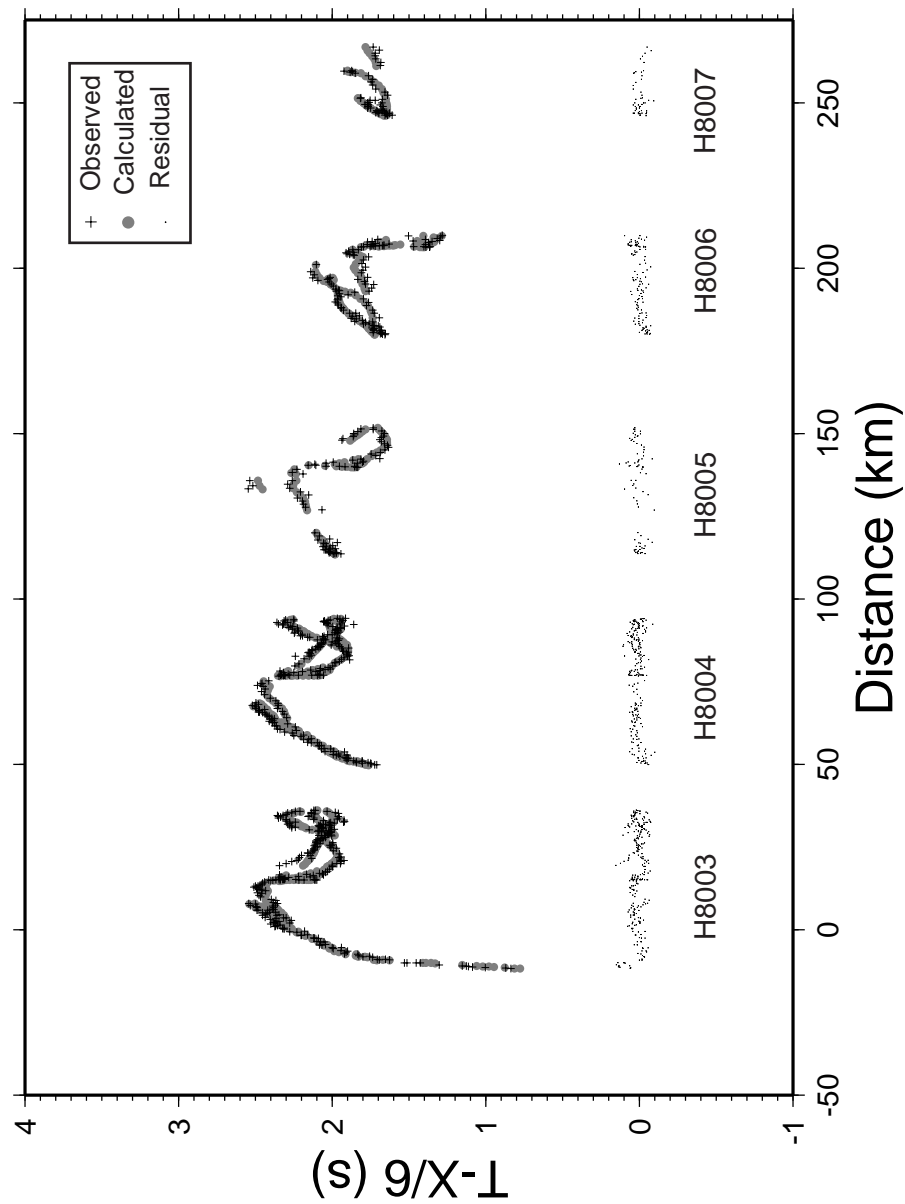


Figure 22: Observed, calculated, and residual travel time plots from stations H8003, H8004, H8005, H8006, and H8007. Offsets of less than 50 km are plotted. Observed picks are denoted as the black plus signs, calculated are the gray circles, and residuals are the black points.

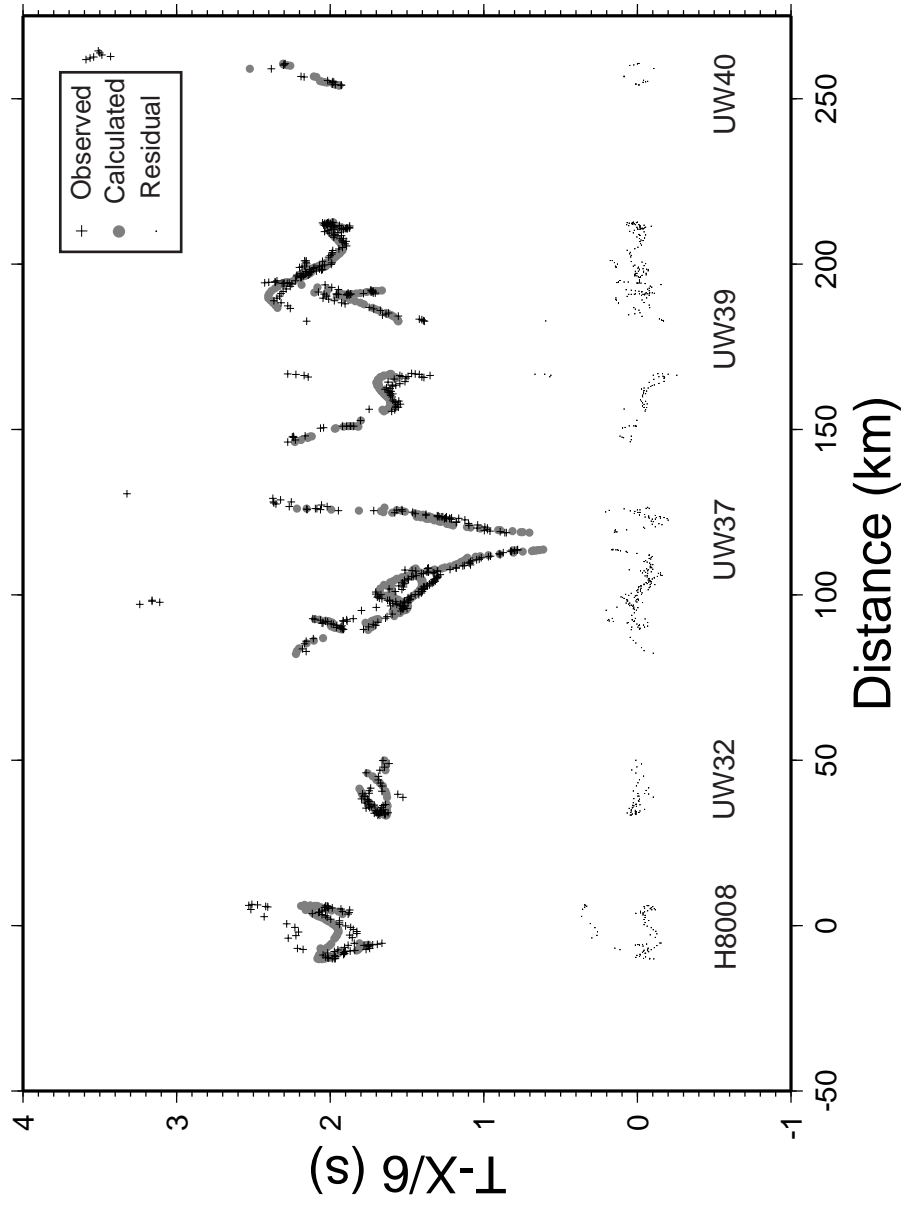


Figure 23: Observed, calculated, and residual travel time plots from stations H8008, UW32, UW37, UW39, and UW40. Offsets of less than 50 km are plotted. Observed picks are denoted as the black plus signs, calculated are the gray circles, and residuals are the black points.

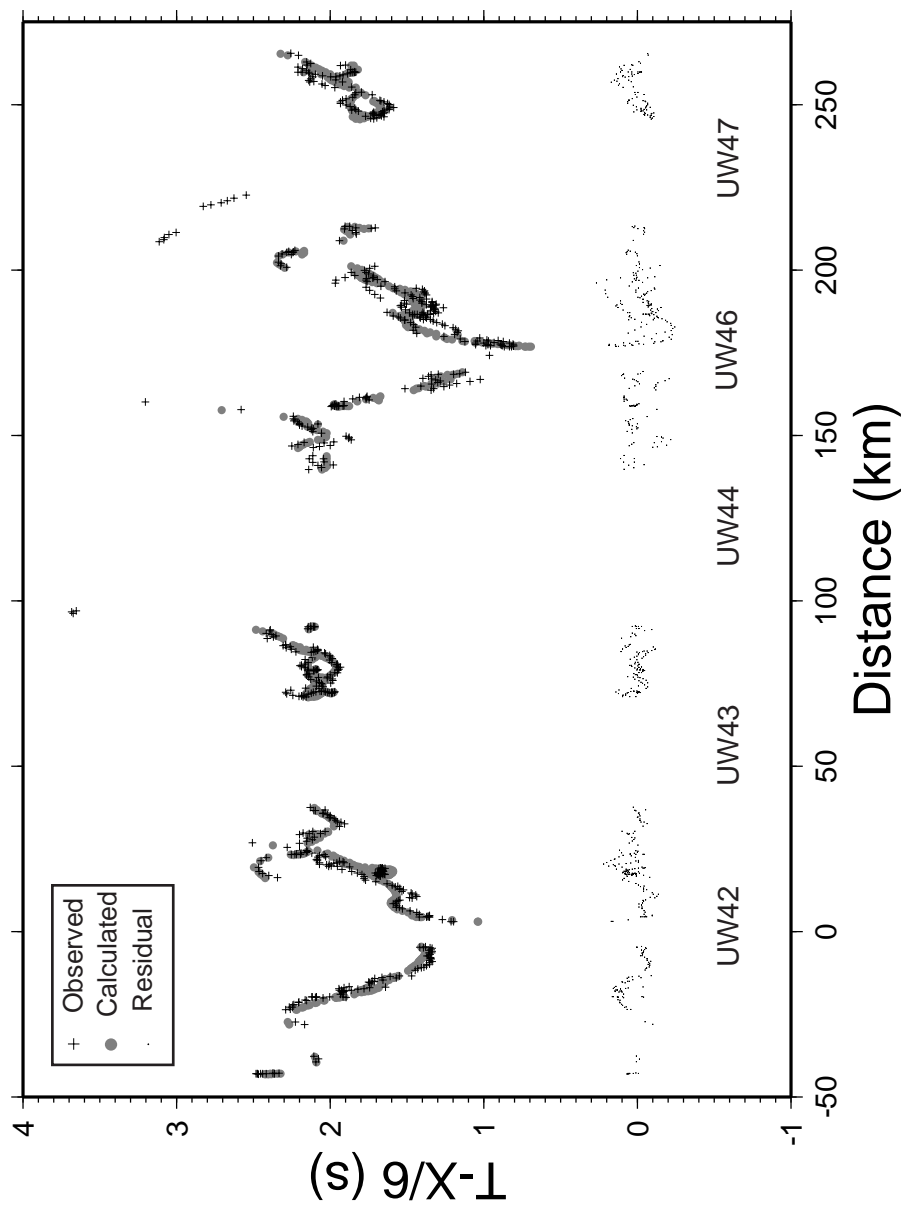


Figure 24: Observed, calculated, and residual travel time plots from stations UW42, UW43, UW44, UW46, and UW47. Offsets of less than 50 km are plotted. Observed picks are denoted as the black plus signs, calculated are the gray circles, and residuals are the black points.

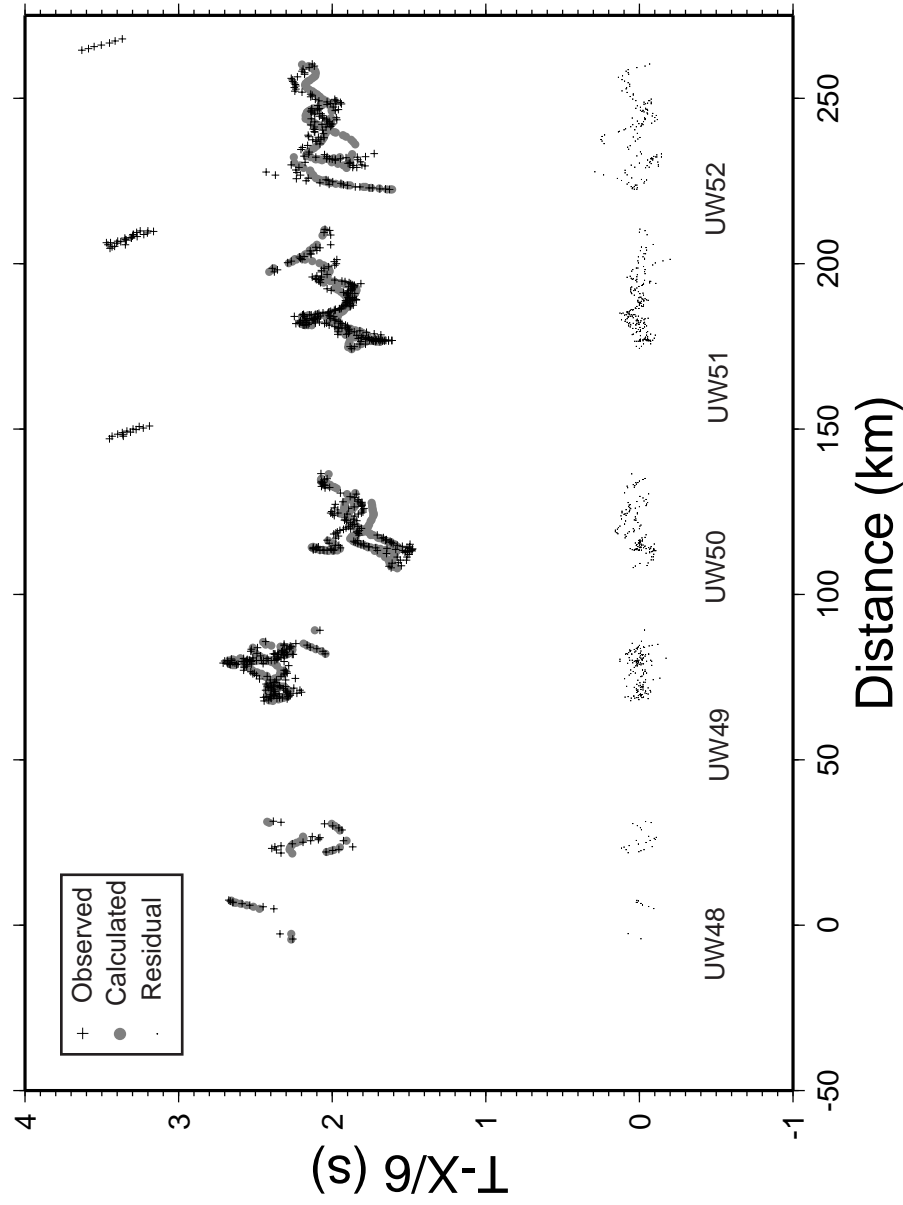


Figure 25: Observed, calculated, and residual travel time plots from stations UW48, UW49, UW50, UW51, and UW52. Offsets of less than 50 km are plotted. Observed picks are denoted as the black plus signs, calculated are the gray circles, and residuals are the black points.

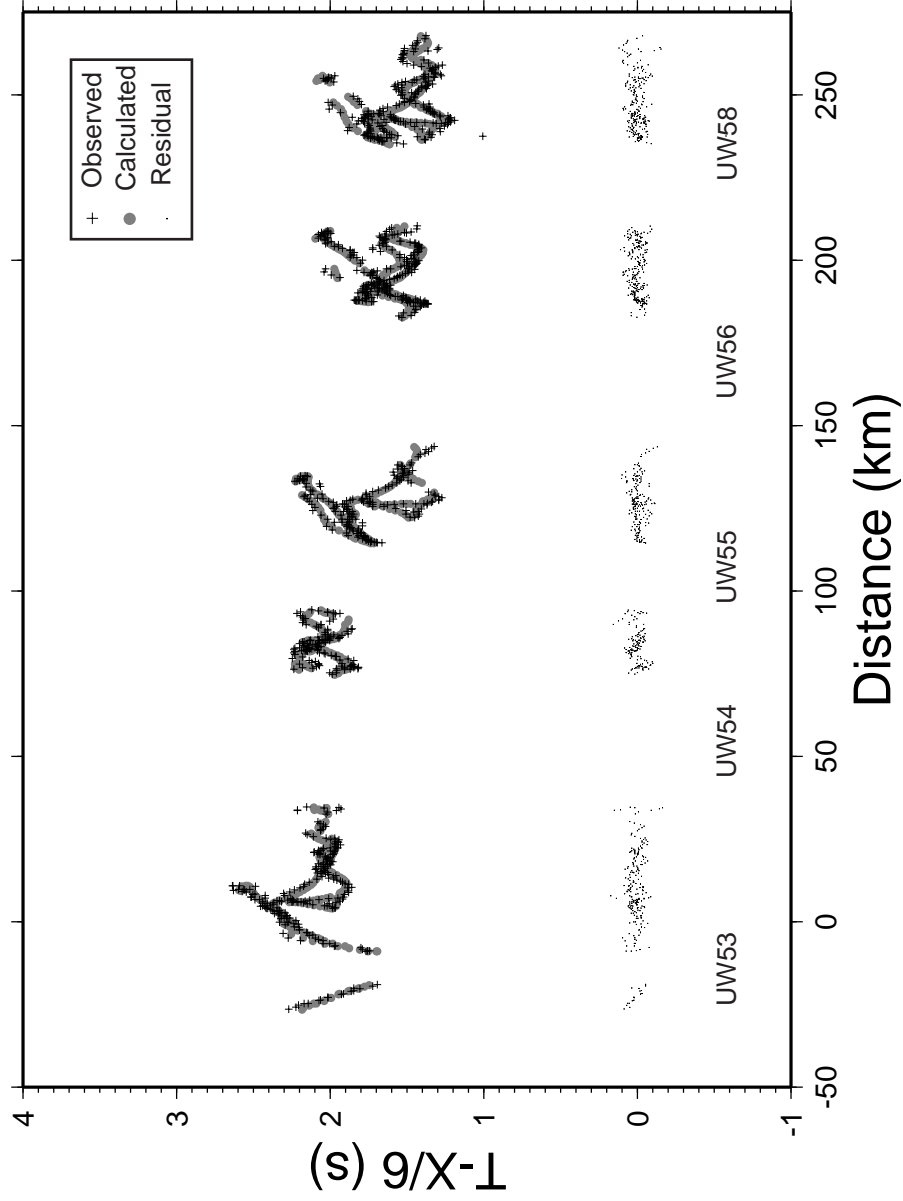


Figure 26: Observed, calculated, and residual travel time plots from stations UW53, UW54, UW55, UW56, and UW58. Offsets of less than 50 km are plotted. Observed picks are denoted as the black plus signs, calculated are the gray circles, and residuals are the black points.

Resolution

To avoid over- or under-interpretation of the tomography results, it is important to understand the spatial resolution of the velocity variations in the final model. Two measures of resolution are ray coverage and checkerboard tests. Ray coverage is a measure of how many rays constrain the velocity estimate for a given cell. The more rays in a cell, the more reliable the velocity is for that cell. Checkerboard tests are a measure of how well the ray coverage can recover a known alternating velocity pattern and thus provide a measure of what size structure the velocity model is resolving.

Checkerboard Tests

For this project, checkerboard tests were conducted as follows: (1) the final velocity model output from the tomography was smoothed to a 1-D velocity model, (2) in map view, sinusoidal checkers, with amplitudes of $\pm 5\%$ of the velocity in a layer were added to this smoothed velocity model. Checkers with dimensions of 5x5, 10x10, and 15x15 km were used. Checkers used to determine the resolution at depth were 15x3 km in the X-Z plane. Travel times for the source and receiver geometry used in the experiment were then calculated for the checkerboard model. These travel times were then input as the observed data to an inversion that has a 1-D smoothed version of the final model as the starting model. Five iterations are run with the new picks and velocity model with the intention of reproducing these checkers. The fifth iteration for each checker

dimension is used in all checkerboard figures. A smoother of 2x2x1 was used for all iterations resulting in RMS errors of ~20 ms or less for all checker sizes.

Results of these checkerboard tests in map slices show that the 15-km checkers are the best resolved (Figures 29-30), and at 10-km, checkers begin to smear (Figures 27-28). The checkers are resolved the best at 3 km depth for both 10 and 15 km. Smearing becomes worse with depth (Figures 27 and 29). The 5x5 km checker model were smeared at all depths suggesting poor resolution at this spatial dimension. The best resolved checkers appear in the Tacoma Basin area. Both the 10x10 and 15x15 km models show relatively good checker reproduction at the 3-km depth slice for the Tacoma Basin.

Checkers with dimensions of 15x3 km were chosen for X-Z tests, since the best spatial resolution from the map slices occurred for the 15x15 km checkers. Since previous studies have shown that the Tacoma Basin is probably about 3.5 km deep, 3 km seemed to be a reasonable size for the checker in the Z direction. The results of these tests followed the pattern of the 10x10 and 15x15 km checkers. Checkers are better resolved at shallower depths (3-4 km) and become more poorly resolved as depth increases (Figures 31 and 32). Overall the resolution tests suggest that the velocity model will reliably resolve structures greater than 10 km in the X-Y dimension and greater than 3 km in the Z direction.

Ray Coverage

For the Tacoma basin, ray coverage is excellent. Within 2 km of a suggested 5.5 km/s Tacoma Basin/Crescent Formation contact, ray density is

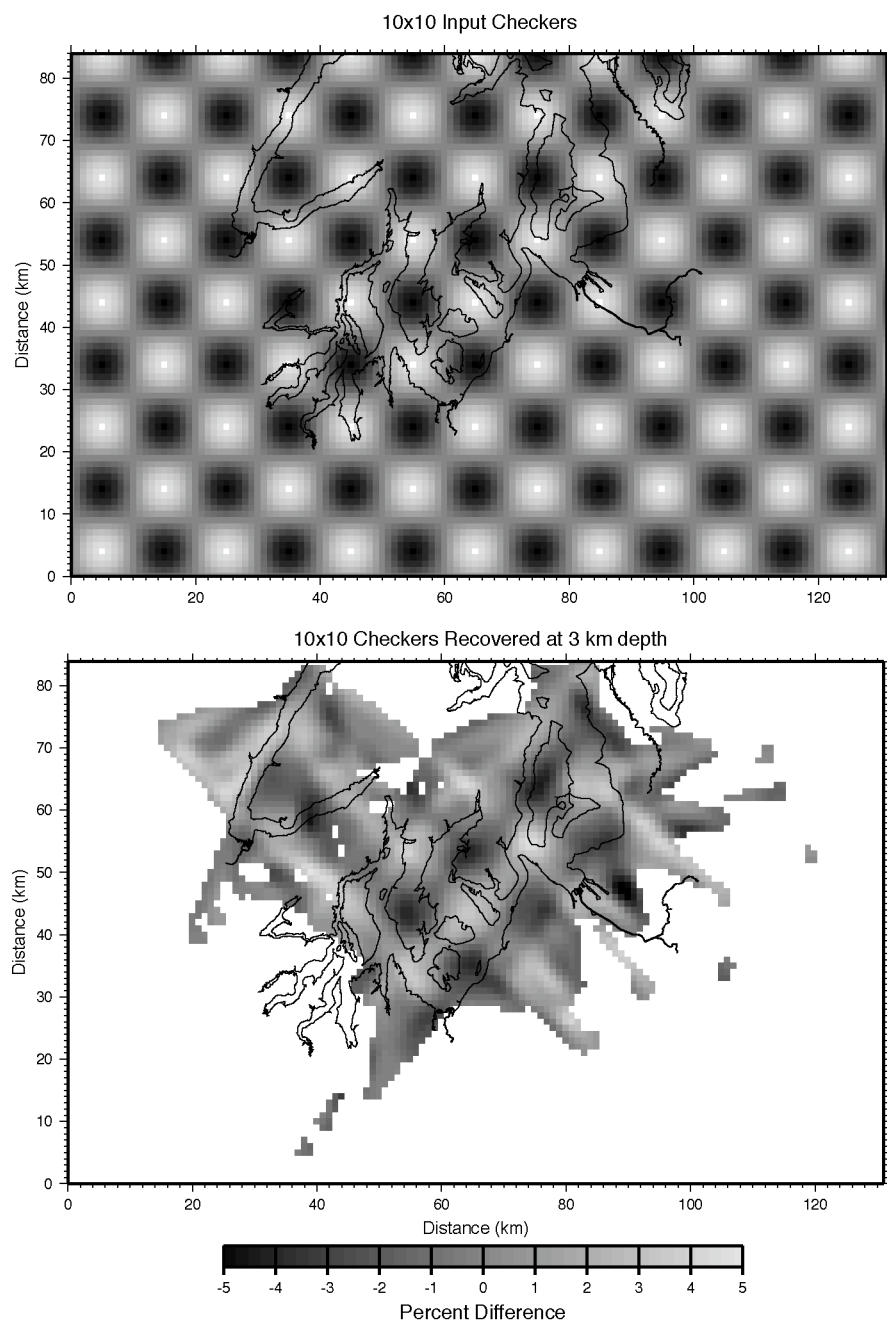


Figure 27: 10x10 km input checkerboard and recovered checkers at 3 km depth. Waterways in Puget Lowland are overlain for reference.

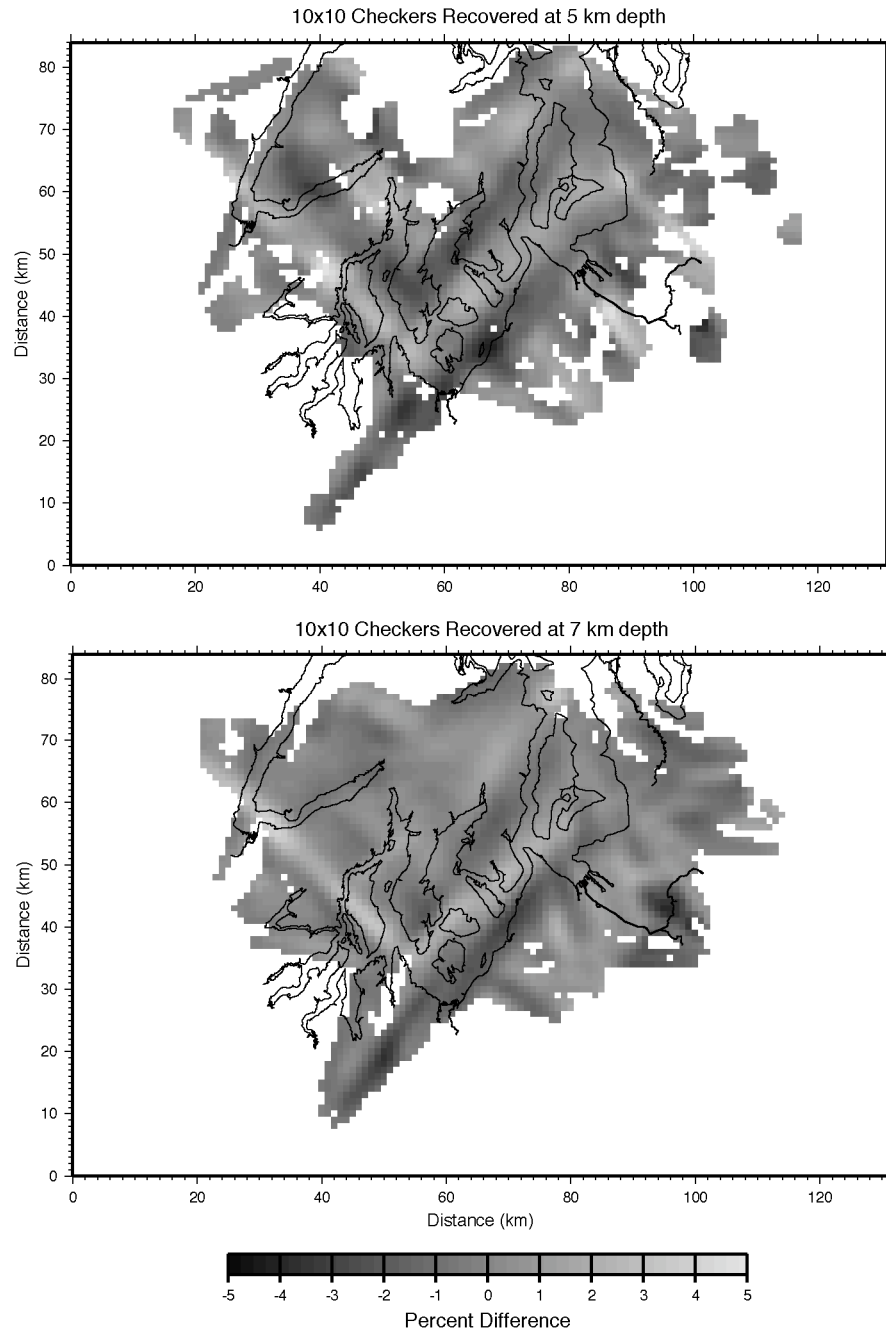


Figure 28 : 10x10 checkers recovered at 5 and 7 km depth. Waterways in the Puget Lowland are overlain for reference.

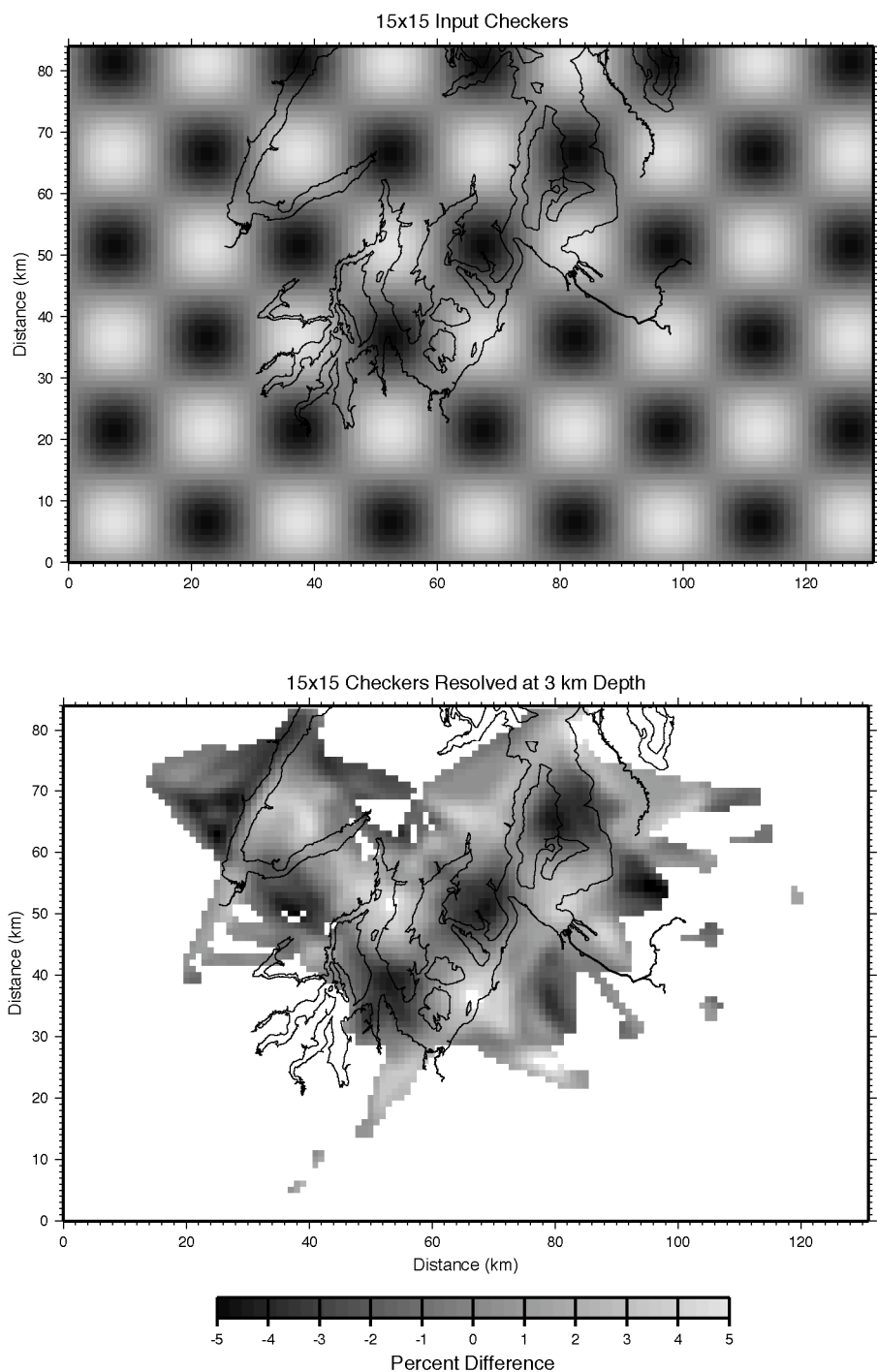


Figure 29: 15x15 input checker model and checkers recovered at 3 km depth. Waterways in the Puget Lowland are overlain for reference.

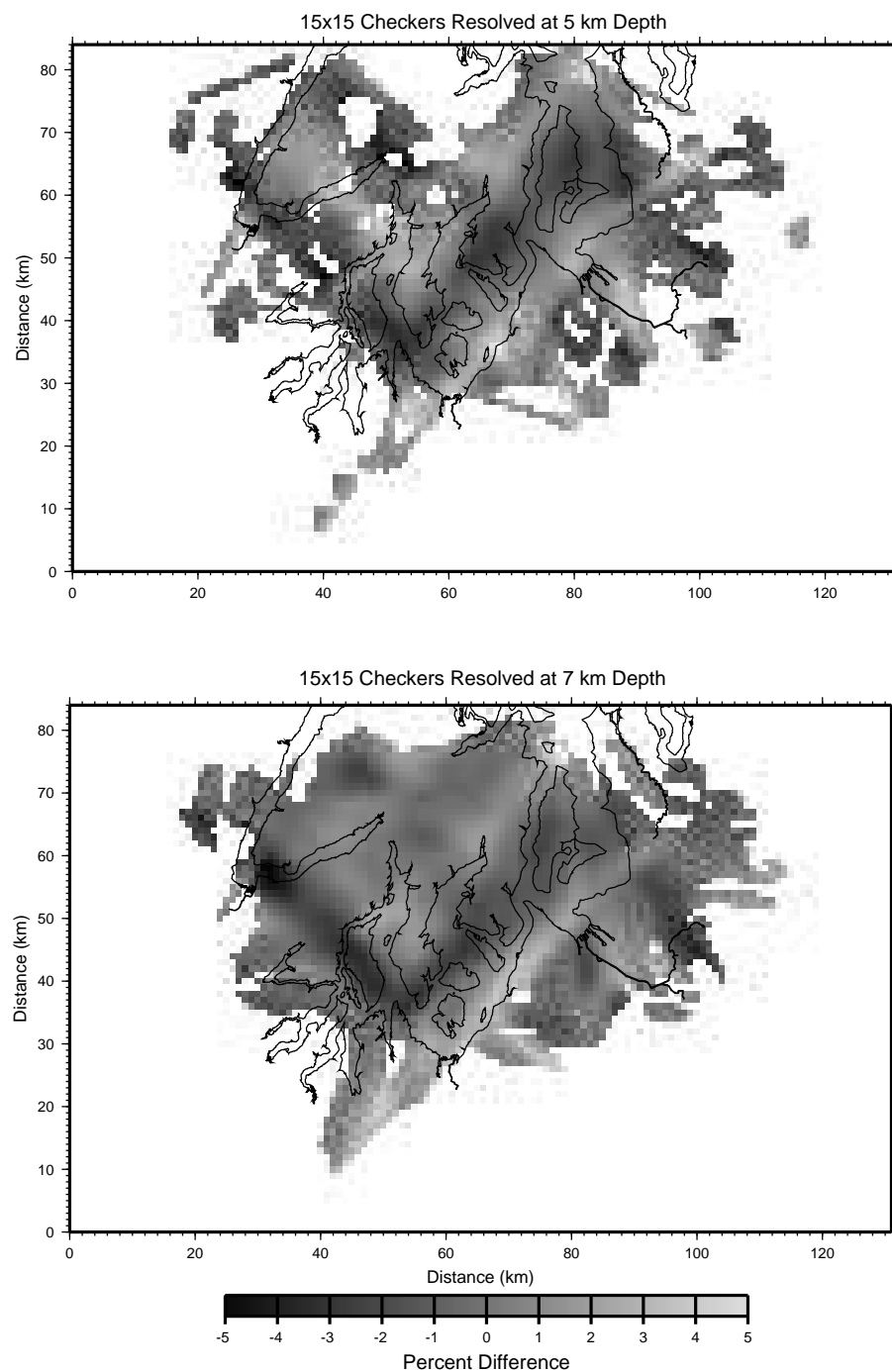


Figure 30: 15x15 checkers recovered at 5 and 7 km depth. Waterways are overlain for reference.

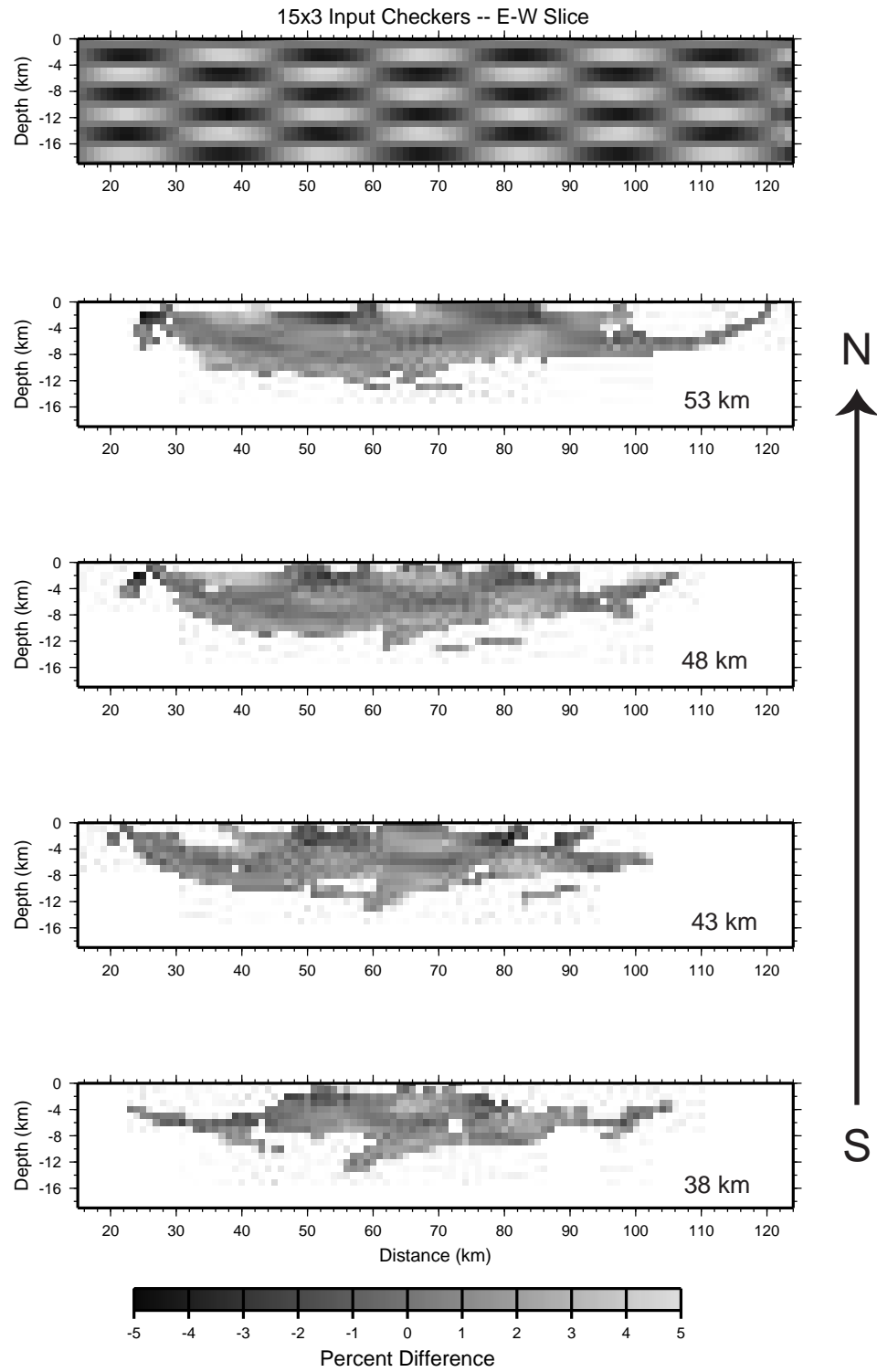


Figure 31: 15x3 checkers starting model and recovered checkers from E-W slices at 38 to 53 km.

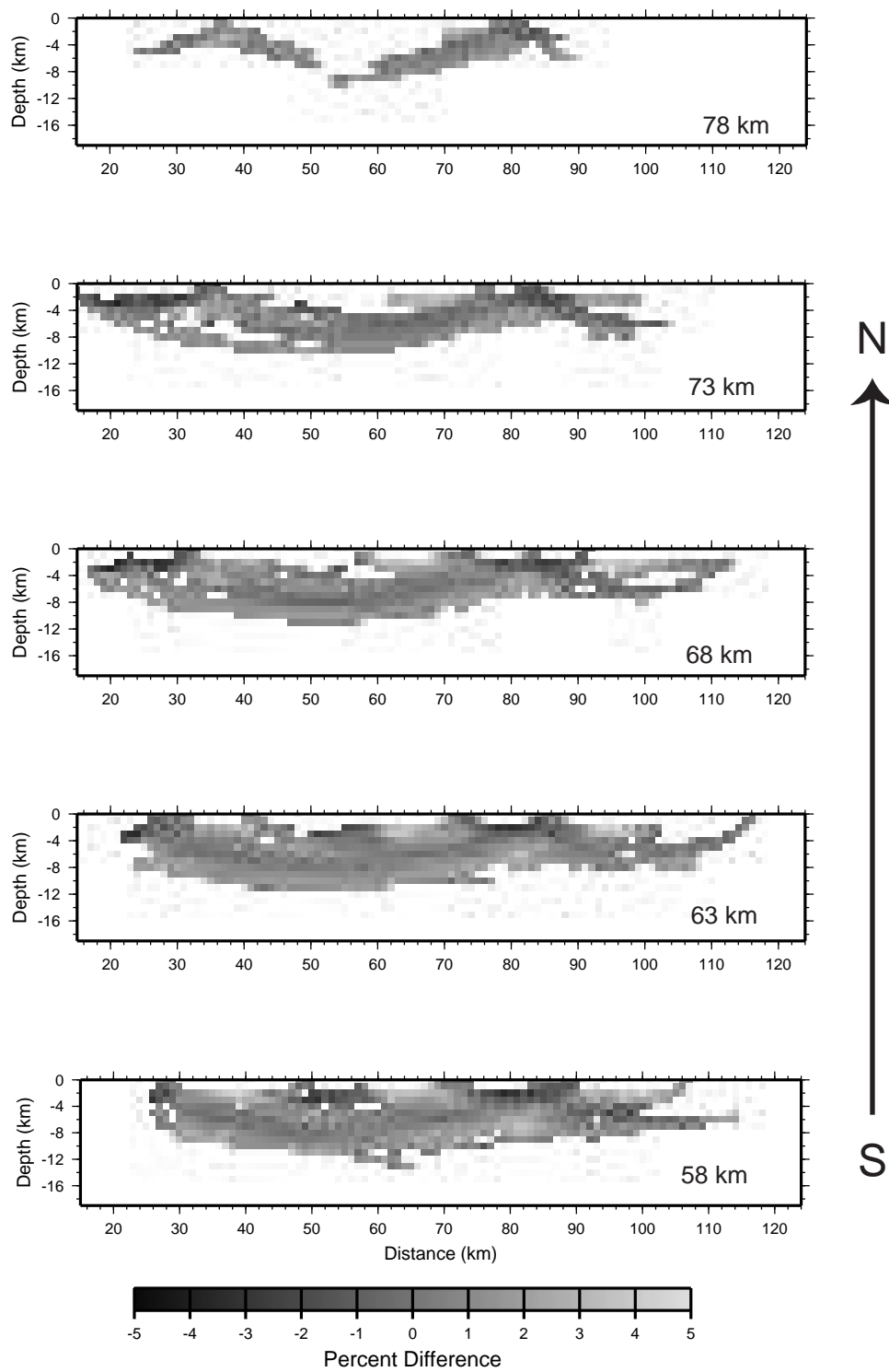


Figure 32: 15x3 checkers recovered from E-W slices at 58 to 78 km.

high, indicating that any grid plotted with a velocity was penetrated by a ray and is reliable. Ray densities reach as much as 4000 rays/cell. Those grids that are not penetrated by rays are not plotted.

Ray coverage is very good at shallower depths when close to shots and receivers. Figures 33-35 show the ray coverage for 3 depth slices. The best ray coverage occurs in the waterways where the boat was tracking through while good ray coverage is found in between the waterways on land where the stations are surrounded by airgun shots. Poorer ray coverage occurs to the extreme west, south, and east of the study area where incident rays come from only one azimuth.

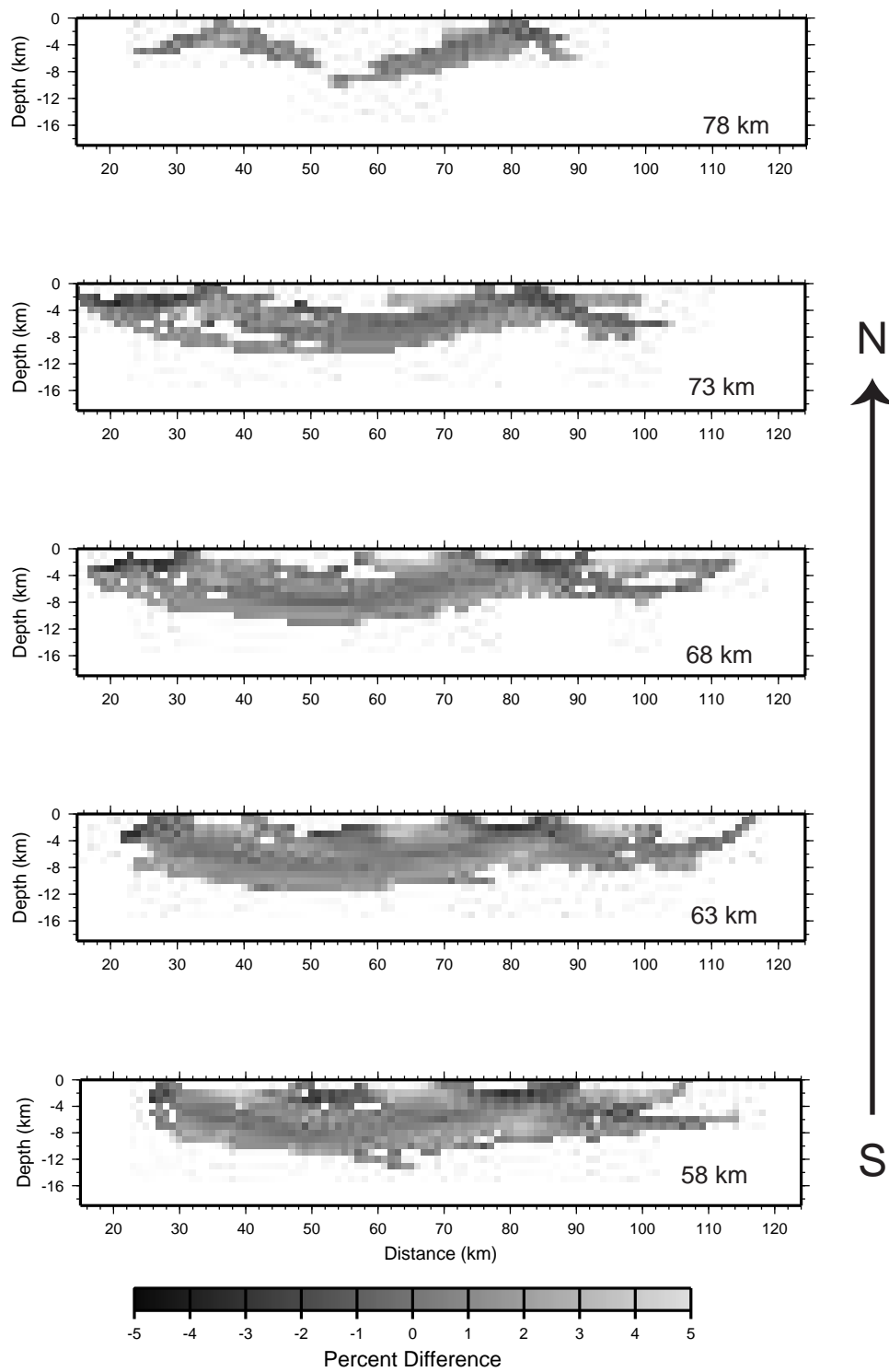


Figure 33: 15x3 checkers recovered from E-W slices at 58 to 78 km.

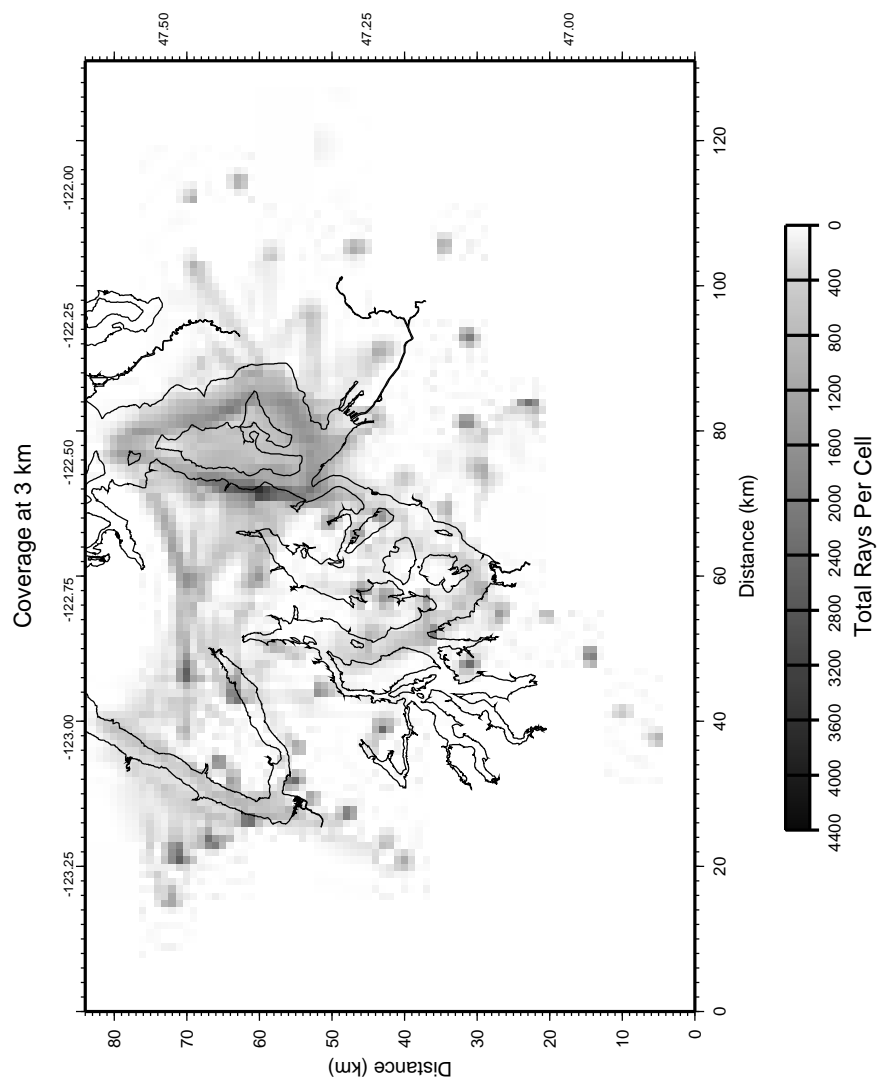


Figure 33: Ray coverage at 3 km depth. The higher the ray count per cell, the more reliable the velocity in that cell.

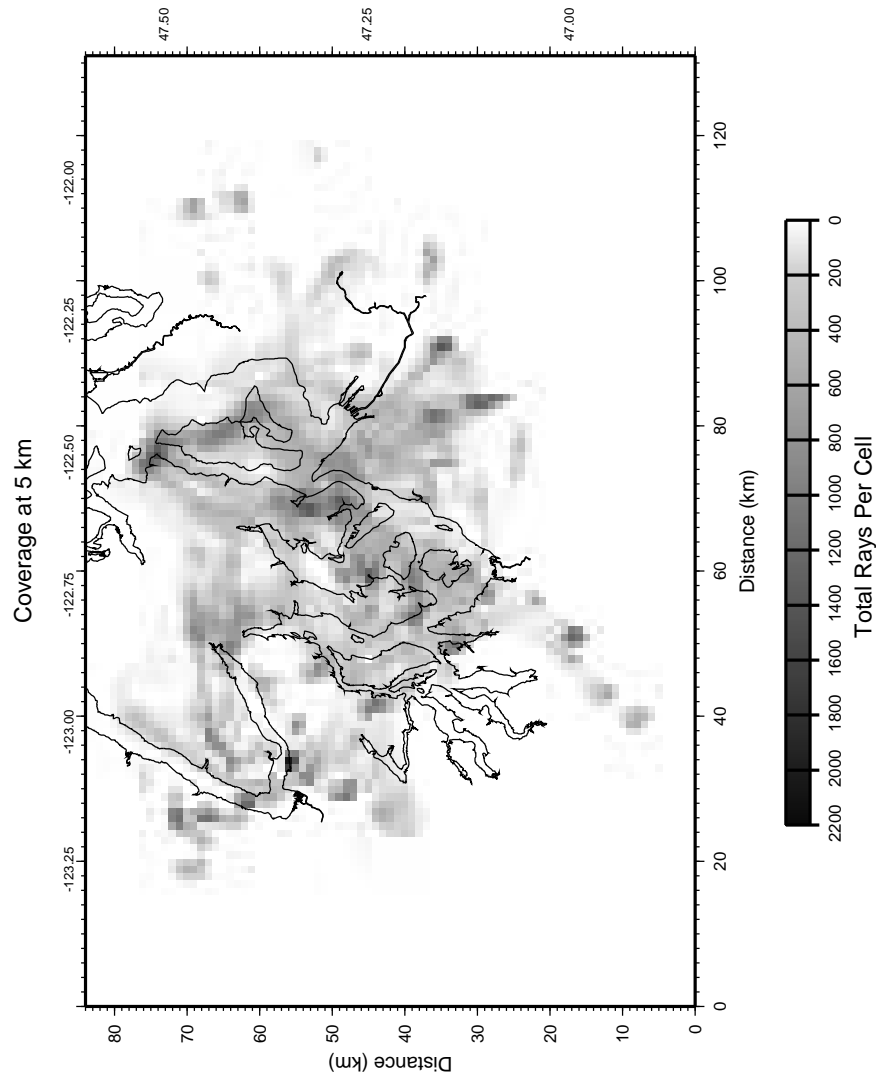


Figure 34: Ray coverage at 5 km depth. The higher the ray count per cell, the more reliable the velocity in that cell.

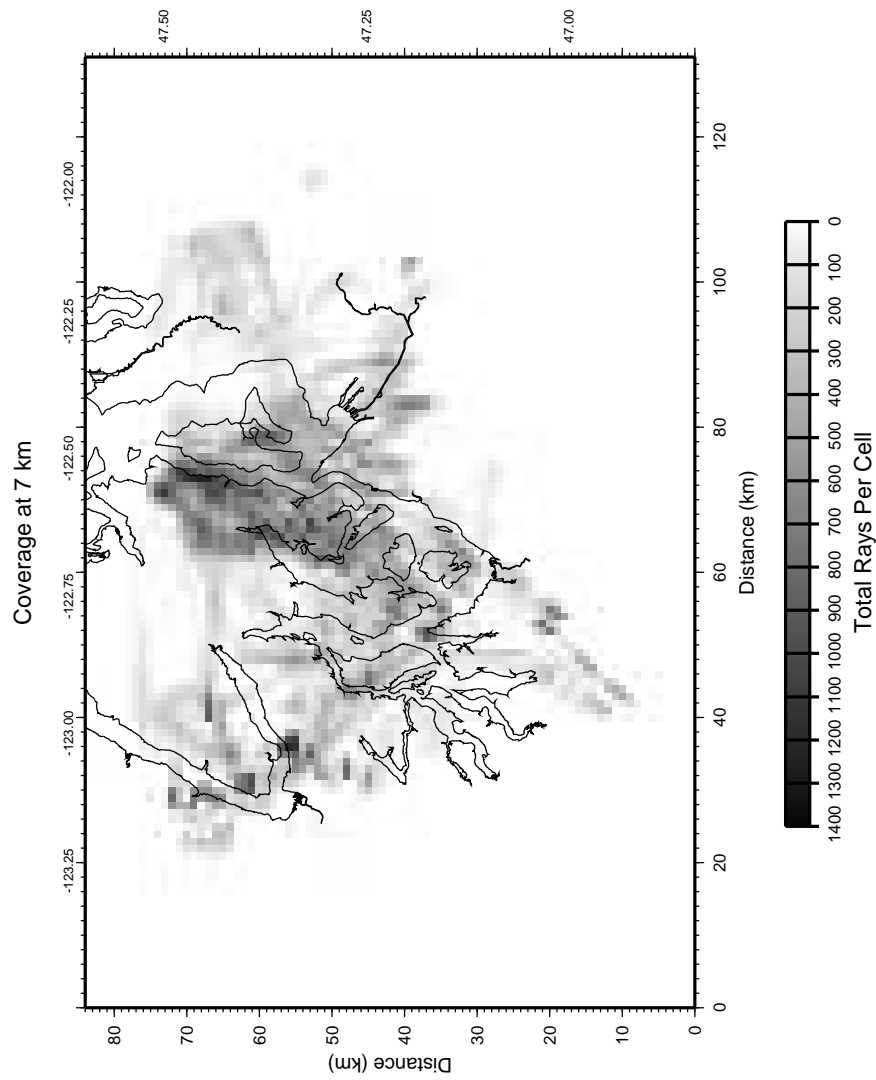


Figure 35: Coverage at 7 km depth. The higher the ray count per cell, the more reliable the velocity in that cell.

Tomography Results

The best way to view the main features resolved by the model is with depth slices and cross-sectional slices through the velocity model. Rock type and velocity should correlate and are important to model interpretation.

Sediment velocities are expected to be in the range of 2-4 km/s while Crescent Formation basalt velocities should be around 5-6 km/s. Velocities of 5.0 km/s (Parsons et al., 1999) and 5.5 km/s (Brocher et al., in review) have been used as a proxy for the top of the Crescent Formation and could be a good indicator of basin boundaries. The main features to examine are the Tacoma basin, the southern edge of the Seattle basin, Seattle uplift, the base of the Olympic uplift, the base of the Black Hills uplift, the Tacoma Narrows fault, and the Seattle Fault.

Map Slices (figures 36-39)

The map slice at 1-km (Figure 36) shows little more than approximate station locations and shot locations in the waterways. Coverage here is sparse and little can be identified, although velocities do appear to be slower in the southern part of Puget Sound and faster to the north.

The map slice at 3-km (Figure 37) depth contains much better ray coverage than the 1-km depth slice. The area in the center of the model space characterized by velocities ~ 4.0 km/s is the Tacoma Basin. Northwest of the main basin area ($x=38$ km, $y=65$ km) is a smaller subbasin with comparable

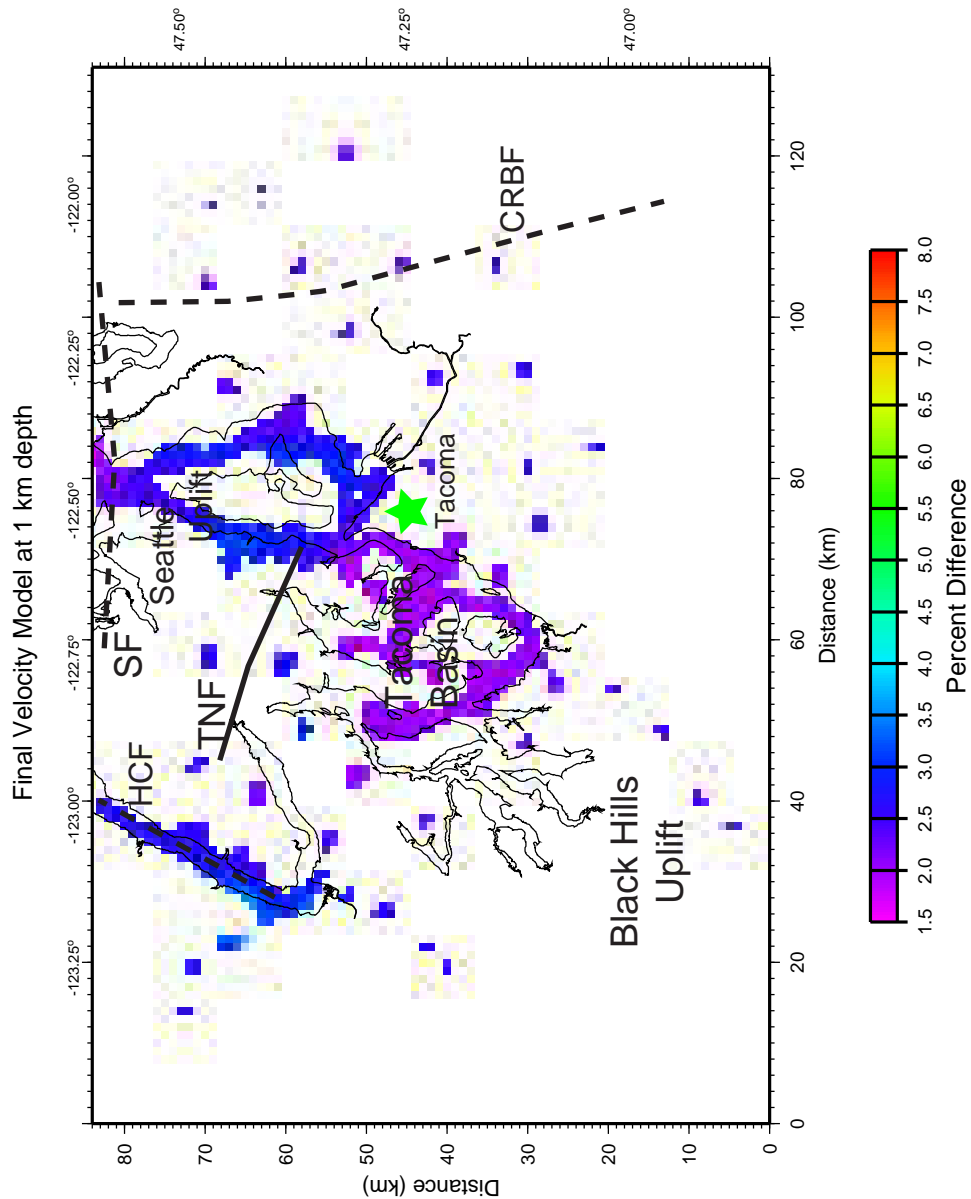


Figure 36: Velocity slice at 3 km depth masked with ray coverage. Waterways in the Puget Lowland are overlain for reference. TNF=Tacoma Narrows Fault; SF=Seattle Fault;HCF=Hood Canal Fault; CRBF=Coast Range Boundary Fault.

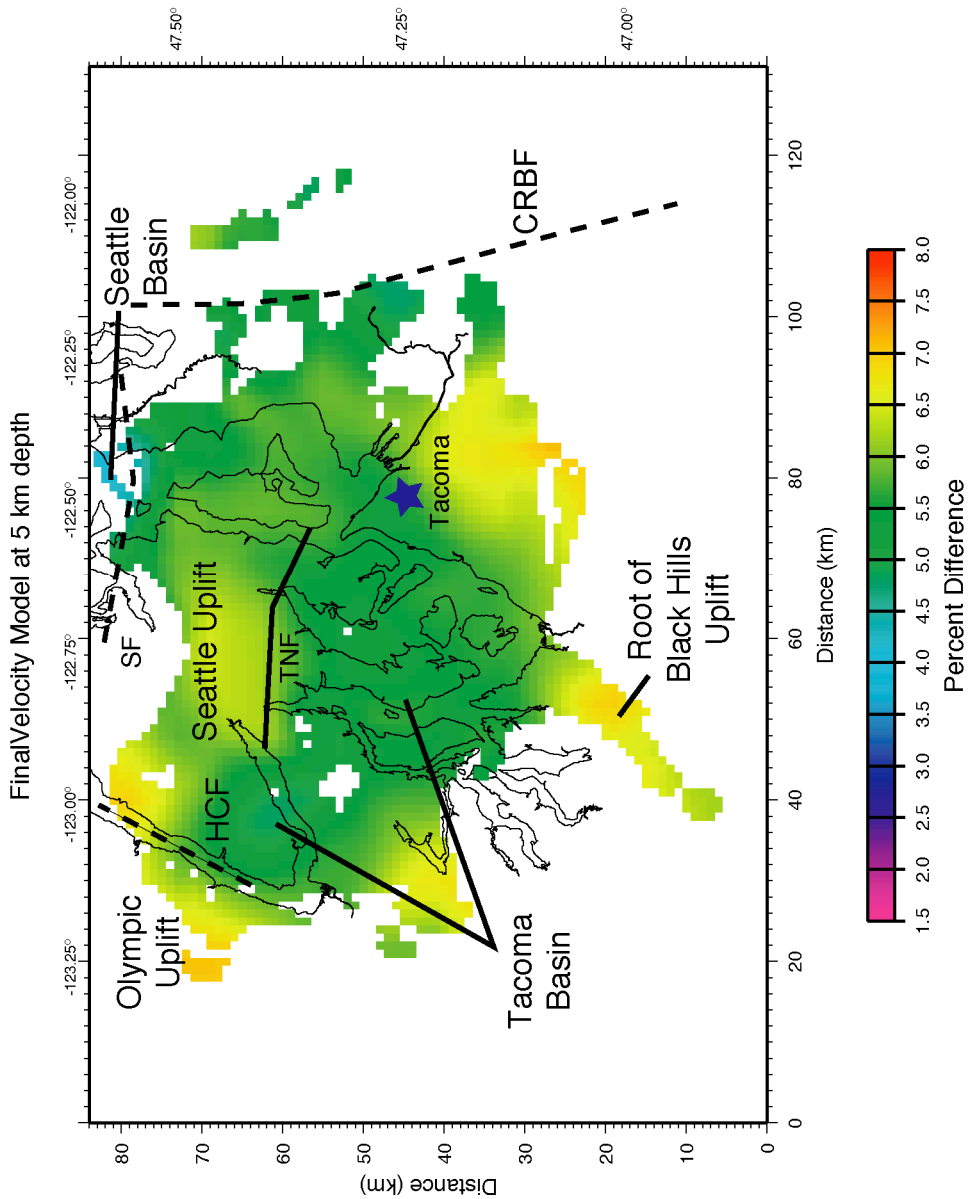


Figure 38: Velocity slice at 5 km depth masked with ray coverage. Waterways in the Puget Lowland are overlain for reference. TNF=Tacoma Narrows Fault; SF=Seattle Fault; HCF=Hood Canal Fault; CRBF=Coast Range Boundary Fault.

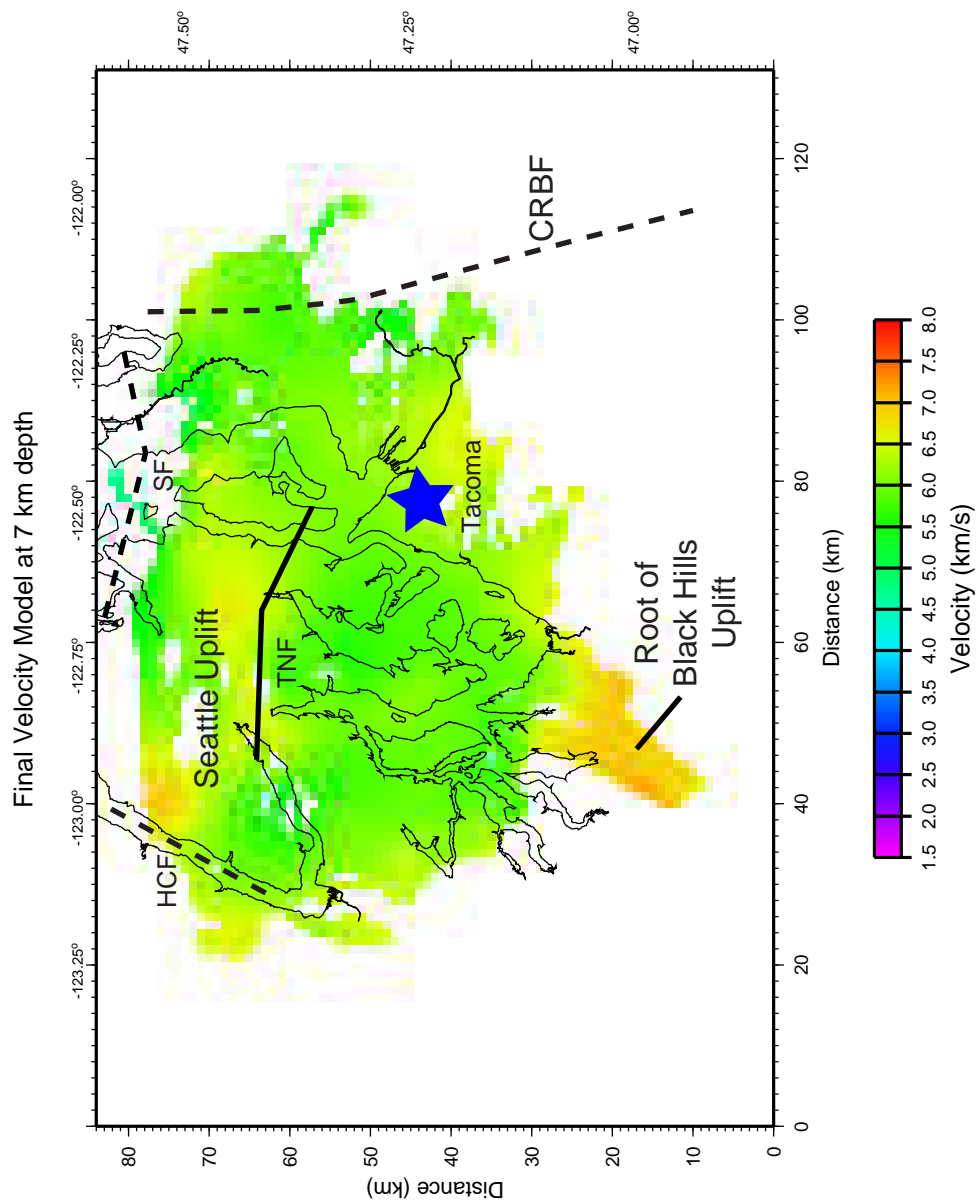


Figure 39: Velocity Slice at 7 km depth masked with ray coverage. Waterways in the Puget Lowland are overlain for reference. TNF=Tacoma Narrows Fault; SF=Seattle Fault; HCF=Hood Canal Fault; CRBF=Coast Range Boundary Fault.

velocities. Farther to the northwest is what appears to be the southwestern edge of the Olympic Uplift. Velocities here approach 8 km/s. This is anomalously high, and probably represents an overestimate due to the lack of reversing ray coverage. One would expect velocities here to be between 6.0 km/s and 6.5 km/s. Just north of the Tacoma Basin is the Seattle Uplift. Velocities here are between 6.0 km/s and 6.5 km/s, exactly what to expect for Crescent Formation basalts. Northeast of the Seattle Uplift is another low velocity zone that is the southern part of the Seattle Basin, which is characterized by velocities between 3 and 4 km/s.

Coverage at 5 km is still good, and major features can still be seen. The main body of the Tacoma Basin is evident, but it is near its deepest point if not already at the Crescent Formation based on velocities around 5.5 km/s. The smaller subbasin to the northwest shows slightly lower velocities (between 4.0 and 4.5 km/s) and may extend deeper than the main body of the Tacoma Basin. The Olympic Uplift still appears to have unusually high velocities, but the Seattle Uplift remains reasonable with velocities ~6.5 km/s. Little of the Seattle Basin is sampled by rays, but the small amount that is shows low velocities in the sediment range (~4.0 km/s) indicating the basin is still present at 5 km depth. Just south of the main body of the Tacoma Basin is a strip of high velocity extending southwest. This may represent the root of the Black Hills Uplift.

The final map slice at 7-km still retains the good coverage seen in previous slices. The Tacoma Basin is no longer evident based on the existing velocities (5.5 km/s and above). Velocities in the strip just south of the Tacoma Basin area still exhibit the probably root of the Black Hills Uplift. Ray coverage in this strip has also improved showing more than previously seen.

West-East Slices (figures 40-41)

Slices taken from west to east give us a better idea of the structures with respect to each other. From the 33 km slice in the south moving north, the root of the Black Hills Uplift can be seen to extend to about 10 km. As the slices trend further north, the Olympic Uplift shows up as faster and shallower towards the west. The Tacoma Basin deepens as the slices trend north from the 33 km slice. Slices 38-53 show the deepest part of the Tacoma Basin, and the slice at 63 km shows the smaller subbasin to the northwest. Slice 78, although the coverage is poor, shows the southern edge of the Seattle Basin around the 80-km point.

North-South Slices (figures 42-44)

The central part of the Tacoma Basin is easily seen from slice 45 to 70. Slice 35 shows the northwest subbasin. Low velocities of the Seattle Basin can be seen on slices 80 and 85 between 2 and 10 km. Evidence for the Tacoma Narrows Fault can be seen on slices 55 through 70 around the 25-km point. Velocities here suggest this fault dips to the north. Also, velocities on the north side of this structure illustrate the Seattle Uplift on slices 50 through 70.

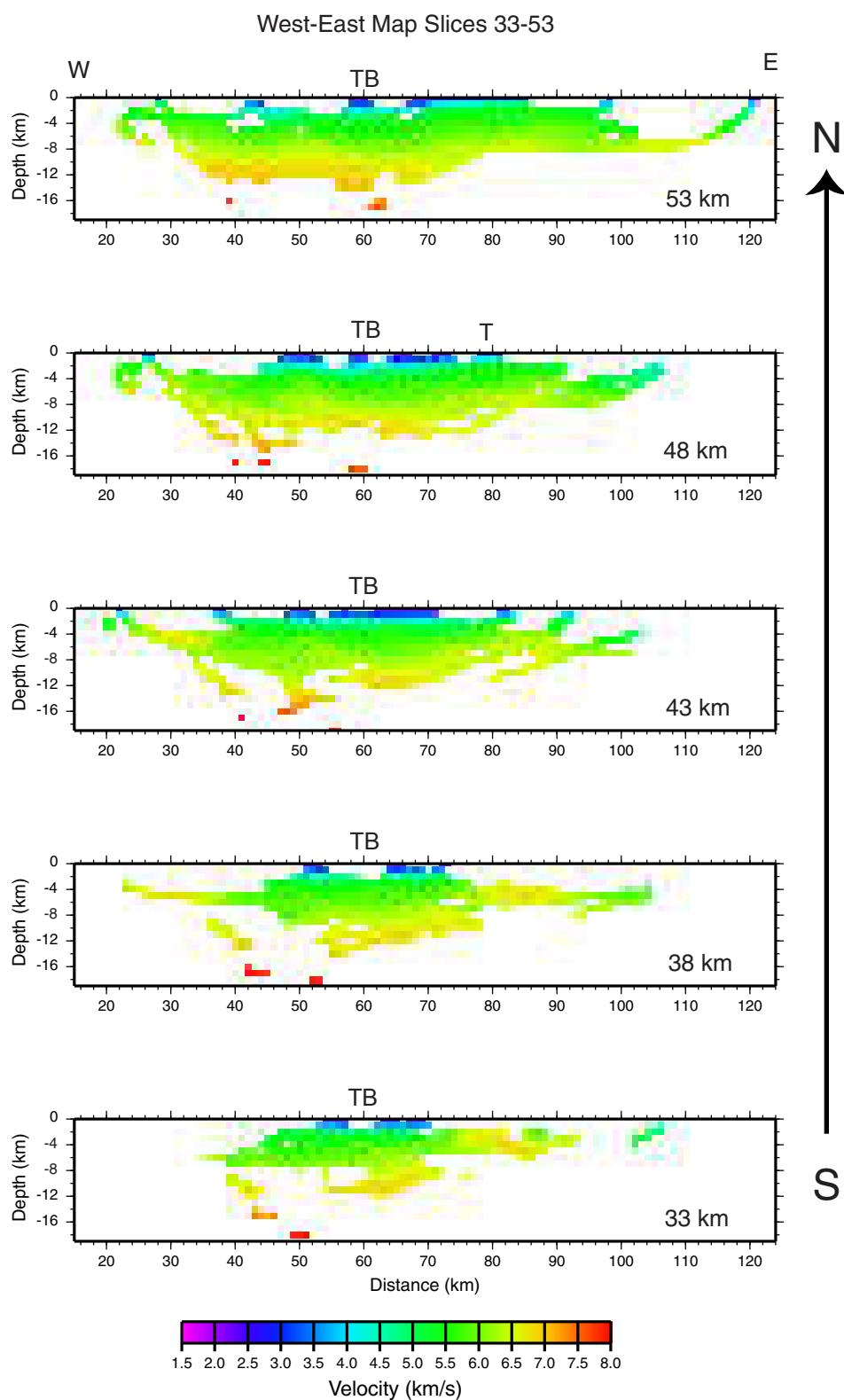


Figure 40: West-East velocity slices from 38 km to 53 km.
TB=Tacoma Basin; T=Tacoma.

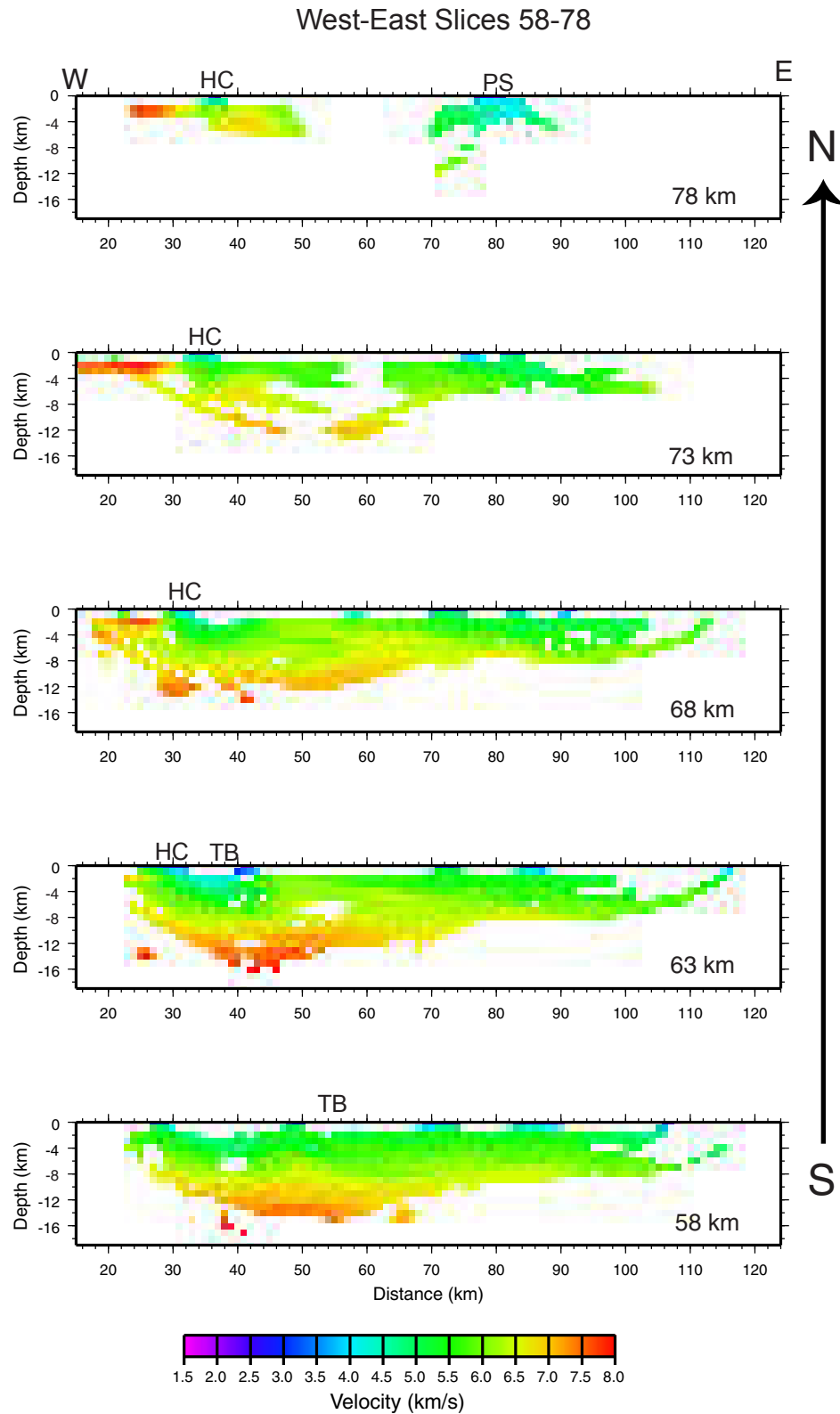


Figure 41: West-East velocity slices from 58 km to 78 km.
 HC=Hood Canal; PS=Puget Sound; TB=Tacoma Basin.

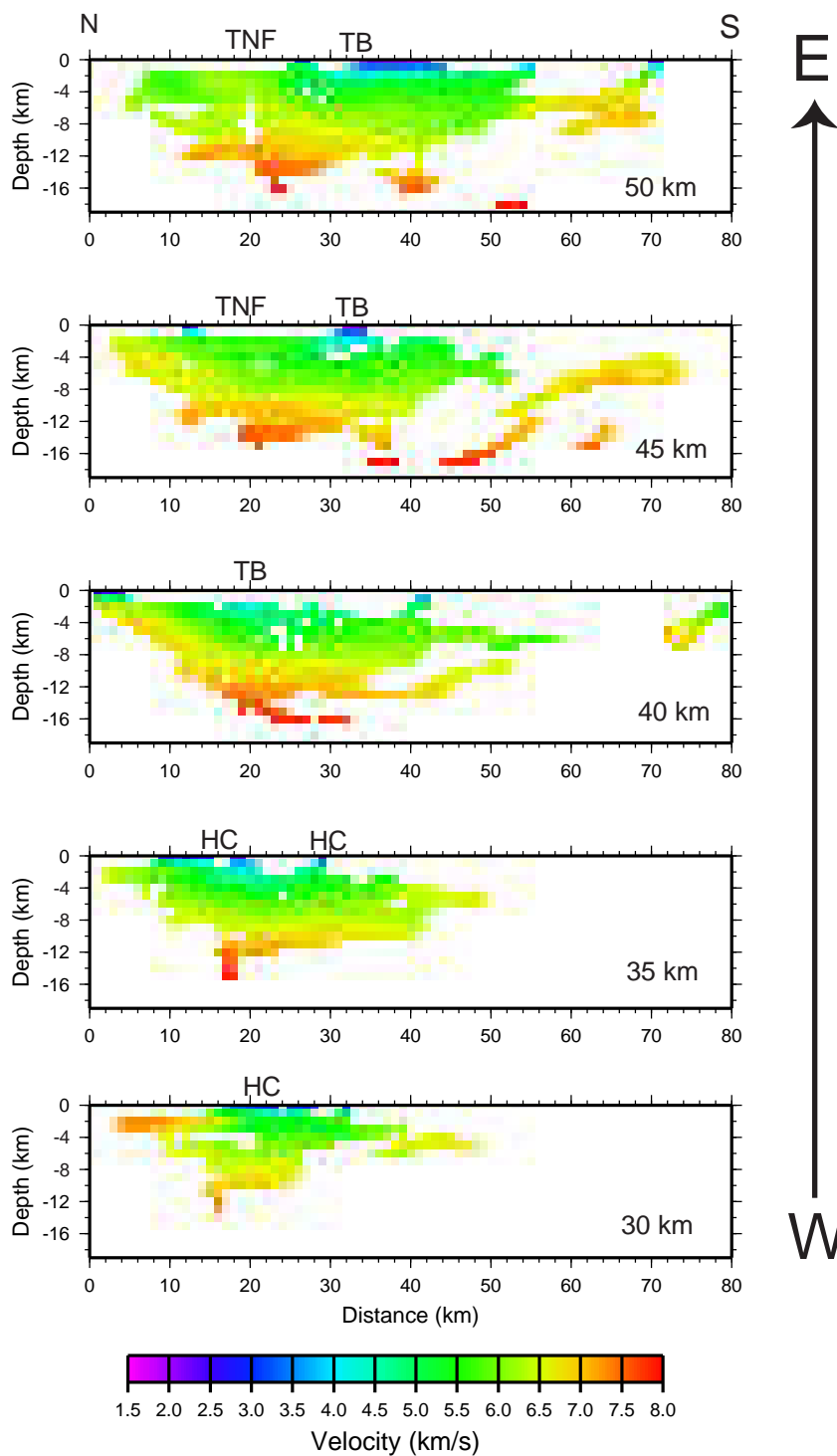


Figure 42: North-south slices from 30 km to 50 km. HC=Hood Canal; TB=Tacoma Basin; TNF=Tacoma Narrows Fault.

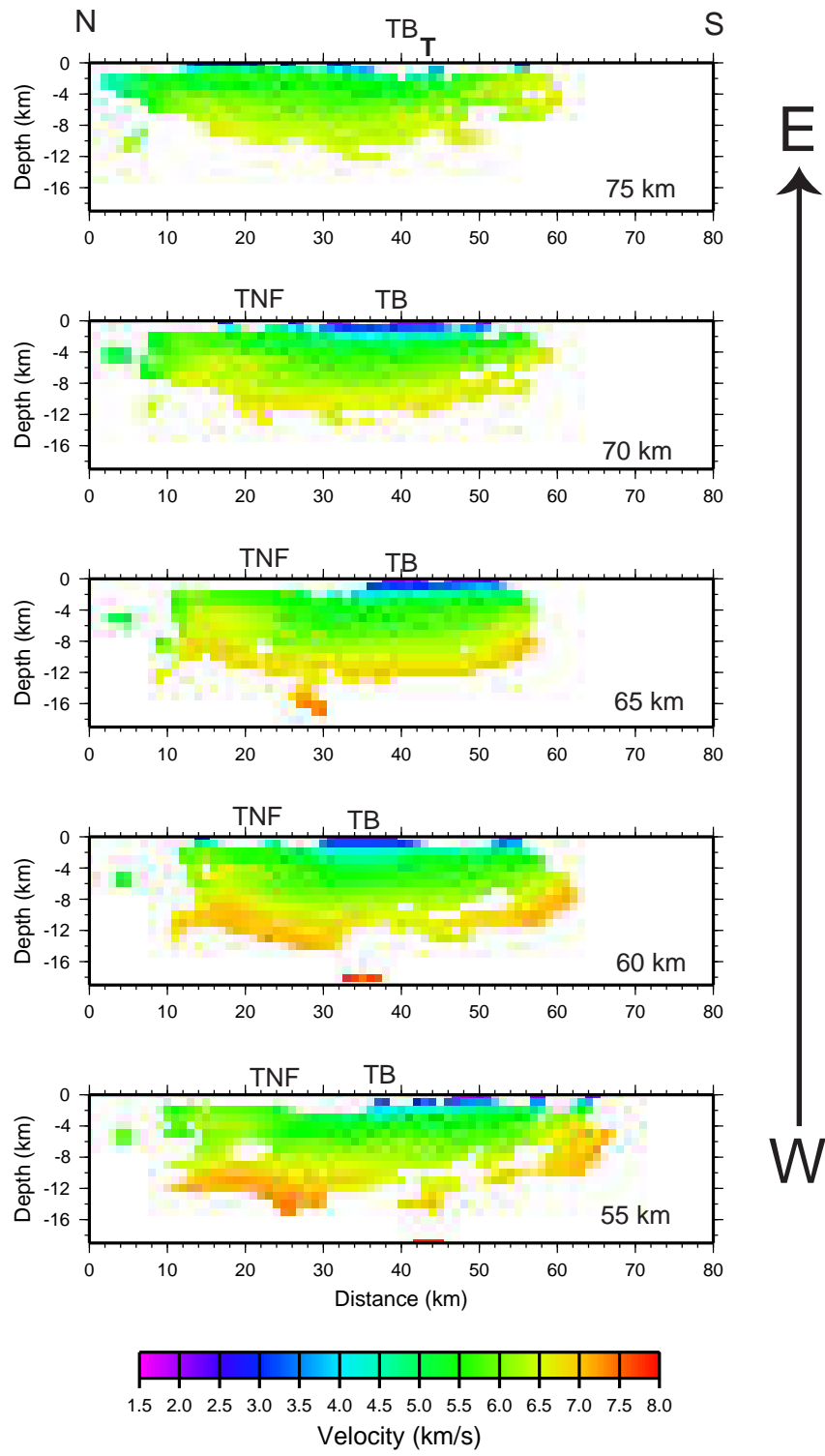


Figure 43: North-south velocity slices from 55 km to 75 km. TB=Tacoma Basin; T=Tacoma.

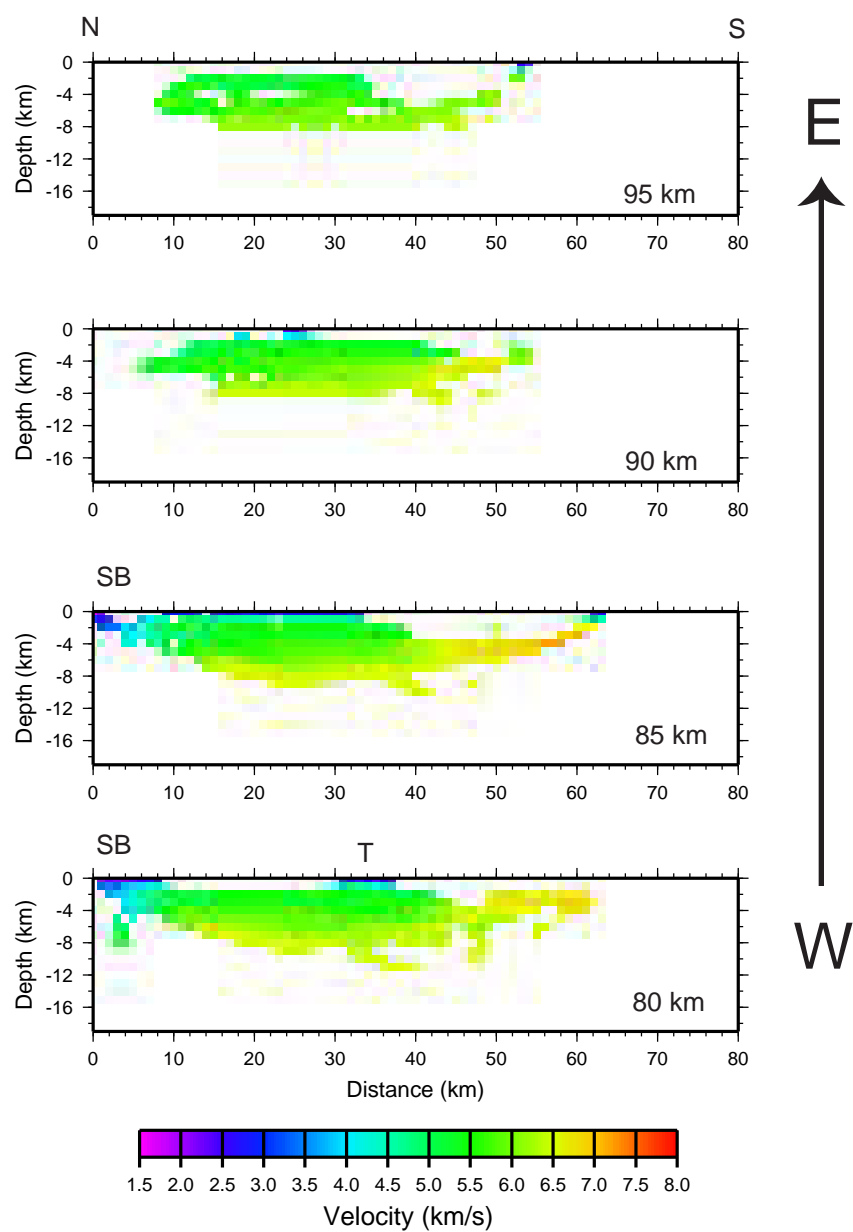


Figure 44: North-south velocity slices from 80 km to 95 km. SB=Seattle Basin; T=Tacoma.

Wide-Angle Reflection Methodology

Because of the large cells in the tomography (1 km^3), the result produces a velocity model that is smooth compared to the geology that is imaged. For example, it might be expected that the contact between Tacoma basin sediments ($< 4 \text{ km/s}$) and Crescent Formation ($> 5.5 \text{ km/s}$) would be a rapid change (e.g. 10s of meters). However, this change is represented by a gradient over a 2 to 3 cell range in the tomography (Figures 40-44). One approach to help locate the basin/basement interface is to model the reflected phase from the bottom of the basin in conjunction with velocities from the tomography.

To estimate reflection travel times for the base of the Tacoma basin the method of Hole and Zelt (1995) was used. The best velocity model from the tomography and an estimate of the depth to the reflector is used as input parameters. A final travel time field based on the reflector is computed and used to calculate travel times for stations and receivers in the model space.

From the final tomography model a major reflector, in this case the Crescent Formation basalts, can be chosen based on the velocities. Brocher et al. (in review) chose a velocity contour of 5.5 km/s as the top of the Crescent Formation using the same tomography program in the same area. That velocity contour was also used for the top of Crescent Formation reflector (Figure 45).

The calculated reflection picks to the 5.5 km/s contour were overlain on selected seismic sections. Stations C3008, C3011, C3014, D4010, and D4011 were used because of their potential of recording reflections at near vertical

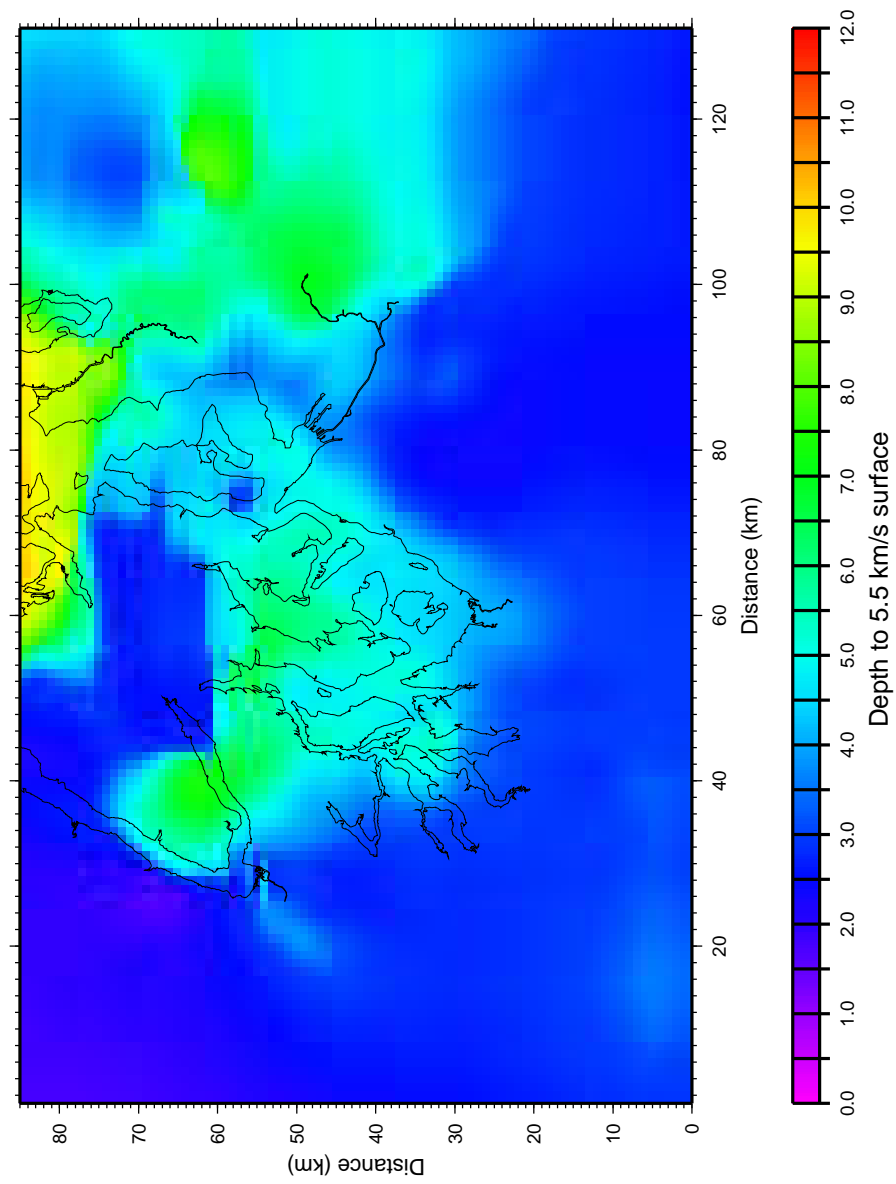


Figure 45: Map of the depth to the 5.5 km/s velocity contour from the tomography. This was used in the calculation of reflection travel times.

incidence (Figures 46-50). These stations are some that best represent the approach and retreat of the shots while other stations are too far away at the closest offset and reflections become asymptotic with the first arrival. All five of these stations exhibit the asymptotic nature of the reflection as the shot-receiver offsets become larger. The reflected calculations at far offsets can easily be seen to overlay the first arrivals. For example, station C3008 becomes asymptotic beyond 6 km offset to the south (Figure 46), and station D4010 becomes asymptotic around 9 km offset to the north (Figure 49). As the offsets become smaller, the late arriving reflection can be seen at all stations. A closer look shows that calculated reflection times do not follow a clear arrival in the data in part because water bottom multiples are too intense to see any reflected energy.

Deconvolution does little to enhance the visibility of reflected arrivals at near vertical incidence. For example, stations C3011 and C3014 (Figure 51 and 52) show what may be reflectors that arrive earlier than that calculated for the 5.5 km/s surface, but the deconvolution of station D4010 (Figure 53) brings out no reflectors with a moveout appropriate for the top of the Crescent Formation. If these reflections are from the top of the Crescent, then they suggest that the 5.5 km/s contour is too high a velocity for a top of Crescent Formation estimate and that 5.0 or 4.5 km/s may be a better choice.

Station C3008 --- Shot Line 9

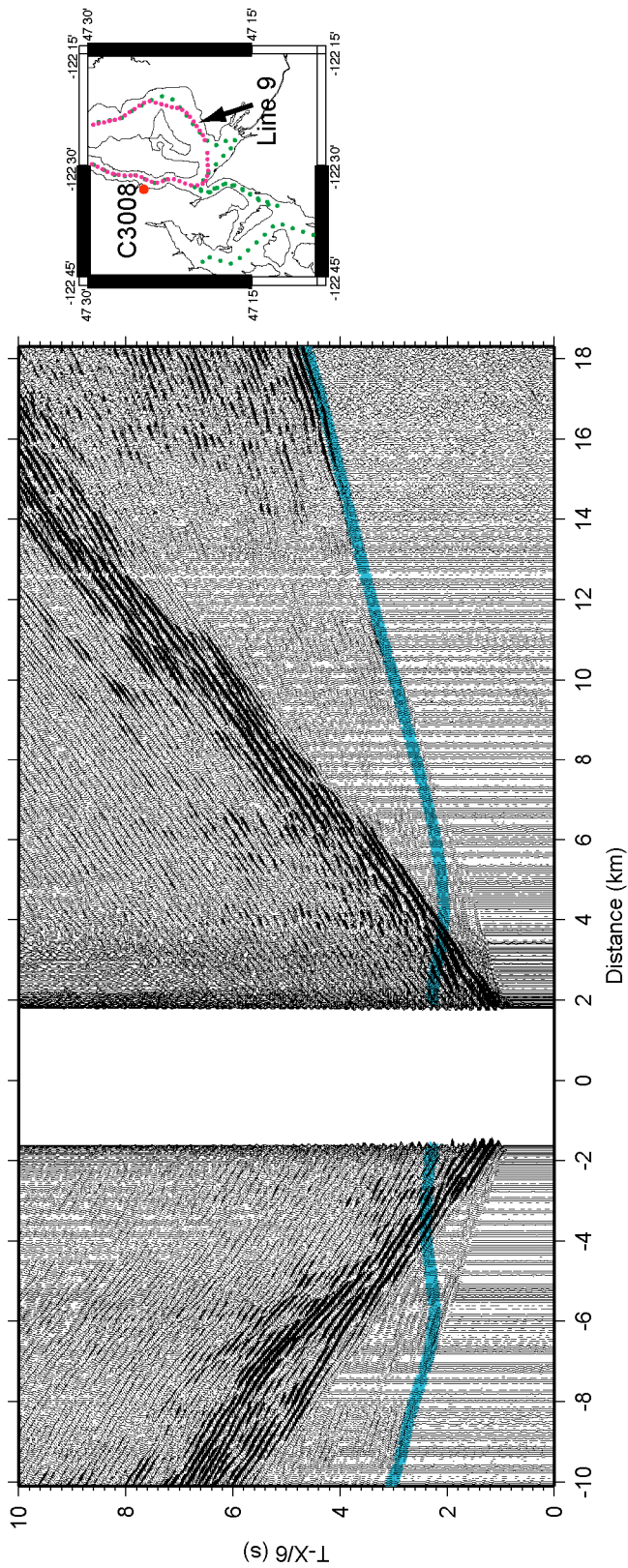


Figure 46: Shots from line 9 recorded at station C3008 with reflection travel time calculations overlain.

Station C3011 -- Shot Line 2

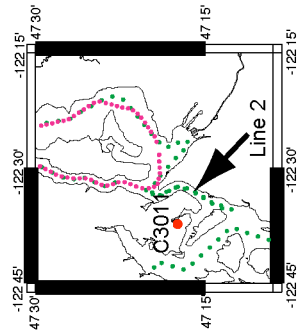
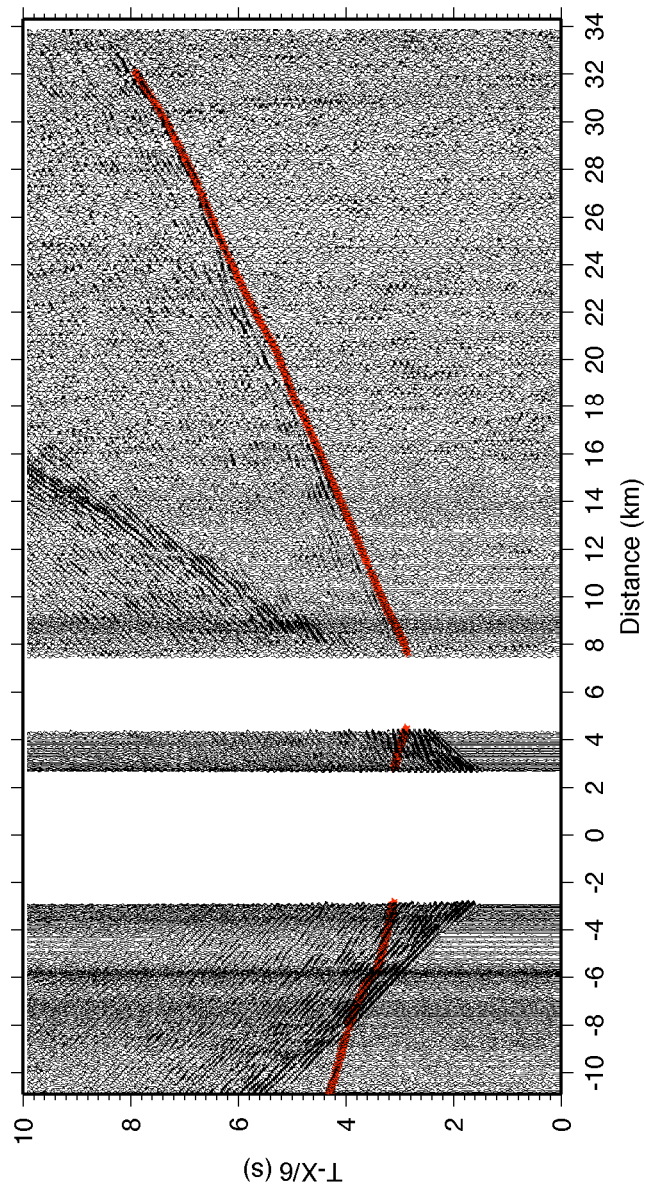


Figure 47: Shots from line 2 recorded at station C3011 with reflection travel time calculations overlain.

Station C3014 -- Shot Line 2

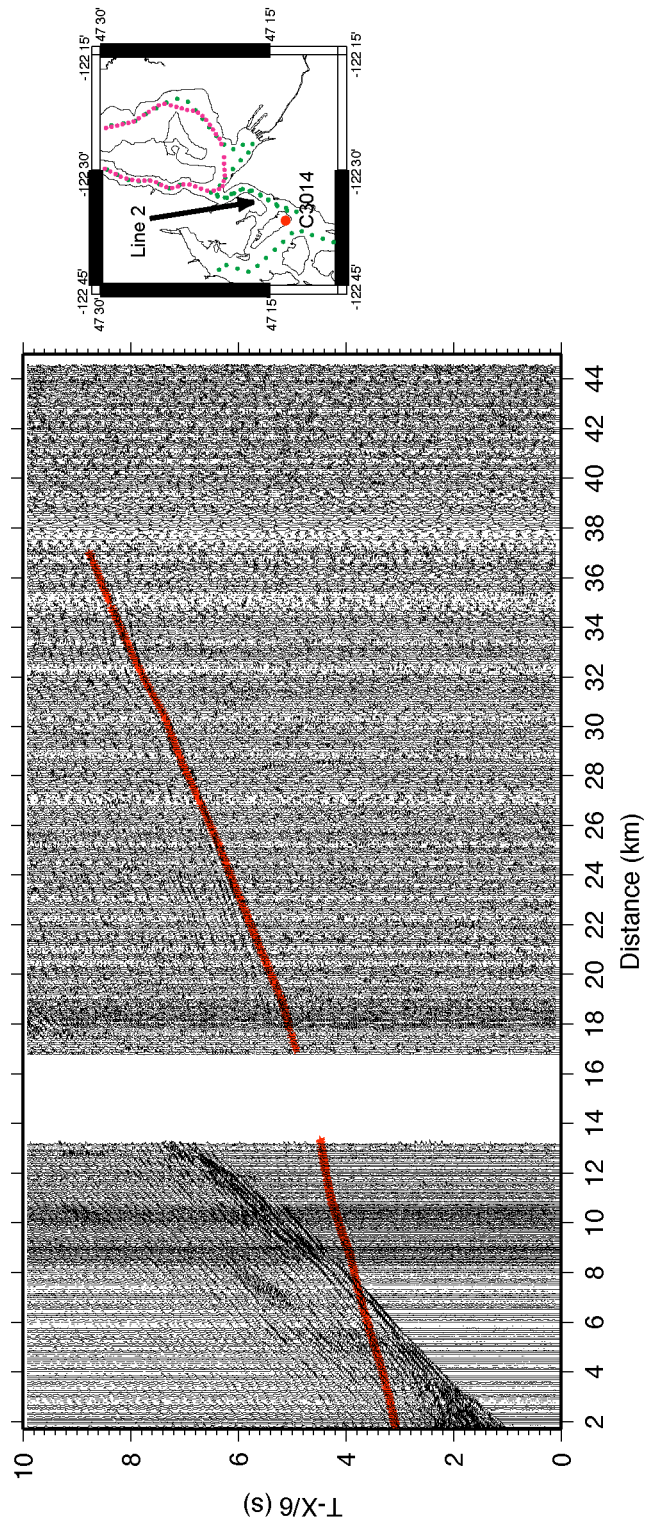


Figure 48: Shots from line 2 recorded at station C3014 with reflection travel time calculations overlain.

Station D4010 -- Shot Line 3

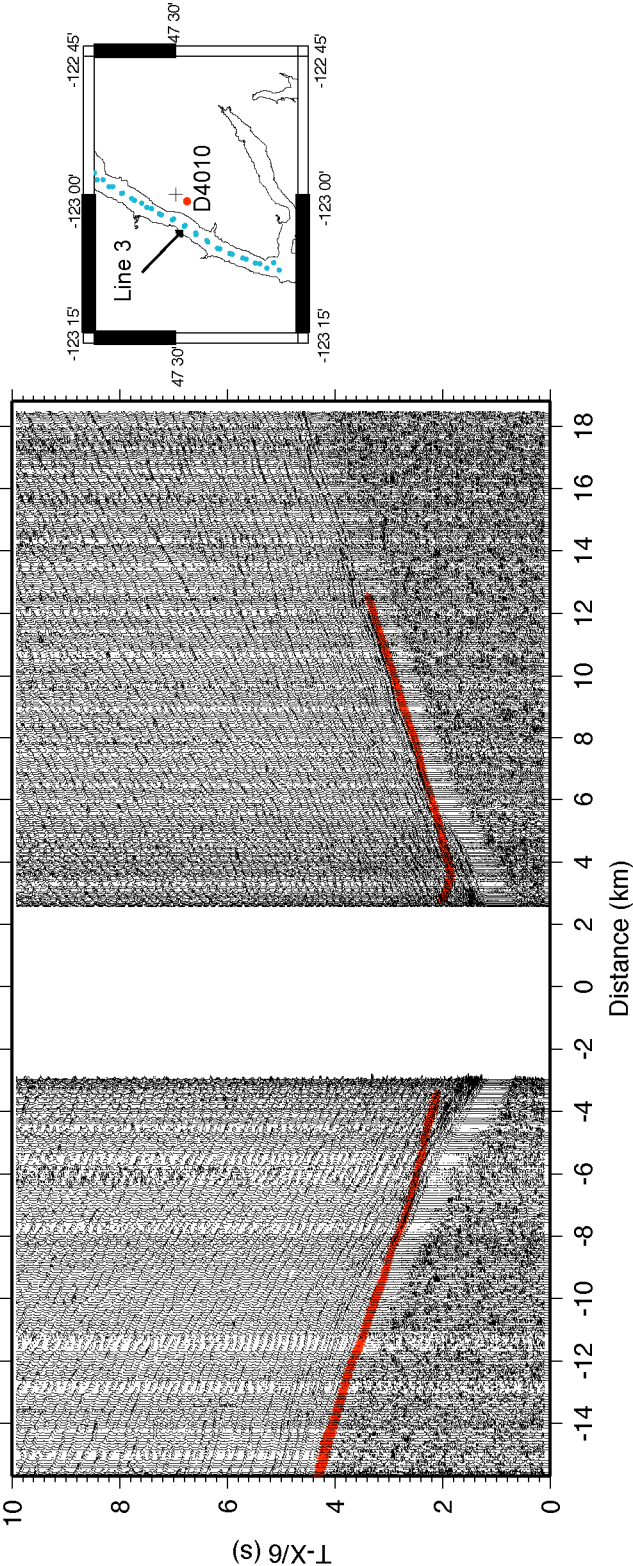


Figure 49: Shots from line 3 recorded at station D4010 with reflection travel time calculations overlain.

Station D4011 -- Shot Line 3

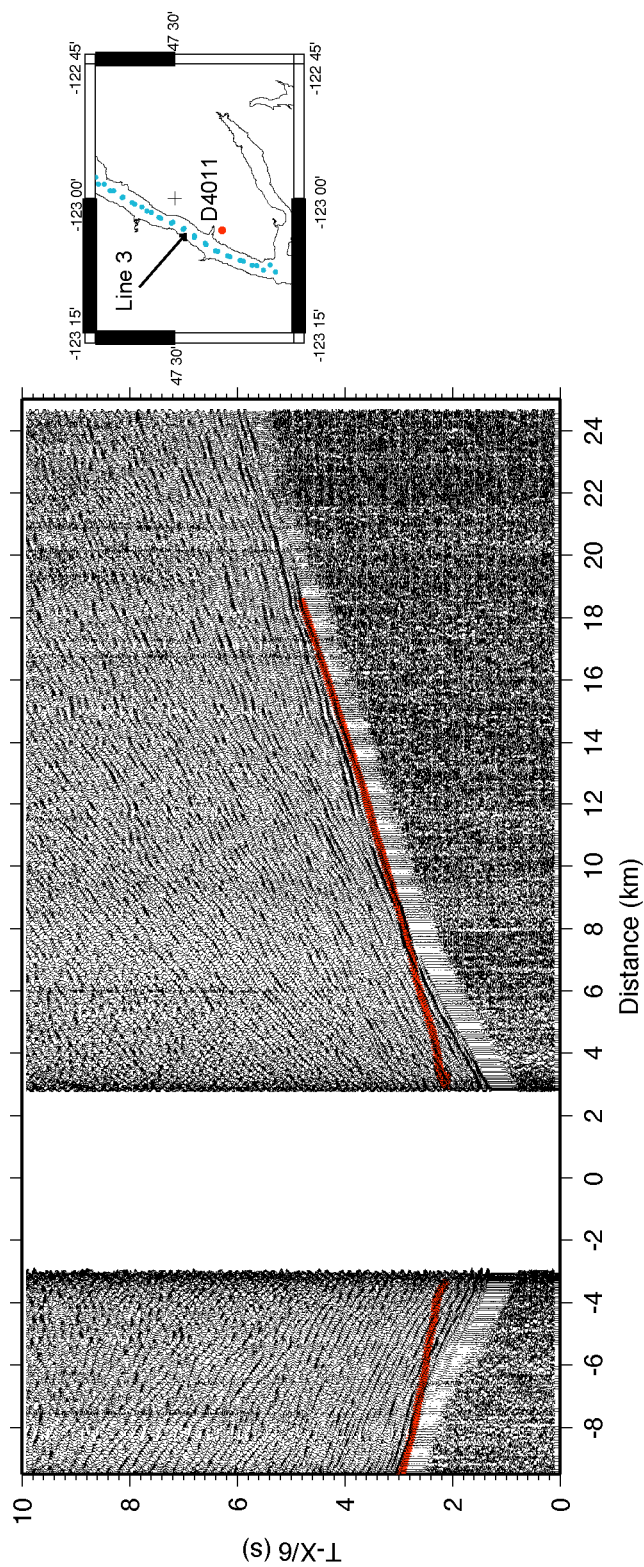


Figure 50: Shots from line 3 recorded at station D4011 with reflection travel time calculations overlain.

Station C3011 with a decon -- Shot Line 2

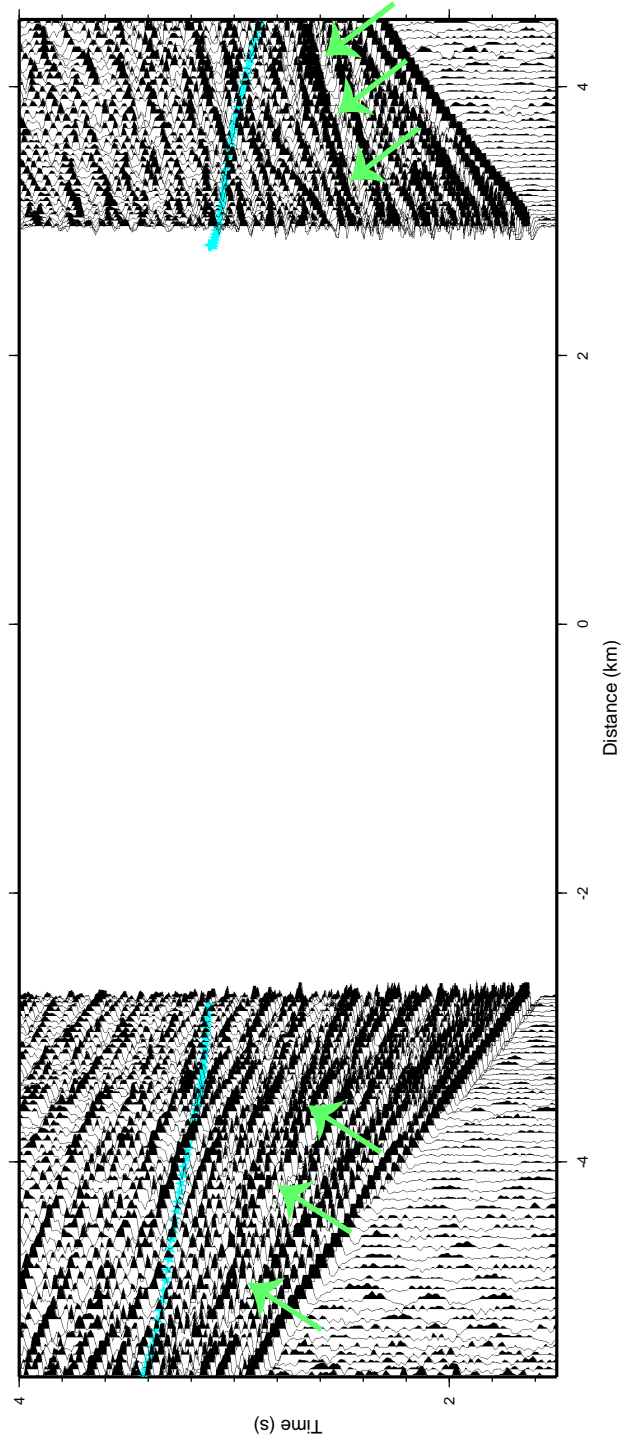


Figure 51: Station C3011 with a deconvolution applied. A prediction distance of 30 ms and an operator length of 300 ms were used in the deconvolution. The blue line represents the calculated reflection travel times. The green arrows point out the possible reflectors brought out by the deconvolution.

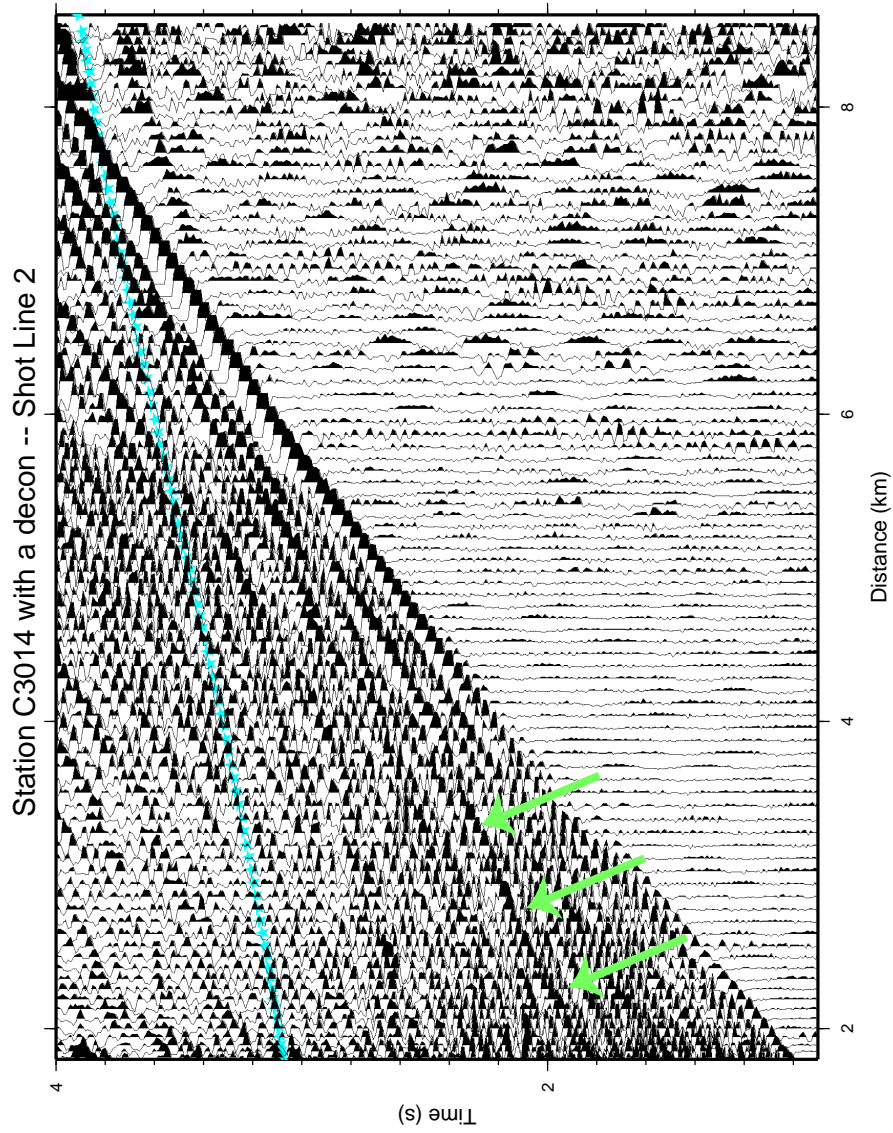


Figure 52: Station C3014 with a deconvolution applied. A prediction distance of 30 ms and an operator length of 300 ms were used in the deconvolution. The blue line represents the calculated reflection travel times. The green arrows point out a possible reflector brought out by the deconvolution.

Station D4010 with a decon -- Shot Line 3

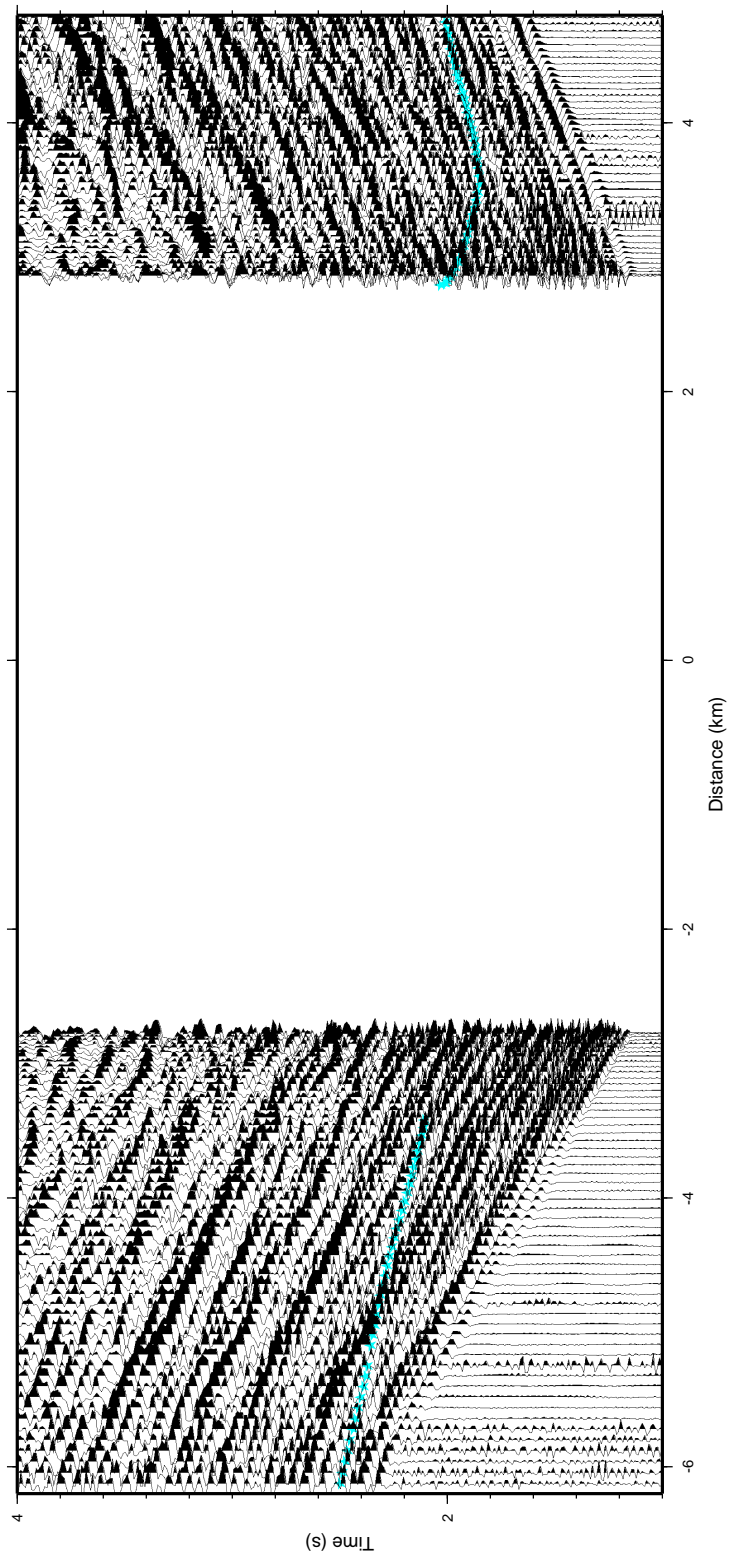


Figure 53: Station D4010 with a deconvolution applied. A prediction distance of 30 ms and an operator length of 300 ms were used in the deconvolution. The blue line represents the calculated reflection travel times. There are no reflections evident in the data even after the deconvolution has been applied

Because so few stations contained visible reflection energy from the top of the Crescent, no attempt was made to model the basin/Crescent boundary using reflection travel times. An interface inversion is in the process of being written by John Hole. This code may be the next step in determining the actual top of the Crescent Formation where the tomography reflection calculations could not.

Discussion

Until this tomographic study, the constraints on the geometry of the Tacoma Basin came only from the gravity modeling and limited single-fold seismic reflection profiling in waterways (Pratt et al., 1997; Danes et al., 1965). These studies estimated the maximum depth of the Tacoma basin to be approximately 3.5 km and suggest that the basin shallows to the north at the Seattle Uplift and to the south at the Black Uplift, where either Crescent Formation crops out or approaches the surface. Little is known of the stratigraphy of the basin sediments due to lack of well control.

The tomography results from this study have provided critical additional constraints on the geometry of the Tacoma basin. Transition of velocities from about 4.0-4.5 km/s to 5.0-6.0 km/s indicates a basin composed of 3 sub-basins trending in a northwest-southeast direction (Figure 37). Dips on the boundaries of the two southeastern sub-basins are relatively low angle at less than 10 degrees (Figures 40-44), however the sub-basin to the northwest shows larger dips around 30 degrees (Figure 41, 63 km slice). This northwest sub-basin is bounded on the northwest edge by the Hood Canal fault. A difference in velocities is evidence for the Tacoma Narrows fault that bounds the northern edge of the Tacoma basin and the southern edge of the Seattle uplift (Figure 42, e.g., slices made at 50 km and 45 km). The Tacoma Narrows fault appears to dip to the north. High velocities (6.5-7.0 km/s) that become shallow up from ~10

km beneath the southern part of the Tacoma basin show the root of the Black Hills uplift (Figures 42-43).

The new velocity model suggests that some of the assumptions that underpin the interpretation of seismic reflection data (Figure 54) in the Tacoma Basin by Pratt et al. (1997) are incorrect. These workers picked a reflector at 1 - 2 s that appears to be an unconformity on the basis of onlap relationships to be top of Crescent (Figures 55-57). By extrapolating this reflector northward it was originally tied to a well on the Seattle uplift that penetrated igneous rock at 213 m. Pratt et al. (1997), lacking any stacking velocity information from these single-channel data, assumed an RMS velocity of 3.5 km/s above this reflector and thus derived the 3.5 km estimate for the maximum depth of the Tacoma basin.

When the velocity model from the tomography is converted to rms velocity and overlain on the seismic reflection data (Figures 55-57), it is clear that the 3.5 km/s assumption significantly over estimates the true rms velocities of the sediments. The tomography shows that RMS velocities above the reflector are actually only 1.5 to 2 km/s and suggest that the depth to the reflector is only 1 to 2 km.

Depth conversion of the seismic reflection data using the velocity model derived from the tomography (Figures 58-60) calls into question whether the reflector is truly top of Crescent as the reflector crosses a region of the velocity model where velocities are only 2.5 to 3.5 km/s. As discussed earlier, previous workers in this region have used the 5.5 km/s contour as a proxy for the top of

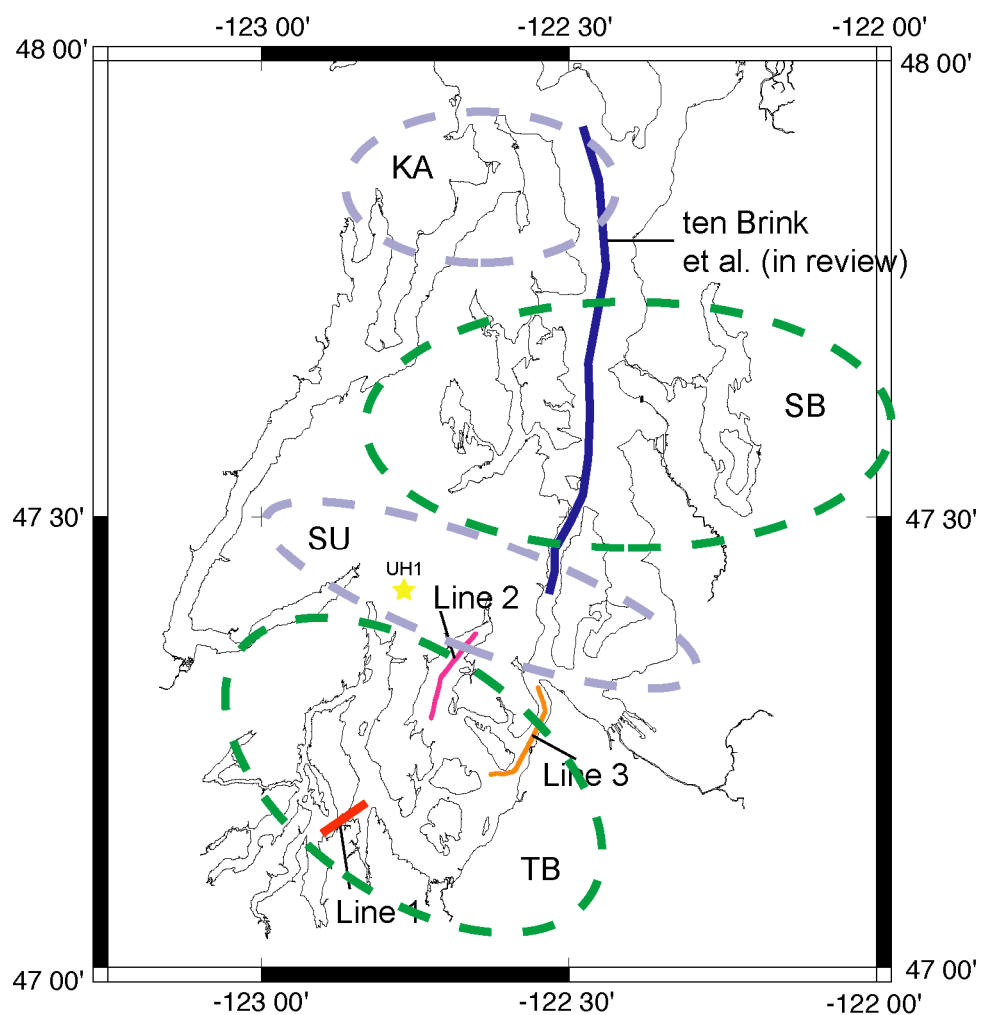


Figure 54: Map of reflection lines in the Puget Lowland with structure of interest overlain and outlined in dashed lines: TB=Tacoma Basin; SU=Seattle Uplift; SB=Seattle Basin; KA=Kingston Arch. UH=Union Oil Company Hofert no. 1 well (Pratt et al., 1997).

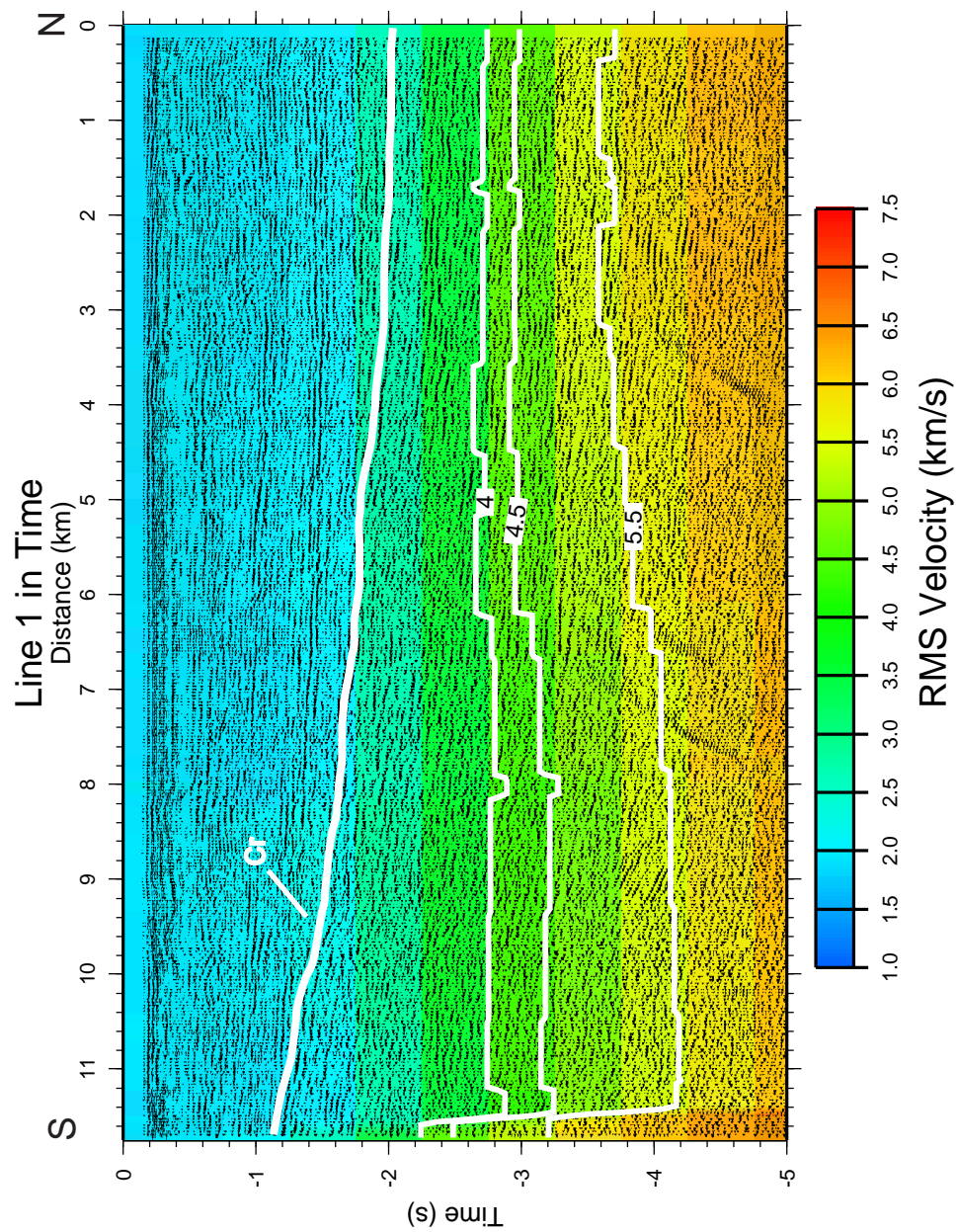


Figure 55: Reflection line 1 in time with velocities and velocity contours overlain .
Pratt's et al., 1997 interpretation labeled Cr.

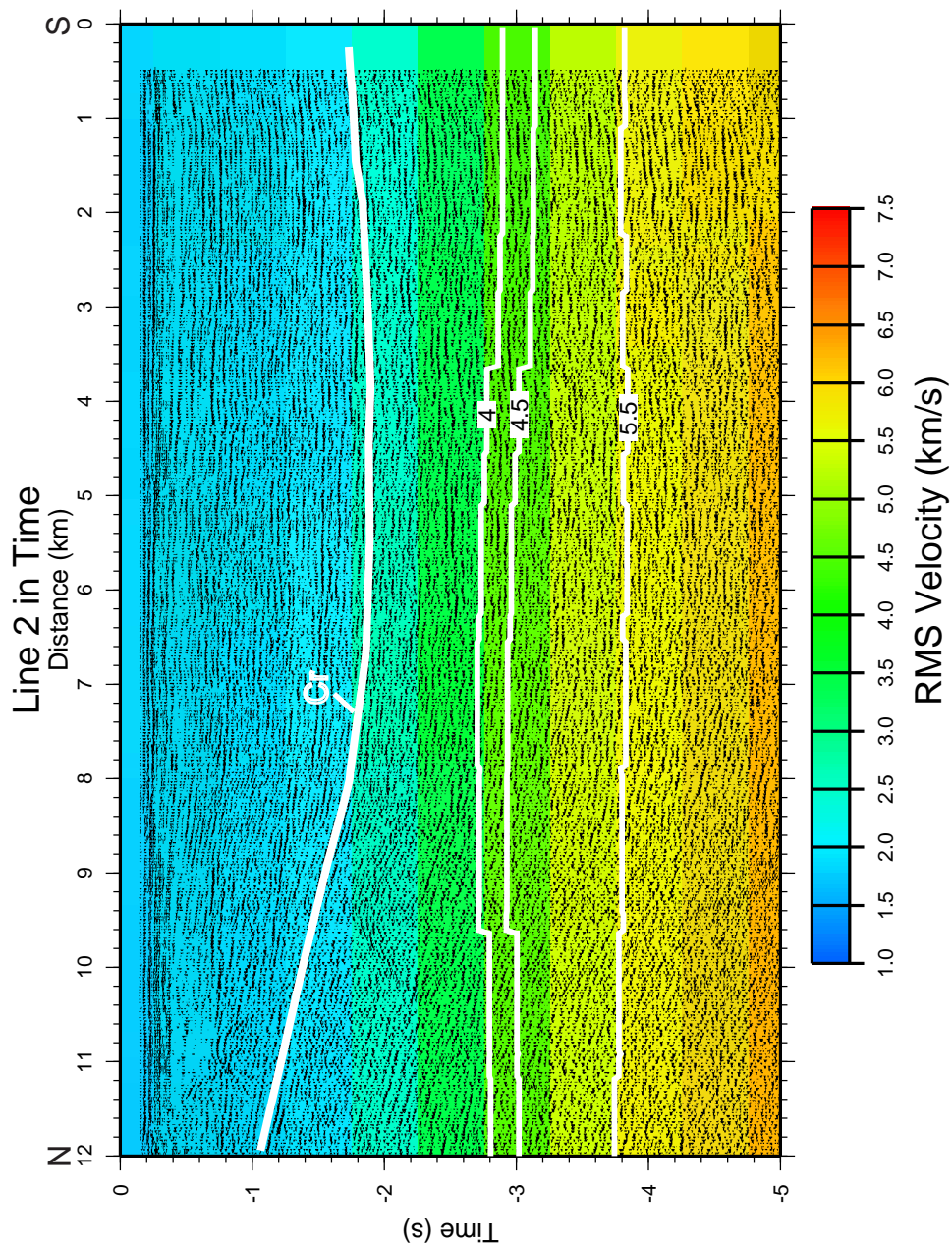


Figure 56: Line 2 reflection with rms velocities and velocity contours overlain. Pratt's et al. (1997) interpretation labeled Cr (Crescent Formation).

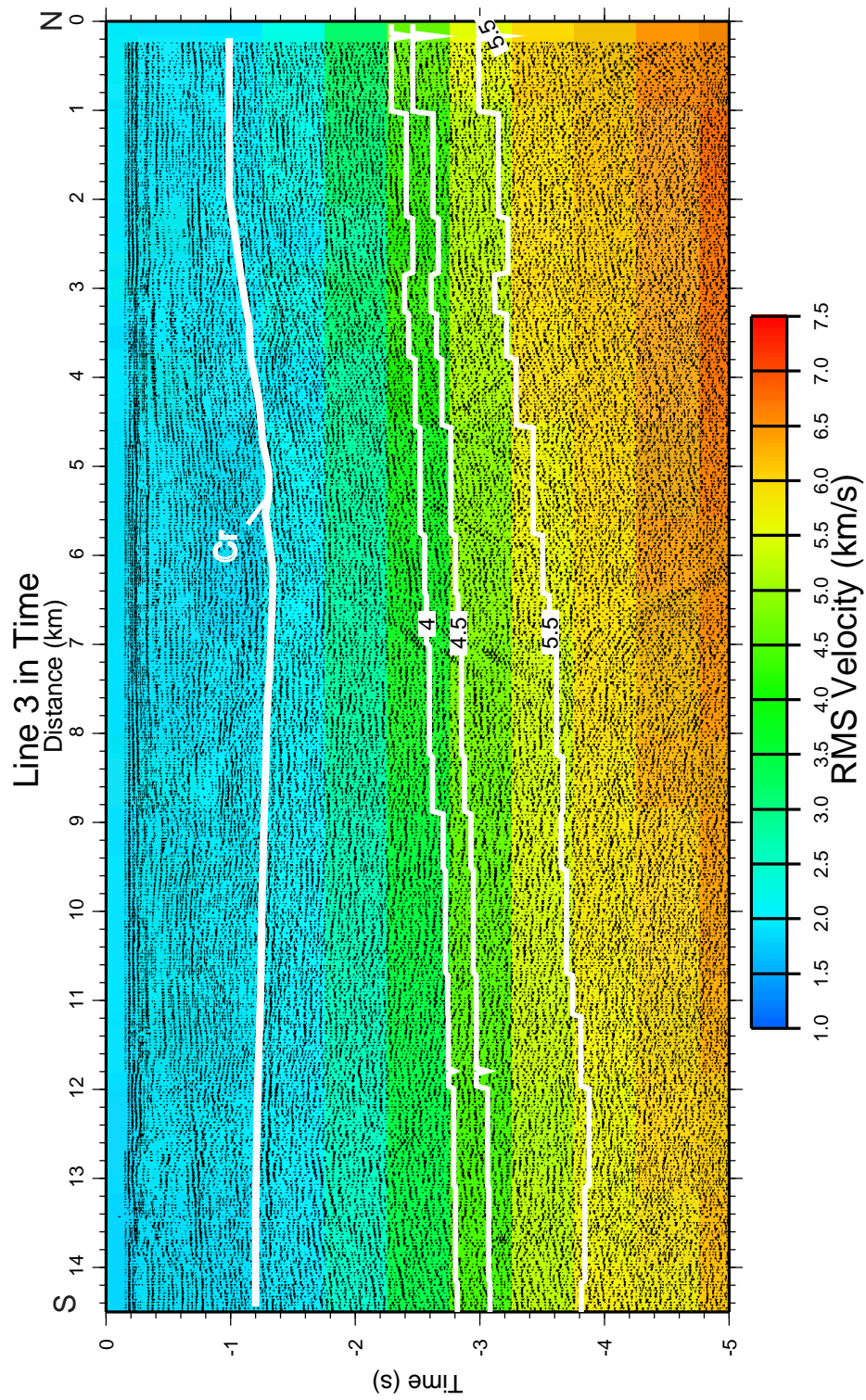


Figure 57: Line 3 reflection with rms velocities and velocity contours overlain. Pratt's et al. (1997) interpretation labeled Cr (Crescent Formation).

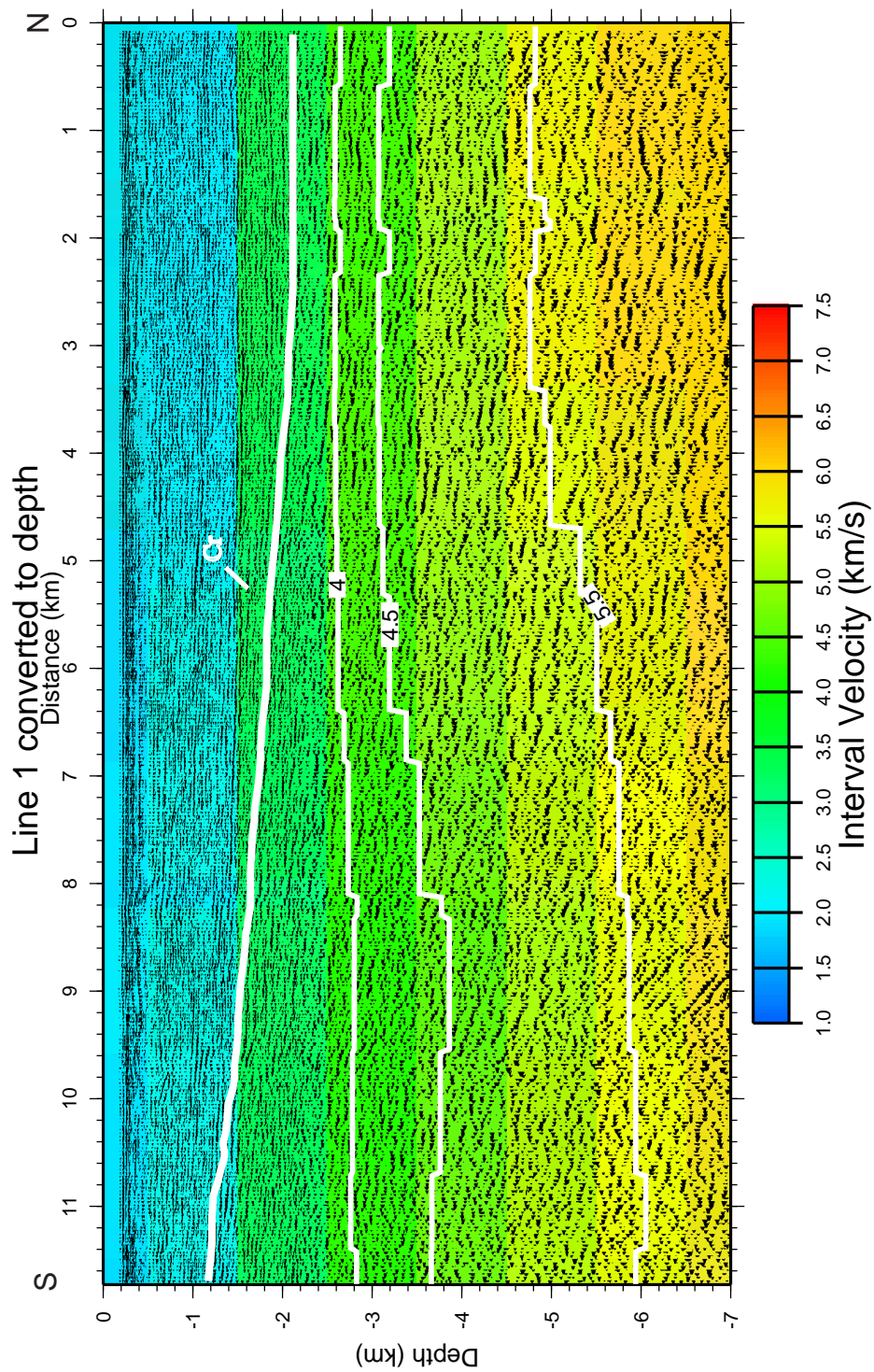


Figure 58: Reflection line 1 in depth with velocities and velocity contours overlain.
Pratt's et al., 1997 interpretation labeled Cr.

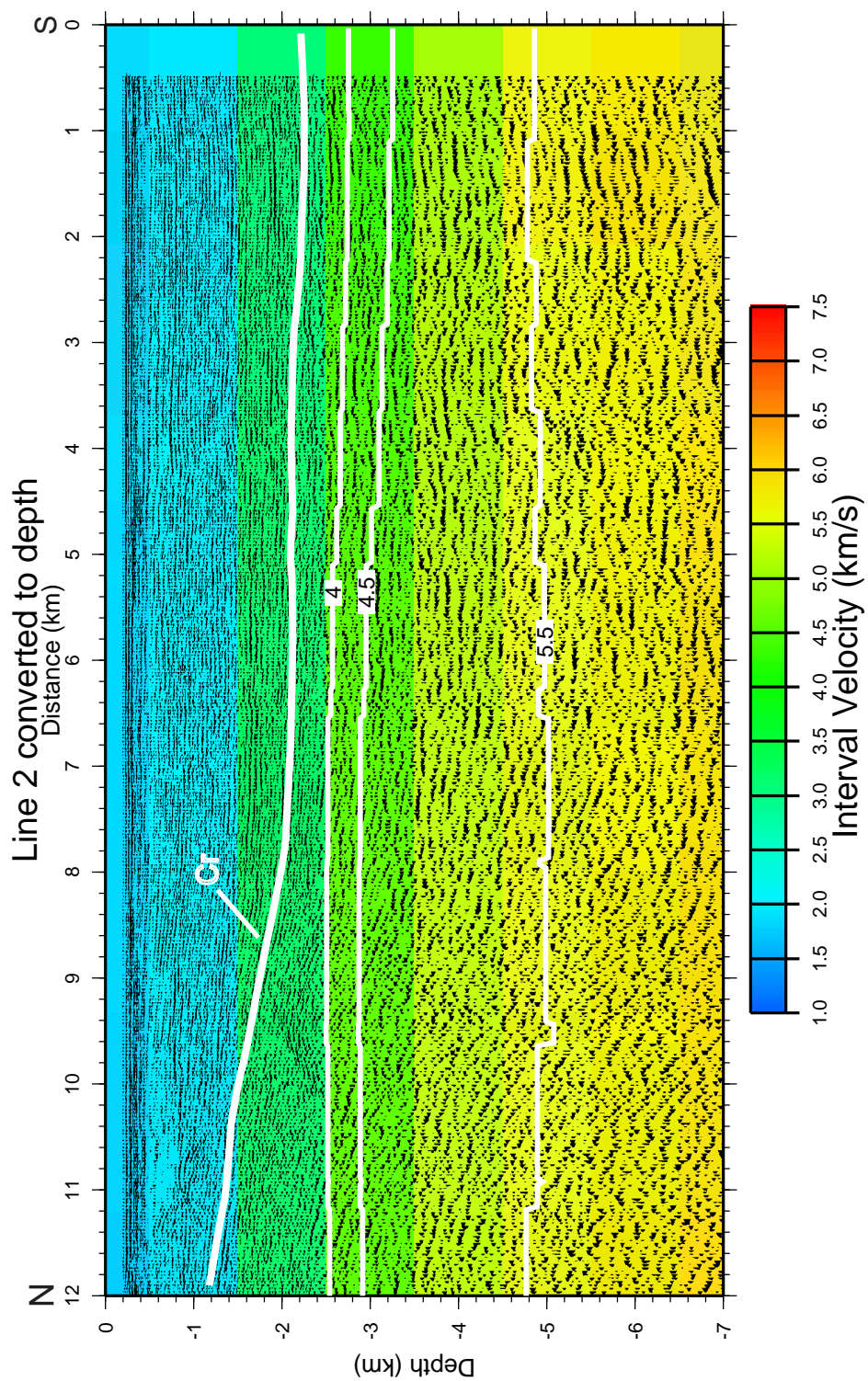


Figure 59: Line 2 reflection with rms velocities and velocity contours overlain. Pratt's et al. (1997) interpretation labeled Cr (Crescent Formation).

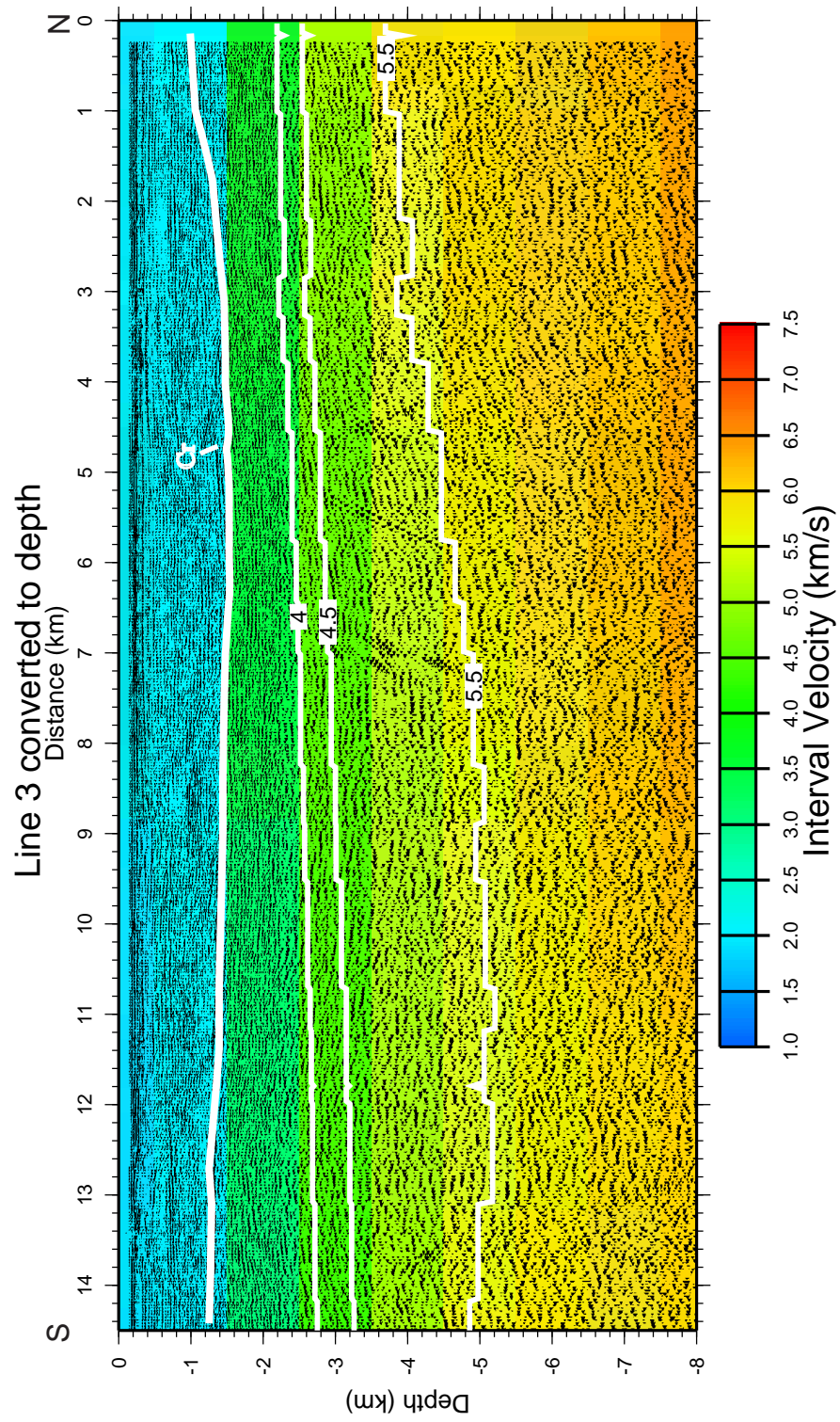


Figure 60: Line 3 reflection with rms velocities and velocity contours overlain. Pratt's et al. (1997) interpretation labeled Cr (Crescent Formation).

the Crescent Formation. When this contour is overlain on the reflection data it is evident that the reflector chosen by Pratt is 2 to 5 km shallower than the 5.5 km/s contour (Figures 58-60). Two end-member explanations for this are that either the 5.5 km/s contour is a poor choice to represent the top of the Crescent or the reflector chosen by Pratt et al. (1997) as top of Crescent represents another, younger boundary.

Just to the north in the Seattle basin, a velocity model by ten Brink et al. (in review) that is tied to reflection data and well data shows that the top of Crescent corresponds to velocities of 4.0 to 4.5 km/s at depths of 2 to 7 km. This is the most reliable tie available in the region and indicates that the 4 or 4.5 km/s contour is probably a better proxy for top Crescent.

In the Tacoma model, the observation that the velocity gradient between the 4.0 and 4.5 km/s is very strong, supports the concept of using 4 or 4.5 km/s as a proxy for top Crescent. The transition from basin sediments to high velocity Crescent rocks would be expected to be rapid (occurring over tens of meters). The close spacing of the 4 and 4.5 km/s contours suggests that it is the best candidate for that transition in the Tacoma Basin.

Although the 4 and 4.5 km/s are nearly coincident with the reflector previously picked as top Crescent in the central part of the Tacoma basin, the contours diverge from the reflector to the north and south (Figures 58-60). This suggests that this reflector may represent another, younger horizon. If we assume that Tacoma and Seattle basins have similar stratigraphy then a good

alternate interpretation of the reflector is that it represents the unconformity between the Miocene Blakely Harbor Formation and the Oligocene Blakeley Formation (Figure 4). Another possibility is that the reflector is the equivalent to the contact between the Oligocene Blakeley Formation and the Eocene Narizian Strata (Figure 4). This contact is a high-amplitude reflector in the reflection data from the Seattle basin (ten Brink et al., in review; Johnson et al., 1994) and may also correspond to this relatively high-amplitude reflection in the Pratt et al. dataset.

Structural Evolution

Both thin-skinned and thick-skinned tectonic models have been proposed for the tectonic evolution of the Puget Lowland. With all of these data and ideas at hand, an origin for the Tacoma basin as well as the Puget Lowland could be constructed. Pratt et al. (1997) have proposed a fault-bend fold style normally characteristic of sedimentary strata and defined as “thin-skinned”. Geometries in the Puget Lowland are suggestive of this style of deformation, but the thrust system hypothesized by Pratt et al. (1997) involves basement rocks at mid-crustal depths and not just shallow sediments. Low-angle faults are also the product of this Suppe (1983) model. A “thick-skinned” model for the Puget Lowland proposed by Wells and Weaver (1993) and supported by Brocher et al. (in review) propose moderately dipping faults (50-65 degrees) that extend to the base of the Crescent Formation (Figure 61) instead. In this model, deformation would root much deeper than in the Pratt et al. model.

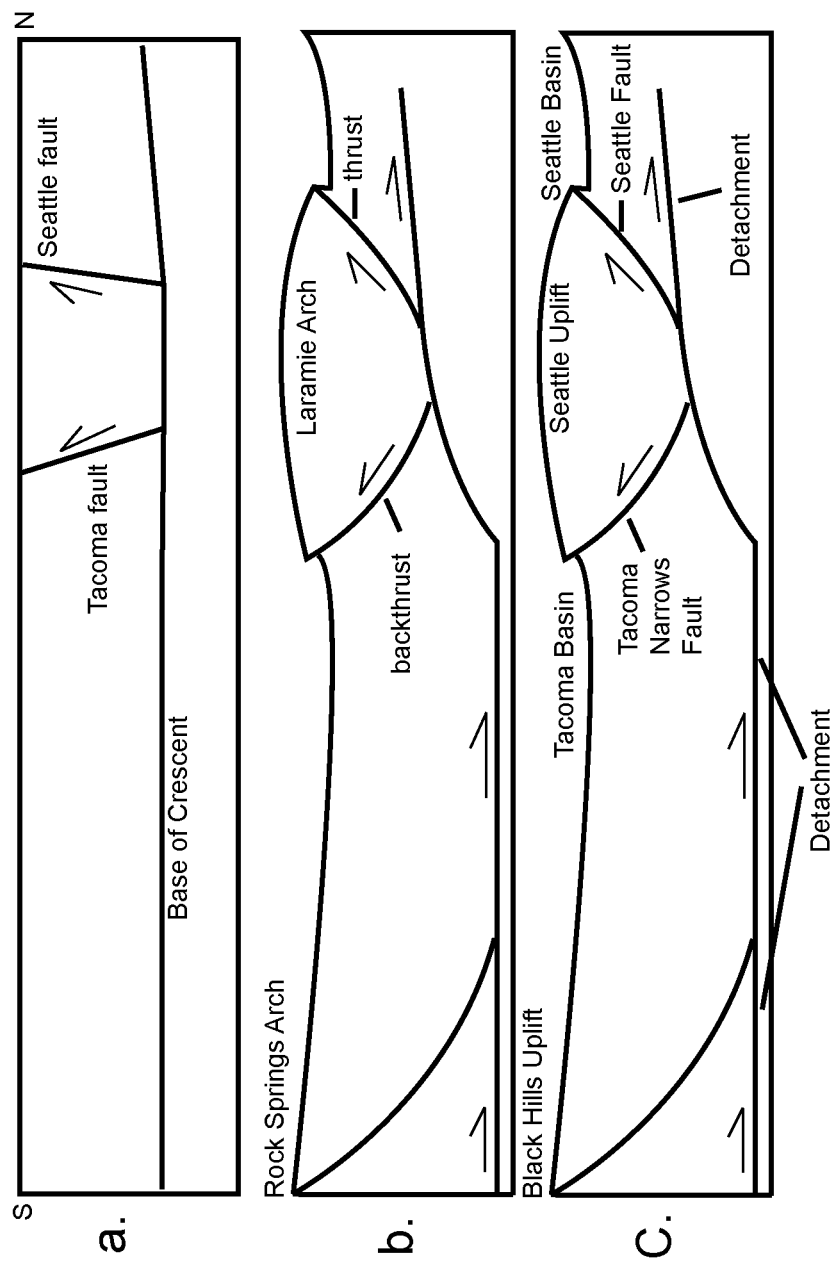


Figure 61: (a) Crustal model after Brocher et al. (in review), (b) Precambrian basement cross-section in Wyoming, after Blackstone, 1990, (c) Thrust-sheet model in the Puget Lowland with the Tacoma Narrows fault added, after Pratt et al., 1997.

An alternate model might be that proposed by Erslev (1993) for Laramide structures of the Rocky Mountains. He proposes that Laramide uplifts actually represent anastomosing arches that are bound by thrusts and back thrusts that sole into a master detachment in the middle crust (Figure 62). In this model, crustal shortening and detachment are driven by horizontal compression that parallels plate convergence.

Possible parallels between the Erslev (1993) model and the geometries of the Puget Lowland can be drawn. The Seattle fault dipping to the south may extend down to the decollement described by Pratt et al. (1997). This would be analogous to the listric master thrust fault that merges with the crustal detachment described by Erslev (1993). The north-dipping Tacoma Narrows fault would be comparable to the back-thrust off of the south-dipping Seattle fault. The result of these two mechanisms could produce the Seattle uplift. Subsequent relief produced on both sides of the Seattle uplift would lead to the formation of the Seattle basin to the north and the Tacoma basin to the south. Differential uplift produced by the master thrust fault favoring the north side would produce the deeper Seattle basin and the shallower Tacoma basin (Figure 61). The Doty fault that is located on the south side of the Black Hills uplift may be a back-thrust fault off of the main detachment in the crust. The result of this back-thrust would be the Black Hills uplift just south of the Tacoma basin. This would be analogous to the Rock Spring's Arch in Erslev's model in Figure 61b.

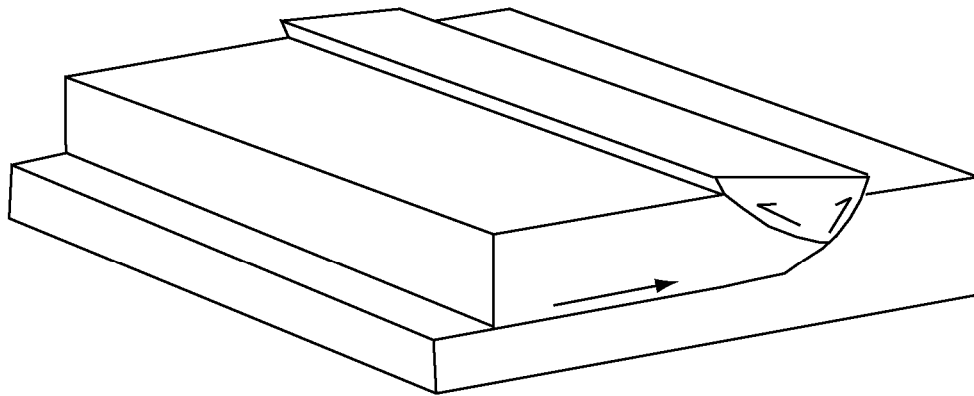


Figure 62: Schematic cartoon of the basement surface in northern Colorado Front Range showing a thrust block with both forward and back thrusting on the eastern margin.

Comparison of an actual cross-section across the Rocky Mountain foreland from Erslev (1993) with a proposed cross-section from the Puget Lowland shows the resemblance of the Laramide model to the structures in the Puget Lowland (Figure 61). The Erslev model combined with results from this study provides new insight into origin and structures surrounding the Tacoma basin.

North-south trending strike-slip faults in the Puget Sound imaged with 2D reflection seismic (Johnson et al., 1999) may also have been a driving mechanism in the creation of the two smaller subbasins of the Tacoma basin. If these faults did extend far enough to the south before the thrusting regime began, then the possibility for these as initiators of the pull-apart basins should be considered. The data does not image across the Seattle uplift so the southern extent of these strike-slip faults is unknown.

Conclusions

Depth to the Crescent Formation based on this study and previous studies appears to be between 3 km and 4.5 km. Velocities by themselves do not determine the top of the Crescent well, but when used with reflection seismic, we get a better estimate of this contact. The velocity models indicate the Tacoma basin is made up of 3 subbasins, 2 of which have less than half the areal extent of the main basin. The Tacoma basin may have formed as a combination of forearc basin development and relief from the Seattle uplift. Thrusting and backthrusting based on Laramide models could produce relief to contribute to basin development. North-south strike-slip faulting imaged north of the Seattle uplift suggests that the smaller subbasins may have formed as pull-apart basins.

With a better estimate of the geometry and velocities of the Tacoma basin in hand, ground motion experts will be able to more reliably estimate the potential for seismic hazards.

References

- Armstrong, R.L., Cenozoic igneous history of the U.S. Cordillera from latitude 42° to 49° north in *Cenozoic tectonics and regional geophysics of the western Cordillera*, 265-282, *Geol. Soc. Am.*, 1978.
- Atwater, B.F., and Hemphill-Haley, E., Recurrence intervals for great earthquakes of the past 3500 years at Northeastern Willapa Bay, Washington, *U. S. Geol. Sur. Prof. Pap. 1576*, 108 pp, 1997.
- Atwater, B.F., Implications of plate tectonics for the Cenozoic tectonic evolution of western North America, *Geol. Soc. Am. Bull.*, 81, 3513-3536, 1970.
- Babcock, R. S., Burmester, R.F., Engebretson, E.C., Warnock, A., A rifted origin for the Crescent basalts and related rocks in the northern Coast Range volcanic province, Washington and British Columbia, *J. Geophys. Res.*, 97, 6799-6821, 1992.
- Blakely, R.J., and Jachens, R.C., Volcanism, isostatic residual gravity, and regional tectonic setting of the Cascade volcanic province, *J. Geophys. Res.*, 95, 19,439-19,451, 1990.
- Boatwright, J., Seekins, L.C., Fumal, T.E., Liu, H., Mueller, C.S., Ground motion amplification in the Marina District, *Bull. Seis. Soc. Am.*, 81, 1980-1997, 1991.
- Booth, D.B., Glaciofluvial infilling and scour of the Puget Lowland, Washington, during ice-sheet glaciation, *Geology*, 22, 695-698, 1994.
- Brandon, M.T., and Calderwood A.R., High-pressure metamorphism and uplift of the Olympic subduction complex, *Geology*, 18, 1252-1255, 1990.
- Brandon, M.T., and Vance, J.A., Tectonic evolution of the Cenozoic Olympic subduction complex, Washington state, as deduced from fission track ages for detrital zircons, *Am. J. of Sci.*, 292, 565-636, 1992.
- Brocher, T.M., Parsons, T., Creager, K.C., Crosson, R.S., Symons, N.P., Spence, G., Zelt, B.C., Hammer, P.T.C., Hyndman, R.D., Trehu, A.M., Miller, K.C., ten Brink, U.S., Fisher, M.A., Pratt, T.A., Alvarez, M., Beaudoin, B., Wide-angle seismic recordings from the 1998 Seismic Hazards Investigation of Puget Sound (SHIPS), western Washington and British Columbia, *U.S. Geological Survey Open-file report*, Preliminary draft, 59 pp., 1998.

- Brocher, T.M., Parsons, T., Blakely, R.J., Christensen, N.I., Fisher, M.A., Wells, R.E., and the SHIPS working group, Upper crustal structure in Puget Lowland, Washington: results from the 1998, Seismic Hazards Investigation in Puget Sound, *J. Geophys. Res.*, in review.
- Cady, J.W., Calculation of gravity and magnetic anomalies of finite-length right polygonal prisms, *Geophysics*, *45*, 1507-1512, 1980.
- Caress, D.W., Menard, H.W., and Hey, R.N., Eocene reorganization of the Pacific-Farallon Spreading center north of the Mendocino fracture zone, *J. Geophys. Res.*, *93*, 2813-2838, 1988.
- Carver, D., Harzell, S.H., Earthquake site response in Santa Cruz, California, *Bull. Seis. Soc. Am.*, *86*, 55-65, 1996.
- Catchings, R.D., Kohler, W.M, Reflected seismic waves and their effect on strong shaking during the 1989 Loma Prieta, California, earthquake, *Bull. Seis. Soc. Am.*, *86*, 1401-1416, 1996.
- Clague, J.J., Evidence for large earthquakes at the Cascadia subduction zone, *Rev. Geophys.*, *35*, 439-460, 1997.
- Coney, P.J., Jones, D.L., Monger, J.W.H., Cordilleran suspect terranes, *Nature*, *298*, 329-333, 1980.
- Danes, Z.F., Bonno, M.M., Brau, E., Gilham, W.D., Hoffman, T.F., Johansen, D., Jones, M.H., Malfait, B., Masten, J., Teague, G.O., Geophysical investigation of the southern Puget Sound area, Washington, *J. Geoph. Res.*, *70*, 5573-5580, 1965.
- Dickinson, W.R., Sedimentary basins developed during evolution of Mesozoic-Cenozoic arc-trench system in western North America, *Can. J. Earth Sci.*, *13*, 1268-1287, 1976.
- Duncan, R.A., A captured island chain in the Coast Range of Oregon and Washington, *J. Geophys. Res.*, *87*, 827-837, 1982.
- Field, E.H., and Jacob, K.H., A comparison and test of various site response estimation techniques, including three that are not reference site dependent, *Bull. Seism. Soc. Am.*, *85*, 1127-1143, 1995.
- Field, E.H., Spectral amplification in a sediment-filled valley exhibiting clear basin-edge induced waves, *Bull. Seis. Soc. Am.*, *86*, 991-1005, 1996.

- Finn, C., Geophysical constraints on Washington convergent margin structure, *J. Geophys. Res.*, 95, 19,533-19,546, 1990.
- Fisher, M.A., Brocher, T.M., Hyndman, R.D., Trehu, A.M., Weaver, C.S., Creager, K.C., Crosson, R.S., Parsons, T., Cooper, A.K., Mosher, D., Spence, G., Zelt, B.C., Hammer, P.T., tenBrink, U.S., Pratt, T.L., Miller, K.C., Childs, J.R., Cochrane, G.C., Chopra, S., and Walia, R., Seismic survey probes urban earthquake hazards in the Pacific Northwest, *EOS Transactions AGU*, 80, no. 2, 13-17, 1999.
- Gower, H.D., Yount, J.C., and Crosson, R.S., Seismotectonic map of the Puget Sound region, Washington, *U.S. Geol. Sur. Map I-1613*, scale 1:250,000, 1985.
- Graves, R.W., Modeling three-dimensional site response effects in the Marina District basin, San Francisco, California, *Bull. Seis. Soc. Am.*, 83, 1042-1063, 1993.
- Guffanti, M., Weaver, C.S., Distribution of volcanic vents in the Cascade Range: Volcanic arc segmentation and regional tectonic considerations, *J. Geophys. Res.*, 93, 6513-6529, 1988.
- Hartzell, S., Harmsen, S., Frankel, A., Carver, D., Cranswick, E., Meremonte, M., Michael, J., First-generation site-response maps for the Los Angeles region based on earthquake ground motions, *Bull. Seis. Soc. Am.*, 88, 463-472, 1998.
- Heaton, T.H. and Kanamori, H., Seismic potential associated with subduction in the northwestern United States, *Bull. Seis. Soc. Am.*, 73, 933-942, 1984.
- Hole, J.A., Nonlinear high-resolution three-dimensional seismic travel time tomography, *J. Geophys. Res.*, 97, 6553-6562, 1992.
- Hough, S.E., Field, E.H., On the coherence of ground motion in the San Fernando Valley, *Bull. Seis. Soc. Am.*, 86, 1724-1732, 1996.
- Hyndman, R.D., and Wang, K., Tectonic constraints on the zone of major thrust earthquake failure: The Cascadia subduction zone, *J. Geophys. Res.*, 98, 2039-2060, 1993.
- Johnson, S.Y., Evidence for a margin-truncating fault (pre-late Eocene) in western Washington, *Geology*, 12, 538-541, 1984.

- Johnson, S.Y., Eocene strike-slip faulting and nonmarine basin formation in Washington, in *Biddle, K.T., and Christie-Blick, N., eds., Strike-slip deformation, basin formation, and sedimentation: Society of Economic Paleontologists and Mineralogists Special Publication 37*, p. 283-302, 1985.
- Johnson, S.Y., Potter, C.J., Armentrout, J.M., Origin and evolution of the Seattle fault and Seattle basin, Washington, *Geology*, 22, 71-74, 1994.
- Johnson, S.Y., Potter, C.J., Armentrout, J.M., Miller, J.J., Finn, C., Weaver, C.S., The southern Whidbey Island fault: An active structure in the Puget Lowland, Washington, *Geol. Soc. Am. Bull.*, 108, 334-354, 1996.
- Johnson, S.Y., Dadisman, S.v., Childs, J.R., Stanley, W.D., 1999, Active tectonics of the Seattle fault and central Puget Sound, Washington—Implications for earthquake hazards, *Geol. Soc. Am. Bull.*, 111, 1042-1053, 1999.
- Lees, J.M., and Crosson, R.S., Tomographic imaging of local earthquake delay times for three-dimensional velocity variation in western Washington, *J. Geophys. Res.*, 95, 4763-4776, 1990.
- Lermo, J., Chavez-Garcia, F.J., Site effect evaluation using spectral ratios with only one station., *Bull. Seism. Soc. Am.*, 83, 1574-1594, 1993.
- Ludwin, R.S., Weaver, C.S., Crosson, R.S., Seismicity of Washington and Oregon, *The Geology of North America*, 1, 77-98, 1991.
- Meremonte, M., Frankel, A., Cranswick, E., Carver, D., Worley, D., Urban seismology—Northridge aftershocks recorded by multi-scale arrays of portable digital seismographs, *Bull. Seis. Soc. Am.*, 86, 1350-1363, 1996.
- Miller, K.C., Keller, G.R., Gridley, J.M., Luetgert, J.H., Mooney, W.D., and Thybo, H., Crustal structure along the west flank of the Cascades, western Washington, *J. Geophys. Res.*, 102, 17,857-17,873, 1997.
- Moczo, P., Labak, P., Kristek, J., Hron, F., Amplification and differential motion due to an antiplane 2D resonance in the sediment valleys embedded in a layer over the half-space, *Bull. Seis. Soc. Am.*, 86, 1434-1446, 1996.
- Nelson, A.R., Atwater, B.F., Bobrowsky, P.T., Bradley, L., Clague, J.J., Carver, G.A., Darienzo, M.E., Grant, W.C., Krueger, H.W., Sparks, R., Stafford, T.W., Jr., and Stuiver, M., Radiocarbon evidence for extensive plate-

boundary rupture about 300 years ago at the Cascadia subduction zone, *Nature*, 378, 371-374, 1995.

Parsons, T., Trehu, A.M., Luetgert, J.H., Miller, K.C., Kilbride, F., Wells, R.E., Fisher, M.A., Flueh, E., ten Brink, U.S., Christensen, N.I., A new view into the Cascadia subduction zone and volcanic arc: implications for earthquake hazards along the Washington margin, *Geology*, 26, 199-202, 1998

Parsons, T., Wells, R.E., Fisher, M.A., Three-dimensional velocity structure of Siletzia and other accreted terranes in the Cascadia forearc of Washington, *J. Geophys. Res.*, 104, 18,015-18,039, 1999.

PASSCAL, Users Guide, A Guide to Planning Experiments Using PASSCAL Instruments: IRIS, 28 pp., 1991.

Pratt, T.L., Johnson, S.Y., Potter, C.J., Stephenson, W.J., Finn, C., Seismic reflection images beneath Puget Sound, western Washington state: The Puget Lowland thrust sheet hypothesis, *J. Geophys. Res.*, 102, 27496-27489, 1997.

Pratt, T.L., Weaver, C.S., Brocher, T.M., Parsons, T., Creager, K.C., Crosson, R.S., Symons, N.P., Spence, G., Zelt, B.C., Hyndman, R.D., Trehu, A.M., Miller, K.C., ten Brink, U.S., Fisher, M.A., Understanding the seismotectonics of the Cascadia subduction zone: overview and recent seismic work, abstract, 10 pp., 1999.

Raines, G.L., Johnson, B.R., Digital representation of the Washington state geologic map: a contribution to the Interior Columbia River Basin Ecosystem Management Project, *U.S. Geol. Surv. Open File Rep.*, 95-684, 19 p., 1996.

Rasmussen, N.H., Millard, R.C., Smith, S.W., Earthquake hazard evaluation of the Puget Sound Region, Washington State: Seattle, University of Washington, 99 pp., 1974.

Riddihough, R.P., Hyndman, R.D., Canada's active western margin—the case for subduction, *Can. J. Earth Sci.*, 16, 350-363, 1977.

Riddihough, R.P., Recent movements of the Juan de Fuca plate system, *J. Geophys. Res.*, 89, 6980-6994, 1984.

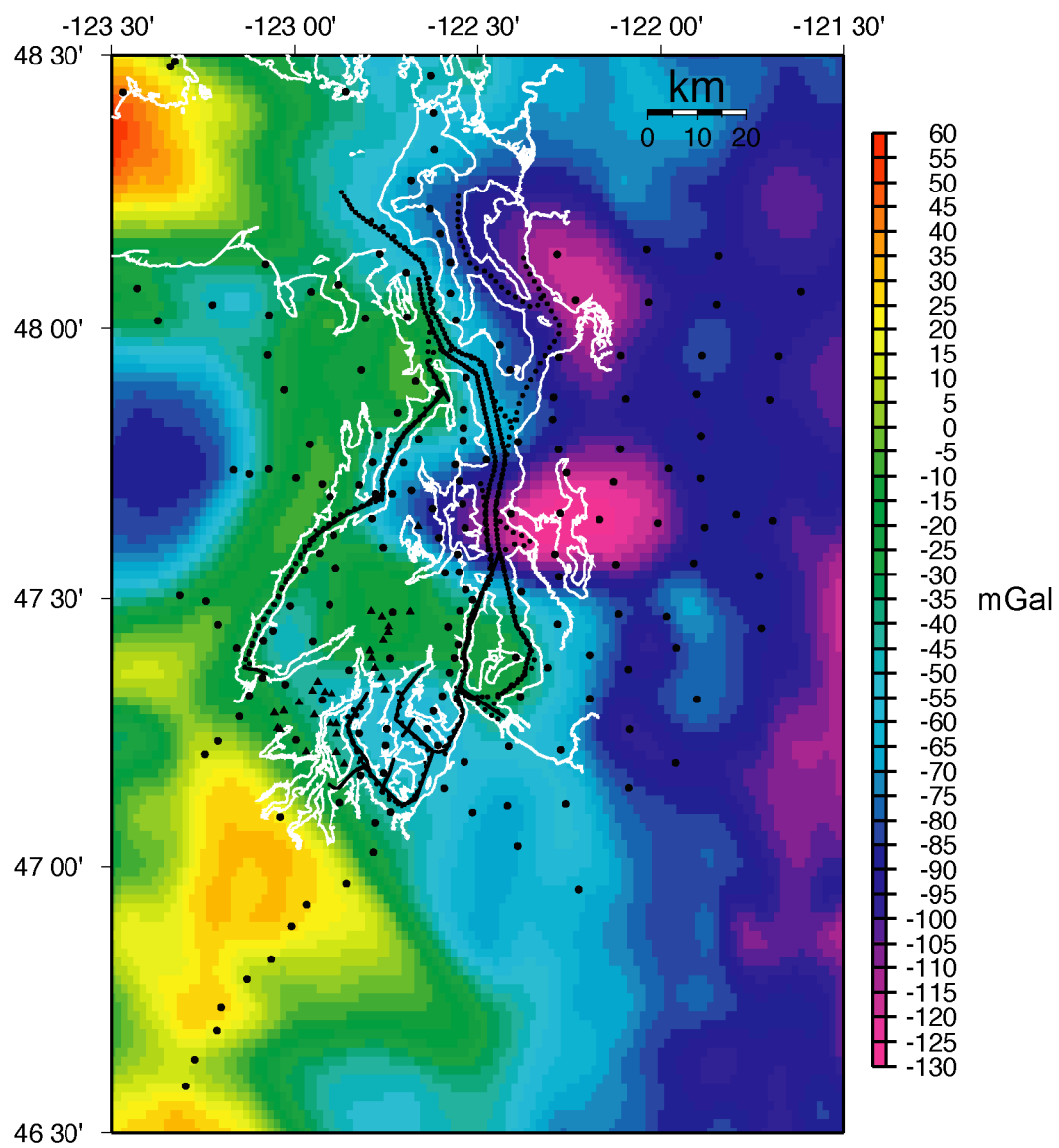
- Schultz, A.P., Crosson, R.S., Seismic velocity structure across the central Washington Cascade Range from refraction interpretation with earthquake sources, *J. Geophys. Res.*, 101, 27899-27915, 1996.
- Simpson, R.W., Cox, A., Paleomagnetic evidence for tectonic rotation of the Oregon Coast Range, *Geology*, 5, 585-589, 1977.
- Snively, P.D. Jr., Tertiary geologic framework, neotectonics, and petroleum potential of the Oregon-Washington continental margin, in Scholl, E. W., Grantz, A., and Vedder, J. G., eds., *Geology and resource potential of the continental margin of western North America and adjacent ocean basins, Beaufort Sea to Baja California: Circum-Pacific Council for Energy and Mineral Resources, Earth Science Series*, 6, p. 305-335, 1987.
- Snively, P.D. Jr., MacLeod, N.S., Yachats Basalt—An upper Eocene differentiated volcanic sequence in the Oregon Coast Range, *J. Res. U.S. Geol. Surv.*, 2, 395-403, 1974.
- Stanley, W.D., Finn, C., Plesha, J.L., Tectonics and conductivity structures in the southern Washington Cascades, *J. Geophys. Res.*, 92, 10,179-10,193, 1987.
- Stanley, W.D., Mooney, W.D., Fuis, G.S., Deep crustal structure of the Cascade Range and surrounding regions from seismic refraction and magnetotelluric data, *J. Geophys. Res.*, 95, 19,419-19,438, 1990.
- Stanley, W.D., Villasenor, A., and Benz, H., Subduction zone and crustal dynamics of western Washington: a tectonic model for earthquake hazards evaluation, *U.S. Geol. Sur. Open File Rep. 99-311*, 64 pages, 64 illustrations, 1999.
- Steidl, J.H., Tumarkin, A.G., Archuleta, R.J., What is a reference site?, *Bull. Seis. Soc. Am.*, 86, 1733-1748, 1996.
- Suppe, J., Geometry and kinematics of fault-bend folding, *Am. J. Sci.* 283, 684-721, 1983.
- Symons, N.P., Crosson, R.S., Seismic velocity structure of the Puget Sound region from 3-D non-linear tomography, *Geophys. Res. Lett.*, 24, 2593-2596, 1997.
- Taber, J.J., Lewis, B.T.R., Crustal structure of the Washington continental margin from refraction data, *Bull. Seis. Soc. Am.*, 76, 1011-1024, 1986.

- Taber, J.J., Smith, S.W., Seismicity and focal mechanisms associated with the subduction of the Juan de Fuca plate beneath the Olympic Peninsula, Washington, *Bull. Seis. Soc. Am.*, 75, 237-249, 1985.
- Tabor, R.W., Cady, W.M., Geologic map of the Olympic Peninsula, Washington, *U.S. Geol. Surv. Misc. Invest. Ser. Map*, I-994, 1978.
- Tabor, R.W., Frizzell, V.A. Jr., Vance, J.A., Naeser, C.W., Ages and stratigraphy of lower and middle Tertiary sedimentary and volcanic rocks of the central Cascades, Washington: Application to the tectonic history of the Straight Creek Fault, *Geol. Soc. Am. Bull.*, 95, 26-44, 1984.
- Tabor, R.W., Late Mesozoic and possible early Tertiary accretion in western Washington state: The Helena-Haystack melange and the Darrington-Devils Mountain fault zone, *Geol. Soc. Am. Bull.*, 106, 217-232.
- Talwani, M., Worzel, J.L., Landisman, M., Rapid gravity computations for two-dimensional bodies with applications to the Mendocino Submarine Fracture Zone, *J. Geophys. Res.*, 64, 49-59, 1958.
- ten Brink, U.S., Molzer, P.C., Fisher, M.A., Brocher, T.M., Parsons, T., Crosson, R.S., Creager, K.C., Structure and evolution of the Seattle Fault and Basin, Washington, *Geology*, 18 pp., in review.
- Thorson, R.M., Earthquake recurrence and glacial loading in western Washington, *GSA Bull.*, 108, 1182-1191, 1996.
- Trehu, A., Asudeh, I., Brocher, T.M., Leutgert, J.H., Mooney, W.D., Nabelek, J.L., Nakamura, Y., Crustal architecture of the Cascadia forearc, *Science*, 266, 237-243, 1994.
- Van de Vrugt, H., Day, S., Magistrale, H., Wedberg, J., Inversion of local earthquake data for site response in San Diego, California, *Bull. Seis. Soc. Am.*, 86, 1447-1458, 1996.
- Vidale, J., finite-difference calculation of travel times, *Bull. Seis. Soc. Am.*, 78, 2062-2076, 1988.
- Wald, D.J., Graves, R.W., The seismic response of the Los Angeles basin, California, *Bull. Seis. Soc. Am.*, 88, 337-356, 1988.
- Weaver, C.S., Baker, G.E., Geometry of the Juan de Fuca plate beneath Washington and northern Oregon from seismicity, *Bull. Seis. Soc. Am.*, 78, 264-275, 1988.

- Weaver, C.S., Smith, S.W., Regional tectonic and earthquake hazard implications of a crustal fault zone in southwestern Washington, *J. Geophys. Res.*, 88, 10371-10383, 1983.
- Wells, R.E., Engebretson, D.C., Snively, R.D. Jr., Coe, R.S., Cenozoic plate motions and the volcano-tectonic evolution of western Oregon and Washington, *Tectonics*, 3, 275-294, 1984.
- Wells, R.E., Heller, P.L., The relative contribution of accretion, shear, and extension to Cenozoic tectonic rotation in the Pacific Northwest, *Geol. Soc. Am. Bull.*, 100, 325-338, 1988.
- Wells, R.E., Paleomagnetic rotations and the Cenozoic tectonics of the Cascade arc, Washington, Oregon, and California, *J. Geophys. Res.*, 95, 19,409-19,417, 1990.
- Wennerberg, L., Borchardt, R.D., Mueller, C., Dietel, C., Sembera, E., Westerlund, R., Aftershock observations suggestive of large linear site amplification at the Cedar Hill nursery accelerograph station, Tarzana, California (abstract), *Seis. Res. Lett.*, 65, A56, 1994.
- Zelt, C.A., Lateral velocity resolution from three-dimensional seismic refraction data, *Geophys. J. Int.*, 135, 1101-1112, 1998.
- Zhang, B., Papageorgiou, A.S., Simulation of the response of the Marina District Basin, San Francisco, California, to the 1989 Loma Prieta earthquake, *Bull. Seis. Soc. Am.*, 86, 1382-1400, 1996.

Appendix -- Gravity

Bouguer gravity map in the Puget Lowland. Stations (circles) and shot lines 2, 3, and 9 are shown on the map. Reflection lines are also shown. Twenty-seven new gravity measurements taken in September 1999 are shown as triangles. Units are in milligals. The bouguer values were obtained using a gravity reducing script at UTEP. These 27 values were incorporated into existing gravity data in the region and were gridded and contoured together.



Curriculum Vitae

Brett Joseph Hielt was born in West Allis, Wisconsin, on October 9th, 1973. The son of Derrell and Patricia Hielt, he graduated from Andress High School in El Paso, TX, in June of 1992. He attended Texas Tech University for 4 _ years and West Texas A&M University for a semester. After graduating from Texas Tech University in May 1997 with a Bachelor of Science in Geophysics, he was accepted and enrolled at the University of Texas at El Paso and began the Master of Science program in Geophysics. After teaching earth science labs for a year, he was granted a research assistantship to analyze data from the SHIPS 1998 experiment. In the spring of 1999, he worked as an intern for Anadarko Petroleum and began full-time employment with Anadarko in June 2000.

This thesis was typed by Brett Hielt.